AIRCRAFT TAXI LOADS IN UNPAVED SURFACES

Lucía González Fernández

Department of Bioengineering and Aerospace Engineering
Universidad Carlos III de Madrid

Bachelor Thesis supervisor: Héctor Climent Máñez

EPS Leganés June 2016

Á miña nai

Acknowledgements

I would like to thank Héctor Climent for the opportunity he gave me to work at Airbus Structural Dynamics and Aeroelasticity Department for three rewarding and challenging months. It has totally been an astonishing career kick-starter since I tackled a real engineering problem for the very first time ever. I specially appreciate your dedication and motivation shown during the Aeroelasticity course I took last semester. That definitely piqued my interest of the field.

Likewise, I praise Guillermo Pastor mentoring. He has been working hard during these three months to deliver a global perspective of the problem so that it is perfectly understandable. Not only that, he helped me use Airbus software resources and was always willing to offer his help with whatever issue it might rise. The quality the final results present is also credited to him. Long story short, thank you for your patience.

Special thanks to the Department staff who made me feel like one of them since day one. Particularly, I would like to express my gratitude to Silvia Parra who helped me dealing with any issue related to the landing gear model, and Sebastián Claverías for his continuous encouragement and support on any arising software doubt.

My old and new friends are also part of this. If it weren't for you, your constant and unceasing support and good times, this wouldn't have been as exciting as it is. Many thanks to those fantastic people I have met during these hectic four years. Keep on rocking as you do.

Last but not least, I would deeply like to thank my mother for her constant support and endurance. You have taught me to face whatever situation it may rise with strength and bravery. I am getting stronger with each passing day because you showed me how to. Thanks for being there when I tumble down. *Por último, pero non por elo menos importante, gustaríame agradecer á miña nai o seu constante apoio e aguante. Ensinásteme a enfrontar calquer situación con forza e valentía. Cada día, son máis forte porque ti demostrásteme como. Grazas por estar ao meu lado cando me estou a derrubar.*

Abstract

Taxi is the intermediate phase found prior to takeoff or after landing. The aircraft normal modes are excited given a determined runway roughness profile. As a matter of fact, the coupling between the aircraft modes and the runway roughness profile contributes to the amplification of the aircraft response and the appearance of dynamic loads. The latter is intensified when taxiing on unpaved surfaces.

Characteristic aircraft elements and magnitudes sized during taxi include the wing down bending moment and the loads acting on the landing gear, paying particular attention to the loads exerted on the nose landing gear.

The experimental aircraft response is attempted to be reproduced by performing numerical simulations. So far, numerical taxi loads were computed by following the requirements established in Airworthiness Regulations specific to taxi:

- Constant taxi speed
- Symmetric cases
- Constant external loads

Far from that, the experimental response gathered through a selection of taxi cases found at different Airbus taxi campaigns is reproduced in this Bachelor Thesis by introducing a series of modifications which represent what is indeed occurring during tests:

- Variable taxi speed
- Asymmetric cases
- Variable external loads

The effect the braking coefficients have on the taxi problem, along with the nose landing gear load relief phenomenon encountered in poor cohesive surfaces is also analysed.

Contents

List of Figures

List of Tables

Chapter 1

Introduction to the taxi loads problem

1.1 Introduction

Taxi is described as the entire phase of ground movement prior to final takeoff and following landing [1]. The action of braking and turning may be found during taxi operation, however, these activities are classified as separate operations. Taxiing is comprehended as a straight line motion on ground [2].

The taxi phase would not be considered a relevant issue if the runway were perfectly smooth. Far from that, non-ideal runways present a determined roughness profile. This implies that a variation in height is assumed along the runway longitudinal axis [2].

In this dissertation thesis, the focus is set on the analysis of the A400M taxi operations in unpaved runways. It is noticeable that taxi in unpaved surfaces is appreciated as a more critical problem when compared to taxi in paved surfaces. The reason behind this is due to the fact of the runway profile. In general terms, unpaved surfaces present a more exacerbated roughness profile than paved runways. Thus, an amplified dynamic response is obtained by means of exciting the aircraft normal modes and the appearance of dynamic loads.

The taxi problem has been tackled and documented since mid fifties. Companies such as Lockheed began to analyse said issue in the sixties [3]. The US Air Force utilised a general use software named TAXI to compute the aircraft dynamic response to bomb damage repair. In addition, the computation of civil aircraft dynamic response when taxiing over a determined runway roughness profile was also performed using TAXI software [4]. Aircraft specimens such as Boeing 707-320C, 727-200, 747, McDonnell Douglas DC-8-63, DC-9-40 and DC-10-10 were subjected to analysis [3].

The AGARD conference which took place in Brussels from the 4th to the 9th of April 1982 can be highlighted as a referent and guidance on the computation of taxi loads. This conference was aimed to spread guidelines on Aircraft Dynamic Response to Damaged and Repaired Runways [5].

As a consequence, CASA has developed similar software tools to tackle this problem [6]. Said software uses the aircraft normal modes obtained with commercial programs such as MSC.NASTRAN, along with the nonlinear equations that model the landing gear and its components, the linear equations which represent the aircraft itself and the runway roughness profile to simulate the taxi operation.

The taxi model is validated once a good match is obtained between the experimental data gathered at the taxi tests and the results attained through the numerical simulation. As a consequence, a set of guidelines and conclusion are drawn based on the results achieved. For instance, boundaries can be established in relation to the maximum roughness profile a given aircraft is able to operate.

As a matter of fact, the taxi loads model validation constitutes an intermediate step to reach the final aircraft certification. The initial activities which are encompassed in the process to achieve said goal are related to aircraft design. In this introductory phase, loads loops are performed: a theoretical aircraft model and ensuing loads are computed, checkstress analyses are executed to ensure that limit loads remain within established limits and regulations are fulfilled. If any of those conditions fail, the model is required to be updated. Several iterations may be needed until all requirements are met. Once the aircraft design phase is considered to be finished, the model validation stage subsequently proceeds. Within this step, taxi tests can be found as a means of validating the taxi model. This step leads to the concluding stage which deals with certification. Certification loads loops are performed using an already validated model. The aircraft is certified whenever all duly requirements and regulations are satisfied. The whole process is iterative and staggered.

Through this Final Thesis, the focus is set on the comparison between the experimental response recorded during the taxi campaigns aimed for unpaved surfaces and the results yielded after performing a numerical simulation. First, taxi trial campaigns in unpaved runways are described, where the specimens subjected to analysis are the A400M MSN2 and MSN6. Consecutively, once the relevant data required by the simulation is gathered, a numerical analysis is performed. The comparison between the taxi test data and the numerical analysis is carried out at final stages.

This dissertation is divided into six Chapters. A brief overview of the tasks and aspects tackled through each Chapter is presented below:

- **Chapter 1:** The taxi loads problem is described and put into context. For that, relevant taxi accidents are highlighted and the applicable taxi airworthiness regulations are introduced. Taxi operation main characteristics, together with the relevance the problem has on dynamic loads analyses is included. It also contains the description of taxi loads trials. Specifically, previous taxi campaigns carried out by Airbus are described in detail. Lastly, the focus is set on the fundamental concepts which come in handy to analyse taxi operations in unpaved surfaces.

- **Chapter 2:** The aircraft subjected to analysis throughout this dissertation is described along with the aircraft structural model and landing gear model. The taxi test campaigns the Thesis is focus on are described. The set of instrumentation used to record the aircraft response during taxi operation is listed. The tools required for test data postprocessing are illustrated.

- **Chapter 3:** The dynamic taxi loads model is described along with the taxi loads numerical simulation process followed to compute numerical responses.

- **Chapter 4:** The numerical response gathered after performing numerical simulations is compared with the experimental response retrieved during taxi operation throughout different campaigns, for a selected number of taxi cases. The process of numerical to experimental response matching is described, including the set of parameters which are tuned to enhance matching and to improve the quality of the numerical results obtained.

- **Chapter 5:** The fundamental points which improve the numerical results quality are further described in detail. The effect the braking coefficients have on the taxi loads problem is presented.

- **Chapter 6:** Conclusions are drawn along with recommended activities to pursue at a future time regarding the study of taxi loads and the underlying numerical simulation.

Supplementary material containing EASA CS/AMC 25.491 regulatory framework can be found in Appendix C. Furthermore, the project time planning and estimated costs are enclosed in Appendix D.

1.1.1 Relevance of the taxi loads problem

During taxi operations, the aircraft normal modes are excited as a consequence of rolling on a surface of significant roughness profile [2]. The coupling between the aircraft modes and roughness profile at a given speed contributes to the amplification of the aircraft response and the appearance of dynamic loads.

Dynamic loads during taxi operation in unpaved surfaces can be the sizing cases for some landing gear components and particular aircraft structural elements. Specifically, the loads acting on the landing gear itself, the vertical force acting on the forward fuselage and the wing down bending moment constitute the relevant magnitudes providing an insight on taxi operations.

Taxi loads are used in design and checkstress analyses of the structure to certify the aircraft, to determine inspection intervals once fatigue analyses are performed, to define maintenance operations or to estimate the number of allowable runs to perform in a specific unpaved surface given a set of conditions and configurations.

The complexity of the problem arises when dealing with the landing gear nonlinear nature. On the one hand, the aircraft structure is considered to be linear, whereas the landing gear nonlinear. Said nonlinear nature is related to the kinematic and elastic properties the components of the landing gear present.

The landing gear requirements go from absorbing energy on landing or ensuring manoeuvrability on ground to having the capability of being retracted and stowed in flight [7]. These are met by introducing a complex system of shock absorbers and wheel and tyre assemblies.

The problem is solved by coupling the nonlinear equations which model the landing gear, with the linear ones that represent the aircraft structure.

The linear equation which models the aircraft structure is expressed in modal coordinates [3]. It looks as follows:

$$[GM]\ddot{x} + [GS]x = [\emptyset]^T F_0 + [\emptyset]^T F_{t/a} \tag{1.1}$$

The preceding equation takes into consideration the aircraft flexibility. x is the modal generalised coordinate, $[GM]$ is the generalised mass matrix, $[GS]$ is the generalised stiffness matrix, $[\emptyset]$ is the modal matrix, F_0 represents the external forces (gravity effects, aerodynamic

and propulsive forces and brakes, to name a few) and $F_{t/a}$ gathers all the forces that the landing gear exerts on the aircraft.

The nonlinear equation [8] which models the landing gear can be found within the following lines. The pertaining landing gear kinematic and elastic properties are also included in the derivation [3].

$$[TM]\ddot{q} = [\bar{V}_r]F_r + [\bar{V}_a]F_a + F_{a/t} + [\bar{F}_c] \tag{1.2}$$

q denotes the landing gear geometric coordinates. $[TM]$ is the generalised mass matrix where the masses are represented as lumped masses which include the corresponding inertia properties as well, $[V_r]$ defines the geometric transformation matrix of the tyre forces, $[F_r]$ depicts the tyre forces, $[V_a]$ represents the geometric transformation matrix of the shock absorber forces and $[F_a]$ the shock absorber forces themselves, $[F_c]$ denotes the nonlinear terms in q and $[F_{a/t}]$ expresses the interaction forces between the landing gear and aircraft structure.

The solution to the system of equations is obtained by integrating on several iterations in the time domain [3]. The forces acting on the aircraft structure to landing gear attachment, pintle points, result.

The combination of the preceding equations and the solution obtained constitute an intermediate step in the numerical simulation process required to determine the overall aircraft response.

Said process is started by computing the aircraft eigenvalues and eigenvectors. To do that, the linear and flexible aircraft model is used along with the nonlinear and rigid landing gear model. Subsequently, a static balance is performed, where the forces and moments applied at the aircraft centre of gravity and 1G (static) loads at the pintle points and wheel axles are retrieved. The next step involves the computation in the time domain of the solution to the two previous equations. The forces exerted on the interface between the landing gear movable and non-movable parts are gathered. The following step is linked to the translation of the previous forces to the pintle points (landing gear to fuselage attachments). Afterwards, the aircraft transient response expressed in modal coordinates is computed in the frequency domain. Such response is finally referred to the several aircraft stations defined after performing a transformation.

For further details concerning the numerical simulation process, please refer to Chapter 3.

The taxi model is required to be validated. In order to do so, the results gathered in the simulation are compared with the data obtained in taxi test trials. The procedure is summarised in the chart below.

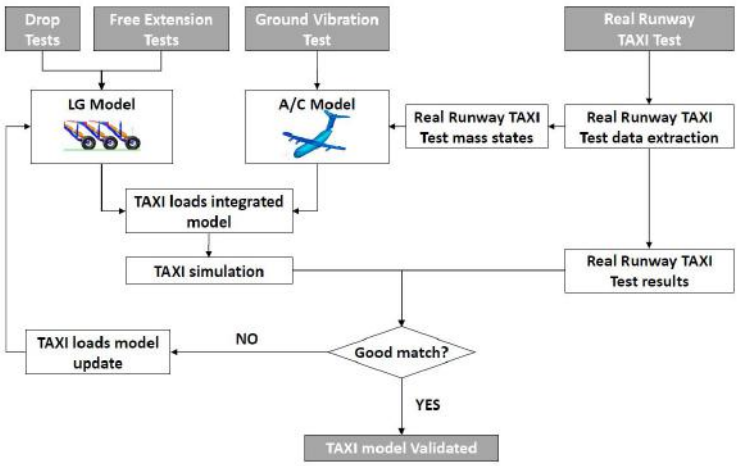

Figure 1.1 Model validation for taxi loads analyses

Following the procedure depicted in the figure above, once a valid and representative landing gear model is coupled with an aircraft model [9], and the pertinent taxi data retrieved from the tests is included in the simulation, the aircraft response is obtained after completing the simulation process described in preceding paragraphs. Such response is compared to the actual one achieved during the taxi trials to finally validate the taxi model.

Note that the comparison between the experimental data acquired at the taxi campaigns with the response computed through the numerical simulation constitutes the main core of the present Final Thesis. It should be highlighted that the leading objective behind the procedure illustrated above is to reach aircraft certification. As a matter of fact, one of the activities out of a wide range which are needed to be accomplished to certify a given aircraft is the taxi model validation.

Among all activities required for this purpose, this dissertation is focused on the acquisition of good matches (numerical simulation results similar to experimental data) to validate the taxi model for specific unpaved runways using an already certified aircraft.

1.1.2 History of taxi loads trials [3]

A400M is the new state-of-the-art military aircraft engineered by Airbus Defence and Space. Taxi test trials have been conducted in order to analyse the performance of said aircraft in different types of surfaces. Particularly, since it is expected to operate in a wide range of runway profiles, Airbus is primarily concerned about how the aircraft behaves when operating in unpaved surfaces.

CN-235 or C-295 are two aircraft models which participated in distinct taxi test campaigns launched by Airbus. Specifically, this section is devoted to the description of the tests which the C-295 took part in.

Figure 1.2 CN-235 landing on unpaved runway

Taxi trials have been conducted from March to April 2000. The aircraft subjected to analysis was C-295 Prototype 1. These trials can be split into two different scenarios: taxiing over standard obstacles and taxiing on unpaved runways.

The first mass configuration tested was 19300kg, distributed into operating empty weight plus crew, full fuel and 3000kg of payload. Two centre of gravity positions were analysed: forward and rearward. The second mass configuration was 16300kg, including operating empty weight plus crew and full fuel, with forward centre of gravity arrangement.

Multiple runs have been made at a given set of aerodynamic and propulsive settings along with a variation of the position of the centre of gravity and brake application. Velocity sweeps starting in 20 knots up to 100 knots have been performed.

The first stage of the trials was conducted in Manises paved runway, Valencia. Standard obstacles such as rectangular steps or single and double repair-plates were installed in the middle of said runway to analyse the effect of taxi loads on tyres and overall aircraft attitude,

as well as to study the aircraft response when facing single or multiple impacts. In order to evaluate the aircraft's output after taxiing over an obstacle which is representative to those found in real unpaved surfaces, a standard 1-cosine bump was used.

The second phase of this campaign took place in Agoncillo airfield (La Rioja). C-295 Prototype 1 was tested on an actual unpaved runway. The runway roughness profile indicated that the track was considered to be severe if compared to other runways PSD[1].

Figure 1.3 C-295 operating in unpaved runway, Spain

A comprehensive set of instrumentation was installed to record the aircraft response to the excitation. Accelerometers were located at the nose and rear fuselage, wing tips, horizontal tail plane tips. In addition to the previous components, both engines, the pair of ailerons and flaps, rudder and elevator were also instrumented.

The equipment used in the landing gear served to obtain data about the forces acting on the wheel axles, as well as to retrieve information about the forces, accelerations and deflections on the shock absorbers or oil and gas pressure. Since it was thought that the response would be symmetric, the left part of the main landing gear was solely instrumented.

134 different runs were performed at different taxi speeds, centre of gravity, aerodynamic, propulsive and brakes settings. The structural sizing cases of the C-295 were obtained after

[1] **PSD** Power Spectral Density:
It is defined as the Fourier Transform of the autocorrelation function. The autocorrelation is the cross-correlation of a signal with itself. It is the similarity between observations as a function of the time lag between them. It is a mathematical tool for finding repeating patterns, such as the presence of a periodic signal obscured by noise, or identifying the missing fundamental frequency in a signal implied by its harmonic frequencies [10].

The Fourier Transform of the autocorrelation function $R_{yy}(\tau)$ is given by the following mathematical expression:

$$S_{yy}(\omega) = \int_{-\infty}^{\infty} R_{yy}(\tau) e^{-i\omega\tau} d\tau \tag{1.3}$$

Practical applications of PSD approach are found in continuous turbulence analyses.

performing a thorough analysis of the results. The nose landing gear was identified as a key component when dealing with taxi in unpaved runways. Maximum values of vertical forces, oil damper pressure, damper force and shock absorber deflection were encountered when taxiing at medium-high speeds over the 1-cosine bump.

Furthermore, within the main landing gear, it was found that critical values have been reached in vertical forces, oil damper pressures and damper forces. Maximum values of said magnitudes correspond to the single rectangular step and the 1-cosine bump runs at medium to high speeds. However, shock absorber deflection critical values have been found at distinct centre of gravity configurations. It was determined that the single and double repair-plates provoked limit values of said magnitude when taxiing at low to medium speeds.

On the other hand, maximum acceleration values were discovered at forward centre of gravity position and no braking/reverse thrust settings. Critical positive wing tip and HTP tip accelerations were encountered after taxiing over the double repair-plate at high speeds. Oppositely, maximum negative wing tip and HTP tip accelerations were obtained in the single rectangular step at medium speeds. Besides, maximum engine accelerations were reached in the 1-cosine bump and double repair-plate at medium to high speeds respectively. It should be denoted that critical fuselage acceleration values were detected in the single rectangular step at high speeds.

Figure 1.4 C-295 operating in unpaved runway, Jordan

Sensitivity analyses were performed at subsequent stages. It was concluded that the aircraft weight would indirectly determine the severity of the loads acting on the landing gear and the aircraft itself. Moreover, it was demonstrated that the use of reverse thrust did not relieve the loads exerted on the nose landing gear, as it was previously thought.

Two lessons learned for future taxi trials included the recommendation to fully instrument the main landing gear in order to capture any asymmetry during the tests, and the second established that it was necessary to measure not only the roughness profile where the nose landing gear passes but the runway profile where the main landing gear goes by as well.

1.1.3 Accidents

Several accidents in civil aviation have been registered during taxi. Although neither did they occur on unpaved runways nor military aircraft were involved, they highlight the aforementioned importance of presenting a landing gear mechanism with an appropriate shock absorber and optimum tyre inflation pressure.

The oldest incident worth mentioning took place in 1963. A Douglas DC-7B landed at Nashville Metropolitan Airport in rainy conditions, the pilot applied asymmetric reverse thrust, erroneously, which caused the nose landing gear to collapse.

Regarding the application of reverse thrust, a Learjet 60 overran Columbia Metropolitan Airport runway during takeoff as the pilot unsuccessfully commanded a rejected takeoff after V1, when sparks appeared on the landing gear [11]. One of the issues which provoked the accident was due to the poor maintenance of tyres, being the right outboard tyre underinflated. In addition to this, it was discovered years before that the reverse thrust system caused a disruption in the wheel well area, inducing an uncommanded forward thrust [11]. This problem was still not resolved at the time the accident took effect.

Another noteworthy incident occurred in 2008, when a DeHavilland Canada DHC-8-301 landed at Barranquilla-Ernesto Cortissoz Airport uneventfully followed by the vibration of the right hand main landing gear and subsequent collapse of the latter [12]. The reason behind this accident was due to the fracture of the right hand main landing gear shock absorber mechanical stop ring, making the landing gear incapable of absorbing landing loads, as the system became a rigid piece.

On the other hand, Fokker 100 models (regional twinjet aircraft manufactured from 1988 to 1996 in the Netherlands) require a special mention since many incidents have been recorded during taxi encompassing this aircraft.

In Amsterdam 1987, a Fokker 100 prototype right main landing gear collapsed after a high speed (300 km/h) touchdown took place. The torque-links were sequentially lengthened in all legs to fix this issue. Furthermore, it was registered in Nigeria in 2005 that the right hand

main landing gear broke during taxi after a normal touchdown and landing. Moreover, the left hand main landing gear failed during taxi four years after in Iran when another Fokker 100 successfully landed.

Figure 1.5 Fokker 100 accident in Amsterdam Schiphol Airport, 1987

Special attention must be paid to an accident occurred in 1989. A flight from Amsterdam to Geneva landed smoothly at Geneva-Cointrin Airport, followed by sudden strong vibrations, leading to the fracture of the left main landing gear leg. Consequently, the left wing impacted ground [13].

The investigators on duty concluded that the accident sources were twofold: the damping coming from the dynamic system constituted by the main landing gear and its interface was insufficient, and the random occurrence of factors which caused a resonant vibration in the left main landing gear [13].

It was determined that a number of similar incidents and antecedents took place before this accident happened [13]:

In an established report from January 1988 reviewing the landing gear certification process, Fokker reported numerous cases of vibrations in the main landing gear, starting in January 1987.

In April 1987, strong vibrations were reported in relation to a landing executed with flaps 42º and without the usage of lift dumpers. Said vibrations were perceived at 90 to 110 knots. The analysis of the landing gear revealed that the axle of the right landing gear part was deformed.

Figure 1.6 Fokker 100 landing gear

In June 1987, after performing a dynamic test on shimmy on the main landing gear, it was found that the axle of the right hand main landing gear was broken, inducing wear in wheels and tyres.

In July 1987, when conducting the required flight tests needed for a certification campaign, it was discovered that after a high speed landing at 160 knots, the right main landing gear leg was broken. The damper was loose and the inferior part laid separated from the system. It was determined that the vibrations encountered were due to the poor stroke course that the damper followed, as well as for an insufficient torsion stiffness, as a result of deficient separation of the natural frequencies of the different vibration modes.

After these events occurred, a strengthening and lengthening of the main landing gear axle compass was decided to be included in the fleet.

In March 1989, a number of constraints were incorporated three days after the major accident happened, in order to avoid the appearance of strong vibrations on the main landing gear. These can be found in the following lines:

- Landings are prohibited to be executed with flaps 25º or less, except for emergencies.
- It is not allowed to land without armed lift dumpers.
- It is not allowed to land using the automatic braking system.
- If the brakes have to be used above 100 knots, they have to be firmly applied.
- Limitations on the allowable tailwind:
  - 5 knots if the aircraft mass is equal or higher than 35000kg.
  - 10 knots if the aircraft mass is lower than 35000kg.

The appearance of vibrations were detected many times subsequently, but there was not damage found. The aforementioned constraints were not applicable to aircraft featuring shimmy dampers on the compass axle. This was certified by the Dutch Civil Aviation Department on BLA 90-022, June 1990. Further measures comprised the installation of a non-return valve in the braking system, and a firmer spring in the brake pedals.

Right after those considerations were taken into action, a new incident arouse in Montpellier during a training flight. When landing was executed, after three laps performed using just a single engine, the right hand main landing gear began to vibrate, thus, provoking the support to burst and the leg to be separated from the rest of the aircraft. The plane's mass, flap configuration and tailwind conditions were within the established limits. However, the landing was considered to be hard (1.5g).

Finally, it was concluded that the fact of strengthening the parts concerned in the accidents could be insufficient, if the damping of the dynamic system dropped below a critical threshold [13]. Thus, the changes introduced after the accident in July 1987, including the guiding compass, did not constitute a remedy to the phenomenon that led to the rupture.

Figure 1.7 Fokker 100 accident, March 1989

On the other hand, there were also incidents where the Fokker 100 had also issues related to fatigue. A flight landing at Dallas-Fort Worth International Airport in 2001 had its right main landing gear detached from the airplane structure. A fatigue crack was found in the subsequent inspection.

To conclude, the incident occurred to an A340-211 in Brussels due to fatigue cracks is summarised briefly. The aircraft presented the right hand main landing gear disconnected from the fuselage after heavy vibrations took place when taxiing. It was discovered that a fatigue crack was developed in a high stress concentrated area induced by ground manoeuvres [14].

1.2 Airworthiness regulations on taxi

Although the A400M is classified as a military aircraft, it follows both civil and military certification specifications. In this section, the set of regulations which are applicable in taxi are presented.

In order to comply with civil regulations, CRI are established as a contract signed by Airbus and OCCAR, in which some relevant sections of the overall regulations ratified by EASA are agreed to be satisfied.

Specifically in taxi, CRI C-11 (Loading Conditions for Multi-Leg Landing Gear) is the applicable one, which comprises SC C-11 and IM C-11.

SC C-11 refers to EASA CS 25.491 Taxi, Takeoff and Landing Roll section, among others. On the other hand, IM C-11 is related to AMC 25.491 Taxi, Takeoff and Landing Roll part, to name a few. More specifically, paragraph 4e should be highlighted.

CS 25.491 is found in CS-25 Book 1 [15]. Particularly, CS 25.491 provides a set of design standards and methods to demonstrate compliance with the regulations on taxi, takeoff and landing roll for large civil transport aircraft weighing more than 12500lb. CS-25 Book 2 [15] contains AMC 25.491. Note that AMC describe acceptable methods to determine compliance with regulations. These act as guidelines, they are advisable to be followed but they do not constitute unique or mandatory approaches to show compliance.

AMC 25.491 is composed of seven sections: Purpose, Related CS Paragraphs, Background, Runway Profile Condition, Discrete Load Condition, Combined Load Condition and Tyre Conditions.

AMC 25.491 is linked to CS 25.491, among others. The importance of the runway roughness profile on dynamic loads is presented briefly as well as the chronological development of several methods to encompass dynamic loads in aircraft design.

The approach of introducing a 1-cosine bump to excite certain aircraft modes is highlighted along with the usage of PSD method. Furthermore, the runway profile of San Francisco Runway 28R, before it was repaired, is a referent in the computation and analysis of dynamic loads in taxi, takeoff and landing roll. Said runway was acknowledged to provoke high loads on airplanes based on its particularly uneven profile. Many complaints from pilots had been filled until repair works took place. Note that San Francisco 28R is a paved runway.

Paragraphs 4, 5 and 6 present detailed information on how to perform and what to include in dynamic loads analyses. Airframe flexibility and landing gear characteristics along with the appropriate tyre properties are required. The cases to analyse are symmetric. Steady aerodynamics is taken into consideration. Test trials should be run at maximum takeoff weight or maximum landing weight along with a variation of fuel, payload and centre of gravity settings.

To perform taxi loads tests in the A400M taxi campaign, AMC 25.491 paragraph 4e is taken into consideration. It reports that a set of bi-directional constant speed runs are needed to be made from 20 knots to the maximum ground speed expected in normal operation (VR in takeoff or 1.25·VL2 in landing) along with the according aerodynamic and propulsive settings. Constant speed runs demonstrate to evaluate dynamic loads peaks at a certain speed and runway roughness point. For sake of completeness, a set of runs is performed at different constant velocities to guarantee that every bump the runway presents is swept at every possible combination of speeds. In this way, the most critical bump found in a certain runway is caught.

Indeed, it is remarkable to point out that taxi runs are not performed at constant velocity in their totality. When it comes to analysing the taxi operation after landing, braking action may usually be found, the aircraft is decelerating.

Furthermore, it is also stated in AMC 25.491 paragraph 4e that the braking coefficient should be around 0.3. It should be noted that the value prescribed by the regulations is considered to be conservative. The runway hardness or soil compactness are two concepts that go hand-in-hand with the value the braking coefficient could reach. The aircraft gross weight also limits the magnitude of this parameter. On the other hand, it should be highlighted that distinct braking coefficients are normally found in each main landing gear leg during experimental tests.

Note that there are many other valid activities to show compliance different from the ones previously exposed. These just act as recommendations and guidelines that are advised to be followed.

Paragraph 5 introduces further approaches to evaluate the aircraft response to dynamic loads, by performing tests on a smooth runway with a 1-cosine bump of variable dimensions.

Further information about EASA CS 25.491 and AMC 25.491 can be found in Appendix C.

In the same fashion, the military specifications are established in MCRI. These are agreed to be satisfied in a contract signed by Airbus and OCCAR. Particularly, MCRI C-20: *Taxi, takeoff and landing roll design loads on unpaved runways* is the applicable set of regulations regarding taxi. It specifies all the criteria which have to be met, similarly to what 25.491 does in civil legislation. MCRI C-20 defines more severe roughness profiles for unpaved runways, if compared with the civil regulation, to comply with the requirements.

Airfield	Reference Weights		Runway reference	To cover
Type I	**TOW**	CSA certified Logistic High Weight MTOW.	**San Francisco 28R**	Paved civil Airfield.
	LW	CSA certified MLW @ 10 ft/s vertical speed at touchdown.		
Type II	**TOW**	CSA certified Logistic MTOW.	DEF-STAN 00-970 Leaflet 305/2 **Class A**	Hard Airfield and soft well maintained Airfield.
	LW	CSA certified MLW @ 10 ft/s vertical speed at touchdown.		
Type III	**TOW**	80% of the CSA certified 2.5g Tactical Low Level MTOW.	DEF-STAN 00-970 Leaflet 305/2 **Class B**	Semi-prepared unpaved surfaces.
	LW	CSA certified MLW @ 12 ft/s vertical speed at touchdown.		

Figure 1.8 Extract from MCRI C-20

The legislation states that the aircraft has to ensure an optimal performance in certain operations (takeoff, landing and rejected takeoff), on a particular mission (Tactical, Logistic Normal, Logistic Heavy, dependent on the aircraft weight), while operating on a runway of considerable roughness.

Said roughness profiles are based upon British military standards (DEF-STAN). In particular, DEF-STAN 00-970 Leaflet 305/2: *Design of undercarriages - Operation from surfaces other than smooth hard runways. Specification of continuous ground unevenness*, is the relevant one.

Leaving aside discrete obstacles such as bumps or steps to analyse dynamic loads in taxi trials, the text following this regulation is concerned about the specification of continuous ground unevenness. The aim of this problem is to set a basis for design, to give clearance and to set a relationship between design or clearance standards and the potential results yielded after operating in any surface.

To quantify the ground unevenness, the variation of height along the x and y position, $h(x,y)$, is considered. PSD approach is utilised along with the identification of individual runway features to tune this parameter.

Runways are classified into four categories beforehand depending on their level of unevenness, ranging from smooth-paved to unpaved. The function *h(x,y)* results by multiplying each vertical coordinate by a suitable factor, depending on the type of runway the analysis is carried out.

In the following table, the relation between the different roughness profiles, missions, weights and operations is summarised regarding the military certification.

		Manoeuvre		
		Landing	Takeoff	RTO
Mission	Tactical (TLL-1)	DEF-STAN B		DEF-STAN A
	Logistic Normal (LN-1)	DEF-STAN A		San Francisco 28R
	Logistic Heavy (LH-1)	San Francisco 28R		Blagnac

Table 1.1 A400M military requirements

Following the summary displayed above, the roughest theoretical runway the A400M is capable of operating in is the DEF-STAN B, followed by the DEF-STAN A. The relation between these two runways is a factor of 1.5, so that DEF-STAN B is equal to 1.5 times DEF-STAN A. Note that the required factor to obtain the DEF-STAN B runway profile is 1.5, whereas 1 for DEF-STAN A.

Note that for landing conditions the maximum landing weight is taken into account, whilst the maximum takeoff weight or fraction of it is considered for takeoff or rejected takeoff missions. It is remarkable to mention that the rejected takeoff mission is not modeled as a failure case but as a extraordinary case.

Recall that San Francisco 28R is the approved runway to comply with civil regulations. The roughness profile of said runway is less severe than the pair of DEF-STAN profiles. Blagnac runway profile is acknowledged to be the least critical among those displayed in Table 1.1.

When evaluating taxi loads in rejected takeoffs in the case of the A400M, Airbus has a policy, which is not included in any regulatory agreement, stating that the aircraft weight has to be that considered in takeoff missions. However, the maximum theoretical runway profiles to cope with should be those specified for takeoff cases but reducing one degree of severity. For instance, instead of operating in DEF-STAN B for a given mission, the A400M should perform in DEF-STAN A runways. Likewise, DEF-STAN A is substituted by San Francisco 28R and the latter by Blagnac runway.

1.3 Operation in unpaved surfaces

Taxi operations are characterised by the excitation of the aircraft normal modes as a consequence of operating in a surface of a considerable roughness profile. Depending upon the taxi speed, a tuning between the aircraft normal modes and roughness excitation may provoke an amplification of the response and the appearance of dynamic loads [2]. The elements which have direct bearing on the problem are the landing gear, the nose fuselage and wing down bending.

When it comes to analysing dynamic loads in unpaved surfaces, one requires to take into consideration the roughness profile where the taxi operation takes place. Bear in mind that the roughness profile of an unpaved surface might be more severe than the one corresponding to a paved surface [16]. Because of that, the amplification of the response and the ensuing dynamic loads might be intensified.

In order to quantify the severity of a given runway or to study the landing gear performance in an unpaved surface, concepts such as EBH or flotation capability may come in handy.

To assess the severity of a specific roughness profile the Equivalent Bump Height (EBH) approach is used. It was developed by BAe (former British Aerospace) and defines runway profiles in terms of their similarity to a 1-cosine bump.

Mathematically, it is expressed as follows:

$$EBH|_{x(i)} = \frac{\sum_{j=1}^{N}[n_x(x(i+j)-x(i))+n_z(z(i+j)-z(i))]0.5(1-cos(2\pi j/N))}{\sum_{j=1}^{N}[0.5(1-cos(2\pi j/N))]^2} \tag{1.4}$$

It determines that for any wavelength $\lambda = x(i+N)-x(i)$, a 0.5 (1-cosine) mask is translated (convolution) through the original runway roughness profile length to establish the correlation of the local profile with the 1-cosine bump. It is based upon the least squares method. Note that N depicts the number of steps the wavelength λ comprises.

In other words, it determines the existing correlation between the height and length or wavelength an obstacle could present. The EBH graphs depict the variation of the highest height resulted after fitting the local profile to a 1-cosine mask versus the corresponding wavelength.

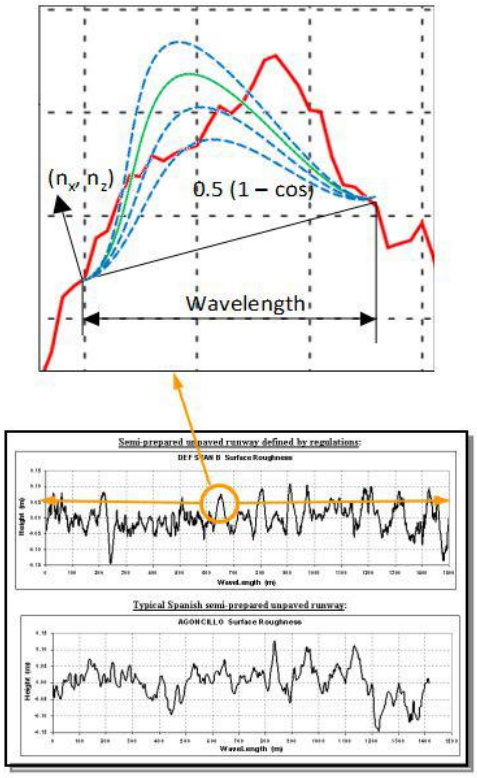

Figure 1.9 Equivalent Bump Height physical insight

Note that it does not provide a roughness profile itself as a way of stating a certain height for a given runway longitudinal point. This approach only provides information about the maximum EBH for each wavelength. The EBH curve does not depict the runway position where the maximum EBH value is located.

Indeed, when giving clearance to operate on a specific runway, the most critical bump the surface presents is plotted along the EBH curve. This acts as an aid to decide whether repair works to flatten the surface should take place, if the critical bump appears to be located in a zone within the EBH curve where safe operations may be compromised.

In Figure 1.10, different EBH curves are plotted for several runways, including Francazal with the addition of a 1-cosine bump, Francazal itself, paved San Francisco 28R, Blagnac and the two regulatory standards: DEF-STAN A and DEF-STAN B. Following the regulations established in Section 1.2, notice how the DEF-STAN B EBH profile is equal to the DEF-STAN A EBH profile multiplied by a given factor (1.5).

It can be appreciated that Francazal runway including a 1-cosine bump presents the highest EBH when the wavelength is around 20m. This particular section is the most severe among

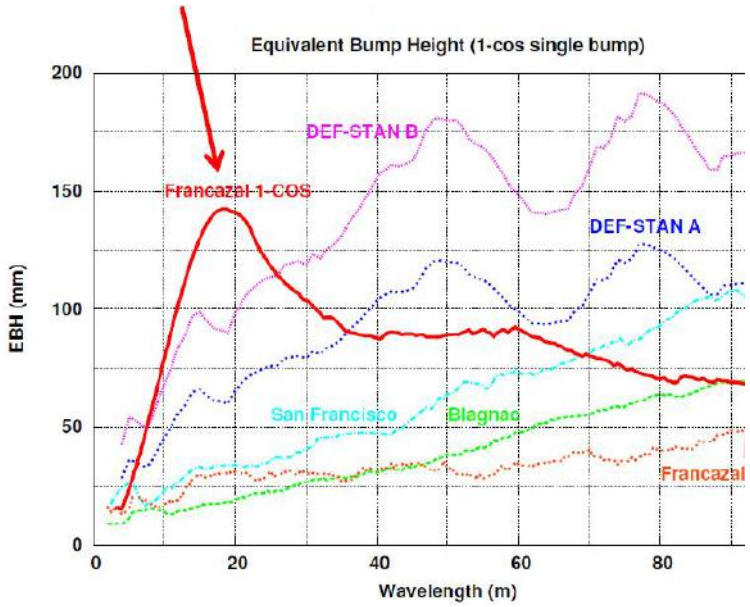

Figure 1.10 Equivalent Bump Height example

the other runways depicted, since the EBH at that given wavelength is higher than DEF-STAN A overall EBH values and surpasses those of DEF-STAN B at said wavelength value.

In the same fashion, the inverse engineering problem is also proposed. An aircraft EBH curve is computed to establish the boundary the specimen is able to operate. If any runway EBH curve overpasses the one obtained in relation to the aircraft taxi capability, this indicates that the aircraft may not be able to taxi in that particular runway without exceeding limit loads. Note that the EBH method is conservative, there might be a possibility to outreach limit loads in the latter case described. Oppositely, if any given runway EBH curve lays below the aircraft EBH curve, it determines that said aircraft will be able to operate in such runway successfully.

It can be concluded that the EBH approach provides a direct measurement of the degree of severity of any runway and the magnitude of the dynamic loads that precedes in operation.

Further concepts to be defined which are suitable to gather an overall view of taxi operations in unpaved surfaces include Flotation Capability. This concept is related to the runway surface hardness.

The flotation capability is the capacity of a given aircraft to operate in an unpaved runway surface of a given hardness. It is usually measured as the number of passes an aircraft can perform on a runway before repair works are needed. The soil hardness is determined by

means of the California Bearing Ratio (CBR). The surface hardness of a runway is measured by means of a cone penetrometer manually, measurements are taken along the runway surface.

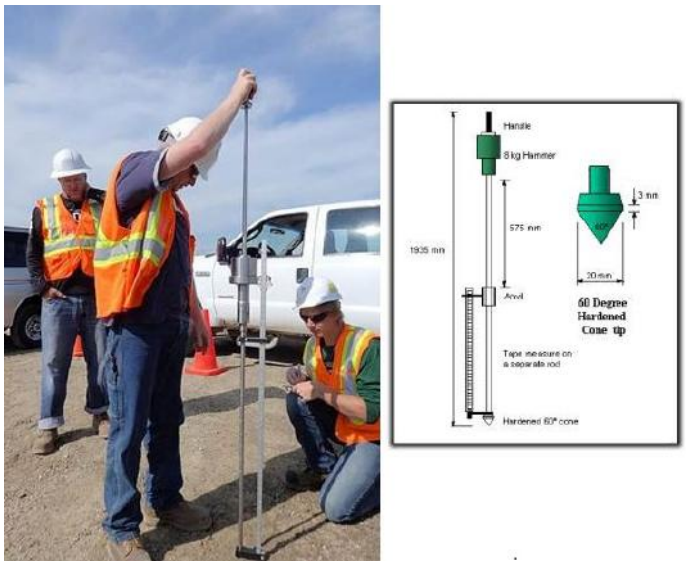

Figure 1.11 Penetrometer

Furthermore, the wheel load, which is dependent on the aircraft weight and determined by the aircraft dynamic response, and the tyre contact area and footprint space, which are related to the tyre inflation pressure, are two remarkable aircraft features which contribute to the concept of ground flotation.

To give some insight, let us focus on a particular aircraft weight, runway roughness and nominal tyre pressure. These magnitudes provide a certain flotation capability as well as certain wheel loads and tyre deflections. The flotation capability can be increased by diminishing the tyre pressure, so that the tyre contact surface is increased.

However, there is a limit when it comes to ameliorating the flotation capability: the tyre pressure cannot be decreased as much as desired. The minimum tyre pressure value is defined by the tyre bottoming phenomenon. Whenever the tyre pressure is reduced, the tyre stiffness and the allowable deflection capability are also shrunk. At any events where these factors come into play, tyre bottoming may occur. These might lead to a wheel stiffness increment with the ensuing wheel loads amplification. Since the deflection capability is worsened, the tyre rubber might get attached to the wheel rim during taxi operations.

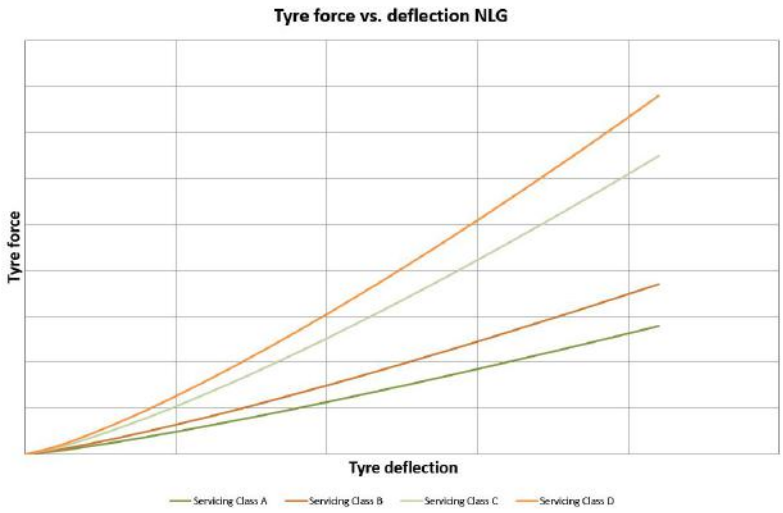

Figure 1.12 Tyre force versus deflection curve, A400M Nose Landing Gear

As it is appreciated in Figure 1.12, the tyre force (proportional to tyre pressure) increases at the same time the tyre deflection grows. The tyre force is modeled by the following expression:

$$F_R = K\delta_r{}^N \tag{1.5}$$

K and N depend on the tyre pressure and δ_r represents the tyre deflection. It should be noted that when increasing the flotation capability, hence reducing the tyre pressure or tyre force, the suitable tyre deflection required to overcome loads is limited to lower values. Consequentially, the ability to adjust to the terrain by deforming the tyre accordingly to each condition is aggravated. In the worst cases (reduced tyre force), the tyre presents no room to deform.

Servicing Classes are established as a way to obtain an optimum flotation capability for a given aircraft mass state and roughness profile. The tyre force and deflection curve is plotted in Figure 1.12 for four Servicing Classes. The Servicing Classes specify the recommended tyre pressure required for each classified set of conditions. In the case of the A400M, the Servicing Classes range from A to D (A: Extra Low Pressure for Maximum Flotation, B: Low Pressure, C: Normal Operation and D: Overpressured). Each category is determined by the combination of a certain aircraft weight and runway roughness.

Besides, flotation charts also provide information relating the aircraft weight and Servicing Class with the runway CBR and number of allowed passes to perform in said runway without having to perform repair works.

Surface roughness profile, CBR, soil compactness or softness constitute the principal features to take into consideration when analysing taxi loads. Another noteworthy phenomenon to consider is the fact of taxiing over recent ruts. Meteorological as well as ambient conditions may modify the runway roughness profile and soil compactness. Hence, the ability to make ruts of considerable dimensions may be enhanced by these factors.

Taxiing over ruts constitutes an added problem. The local surface roughness has completely changed from what was previously studied, the CBR may also vary. Likewise, it might be the case that the Servicing Class is not the appropriate one for that determined condition.

The risk of getting a landing gear component partially buried all of a sudden may intensify the risk of reaching or exceeding limit loads.

Figure 1.13 Limiting case: partially buried landing gear

In short, the flotation capability problem is twofold: runway degradation and the fact of getting selected aircraft components sunk into the runway surface. The first is related to the number of passes (statistical level) an aircraft could perform until repair works are necessary to be executed. The second is associated to the aircraft structural integrity. If the landing gear gets stuck into ruts, it may be required to tow the aircraft back to a compact runway area free from problematic ruts. The critical and limiting case is found whenever the aircraft comes to a halt instantly by getting the landing gear partially buried into runway ruts. This episode may provoke the landing gear to fracture.

An Aircraft Technical Specification is issued by OCCAR and Airbus regarding the A400M flotation capability. It specifies the number of allowed passes for a given CBR, aircraft weight, total deceleration, tyre deflection and centre of gravity settings. It is remarked that one pass is the equivalent of operation of one takeoff or one landing.

1.4 Available test results

A taxi test campaign for the A400M was launched by Airbus in 2010. These test trials took place in Francazal airfield, near Toulouse in August 2010 [17]. The main objective was to validate the A400M dynamic taxi loads model. The aircraft subjected to analysis was A400M MSN2, which constituted the second prototype of said airplane series.

Toulouse Francazal runway consists of a paved surface whose roughness profile was measured beforehand. Standard obstacles were placed in the middle of the runway to evaluate the performance of the aircraft.

Three types of obstacles were utilised: a single 20 meters long 1-cosine bump to approve the dynamic taxi loads model, a single repair-plate to mimic the existence of a single impact and a single step to test the tyres deformation [17].

Multiple runs over each obstacle were performed modifying the aircraft speed, brakes application, centre of gravity configuration and aerodynamic and propulsive settings.

For this particular taxi campaign, one specific run over the 1-cosine bump was highlighted since critical values were obtained for wing down bending moment and nose landing gear vertical force. Said run was executed with forward centre of gravity configuration, activated braking and reverse thrust, medium speed, flaps deflected 15º and deployed spoilers [17].

Figure 1.14 1-cosine bump, Francazal taxi campaign

The magnitudes which were mainly monitored include vertical forces at nose landing gear and front right main landing gear legs, as well as wing tip vertical acceleration, front fuselage shear force, wing root bending moment or wing root torsion moment [17]. The experimental data retrieved was compared with the results gathered after performing a numerical simulation. A good match yielded. Therefore, certification loads were also obtained.

Moreover, it was determined [17] that the contribution of 1P incremental loads was considered to be insignificant, and that accuracy was gained when comparing tests and simulations whenever the aircraft and landing gear experience heavy loads rather than low.

Two further taxi campaigns were launched. The A400M was tested in two different unpaved runways.

The first taxi test campaign was set in Ablitas airfield, Navarra, Spain in 2013. The runway in consideration is made of gravel.

Figure 1.15 A400M on gravel (left) and grass (right) runway tests

Écury sur Coole airfield consists of an uneven grass runway. It is located in the vicinity of Reims, France. The second taxi campaign was launched in the aforementioned unpaved runway in 2015.

In Chapter 2, a more detailed description of the taxi tests is presented regarding Ablitas and Écury sur Coole trials. The data gathered in these two test trials is significant to check the validity of the numerical model used for taxi operations in unpaved surfaces.

Furthermore, Airbus is planning to perform additional tests on soft runways, in particular sand runways, to explore the boundaries the A400M is able to reach regarding its operation in unpaved surfaces.

Chapter 2

Description of models

2.1 Description of the specimen

The aircraft used in the analysis are the A400M MSN2 (prototype aircraft) and MSN6 (A400M series aircraft). At early design stages, it was established that the A400M series has to guarantee the operation in multiple scenarios. It is certified as a civil and military aircraft. The programme was not only intended to produce a new generation of technologically advanced warfare aircraft but one to cover humanitarian missions as well.

Moreover, the main objective of this programme is to cover the void in military transport. Typically, the aircraft engaged in tactical missions present poor logistic capability. Oppositely, those which are aimed towards logistic missions do not have remarkable tactical features. The A400M presents specific characteristics tailored to meet certain demanded requirements [18]:

High performance in short takeoff and landing as well as reverse thrust is obtained through four 8-bladed TP400 turbo propeller engines. The main powerplant characteristics are displayed below.

Prop. Diam (m)	Max. Power (shp)	Prop. RPM
5.34	11000	655/690, 730, 842

Table 2.1 Powerplant characteristics

Aerial delivery, combat offload and capability to load outsize payload such as tanks or helicopters is possible thanks to the ramp and door located in the rear fuselage. The following table (Table 2.2) provides some figures related to the aircraft dimensions.

Length (m)	45.10
Height (m)	14.70
Wing span (m)	42.40
Cargo Hold Length (m)	17.71
Cargo Hold Height (m)	3.85 – 4.00
Cargo Hold Width (m)	4.0
Cargo Hold Volume (m^3)	340

Table 2.2 A400M overall dimensions

Figure 2.1 A400M sketches

Given that the propeller radius is large, the A400M possesses high wings, enhancing, thus, loading operations on ground.

In order to reduce the interference of the propeller flow in the horizontal tail plane, the aircraft is constituted of a T-tail. In addition, the T-tail improves the aircraft manoeuvrability by means of the elevator.

Its cargo capabilities enable the aircraft to be loaded with pallets, trucks or even to handle medical evacuations. In the following table, weight characteristics are shown.

MTOW (kg)	MLW (kg)	MPL (kg)	MFW (kg)
141000	122000	37000	50500

Table 2.3 Weight characteristics

The A400M fleet can fly at high altitudes. They present the capability to cover extensive distances, as it can be appreciated in the table below by looking at the *Range* value, even considerably loaded. These global performance characteristics enable the aircraft to fulfill strategic, tactical and logistic missions. Further aircraft performance features can be found below.

Cruise Mach	Cruise altitude (ft)	Range (km)
0.45-0.72	37000	4535-8700

Table 2.4 A400M overall performances

The operation in unpaved runways is included within the tactical mission performance capability the A400M presents. The A400M is designed to operate in austere airfields and unpaved and size-limited runways. Specifically, the tactical operation upper threshold is set at the conditions described in the following lines. It is able to operate in any short, soft, uneven and unpaved CBR 6 runway no more than 750 metres, carrying 25T of payload and the equivalent fuel quantity needed to cover a 500nm return trip distance.

The A400M series possesses a nose landing gear and a six-leg main landing gear. The nose landing gear can be depicted as a telescopic leg, whereas the main landing gear legs as articulated ones.

Specifically, the nose landing gear shock absorber is composed of two chambers mainly: a low pressure chamber and a high pressure chamber which is activated in critical circumstances, to overcome high loads.

The main landing gear is divided into forward, mid and aft sections, distributed into right and left part. The shock absorber installed in each main landing gear leg presents a single chamber. All the braking action takes place in the main landing gear. An automatic braking system is incorporated as well.

2.2 Introduction to the dynamic taxi loads model

2.2.1 Aircraft structural model

In order to represent the aircraft stiffness and degrees of freedom, a linear and flexible model is considered. To do so, FEM techniques are used. The structural model is representative of the aircraft mode shapes and frequencies up to a cutoff frequency of 50Hz. The model was validated by the Ground Vibration Test (GVT).

The structural model reproduces accurately the load path of the structure and the stiffness characteristics of the lifting surfaces, engine and engine mounting system, control surfaces and fuselage.

Figure 2.2 Aircraft structural model

Depending on the level of symmetry which the dynamic case presents (external factors may contribute to the application of rudder or aileron deflections, for instance, inducing asymmetries in the problem), the structural model in use can be half symmetric to consider symmetric cases or full aircraft to account for any asymmetry that may arise during the analysis.

As a matter of fact, the structural model which is selected to analyse taxi cases in unpaved runways corresponds to complete aircraft model. The reason behind this is to capture all asymmetric responses which might arise during the tests. These are mainly due to the heterogeneous and exacerbated roughness profile unpaved runways present. Further dynamic cases such as lateral gust also considers a full aircraft structural model since the loads acting on the structure contribute to inducing asymmetric responses.

On the other hand, dynamic landing analyses or vertical gust cases make use of a symmetric aircraft model as the loads acting on the structure are aimed to provoke longitudinal, hence, symmetric responses.

The model considers the masses to be CONM2 lumped masses. Bear in mind that lumped masses contain information about the represented mass itself, centre of gravity, moments of inertia and a reference point to which the mass is allocated. The CONM2 entries also provide the identification number of the grid point to which the mass is connected.

Since the CPU time is an important constraint when it comes to the computation of the aircraft normal modes, the model is condensed by means of applying the superelement method, without losing accuracy. The A-set is chosen by selecting points with masses,

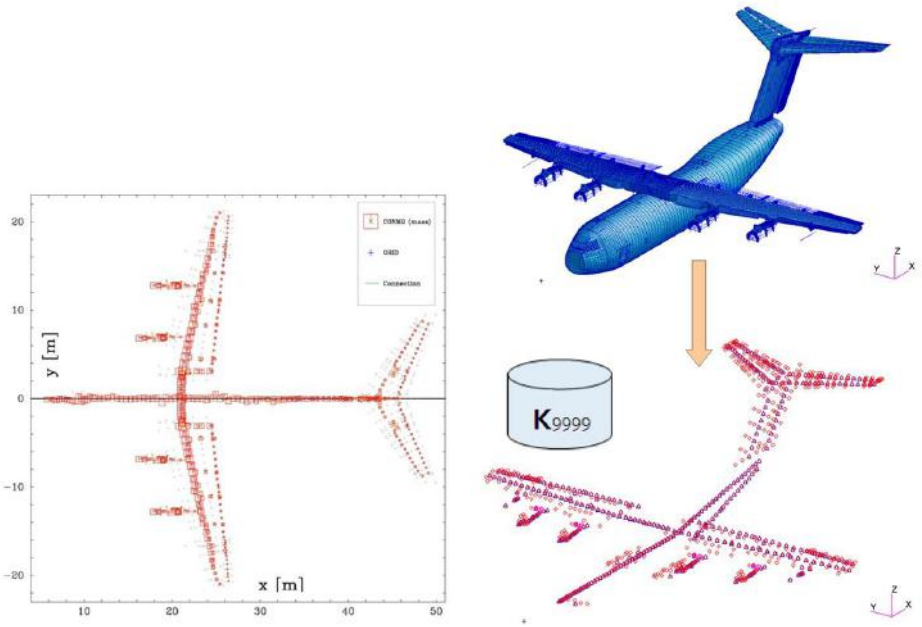

(a) Aircraft mass model (b) Model condensation

Figure 2.3 Mass model and model condensation

applied loads, those required for interpolation or interfaces. This matrix, A-set, is the result of the model condensation. A residual structure, O-set, is also provided.

2.2.2 Landing gear model

The landing gear model [8] takes into consideration all the nonlinearities that the shock absorbers and tyres introduce into the problem. The landing gear non-mobile parts flexibility is not included. The landing gear model was verified and validated by drop tests and free extension tests.

As a matter of fact, the tyres are represented as nonlinear springs perpendicular to the runway profile. Only one contact point with the ground is considered at a time. Moreover, it is remarkable to mention that the force exerted on the tyres depends directly on the deformation, K_{r1}, K_{r2} and N; where K_{r1} is related to the tyre pressure, K_{r2} depends on the plasticity characteristics of the rubber and N has to do with the tyre pressure value.

In the same fashion, the shock absorber force is dependent upon the oil force, gas force and friction force. The liquid (oil) force consists of the force acting whenever the piston expands or compresses. The gas force models the general shock absorber behaviour. Moreover, the polytropic compression which may result whenever the system requires an immediate action

is represented by this model. Care must be taken when selecting the convenient polytropic gas constant γ. Recall that $\gamma = 1$ is used to model a static action whilst $\gamma = 1.4$ or $\gamma = 1.5$ to represent a dynamic one. Finally, the friction force is dependent upon the latter two described forces and the piston dynamic friction coefficient, as well.

Note that the nose landing gear shock absorber presents a double stage chamber (high pressure and low pressure) compared to the single chamber (low pressure) which the main landing gear shock absorbers have. Furthermore, the reference gas pressure value regarding the nose landing gear and main landing gear low pressure chambers is distinct. In short, the shock absorber deflection is given by the following formula:

$$\delta_a = \frac{V_0}{S}\left[1 - \left(\frac{P_0 S}{F_g}\right)^{\frac{1}{\gamma}}\right] + \frac{V_1}{BS}\left[\frac{F_g}{S} - P_0\right] \tag{2.1}$$

The first term is applicable to first stage whilst the second one models the second stage followed by the shock absorber, if any. The deflection is dependent upon the initial gas and liquid volume, piston area, initial gas pressure, polytropic gas constant and bulk modulus. Note that the initial gas pressure P_0 and liquid volume V_1 change from flight to flight and they might be required to be adjusted in the numerical simulation.

Besides, it is important to determine the points where the loads acting on the landing gear are transmitted to the aircraft structure. Said points correspond to the so-called pintle points or landing gear to fuselage attachments.

The following figures depict the rigid landing gear model for the nose landing gear and main landing gear compared to the respective MSC.ADAMS FE model.

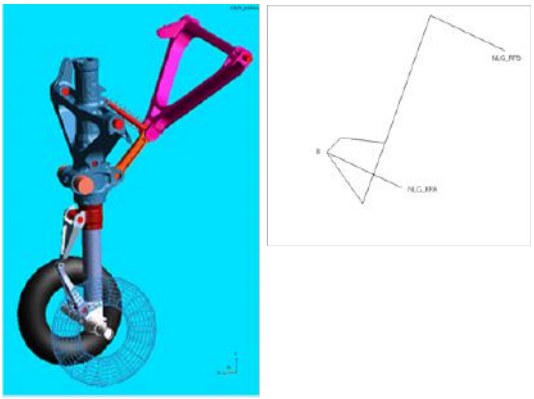

Figure 2.4 MSC.ADAMS NLG model and rigid NLG model

The nose landing gear rigid model provides information about what occurs in the interface between movable and non-movable parts. These points are denoted by letters A and B.

In the same manner, the main landing gear rigid model also considers the effects on the interface between movable and non-movable parts. Moreover, the effects on the upper, lower, longitudinal and lateral links are included.

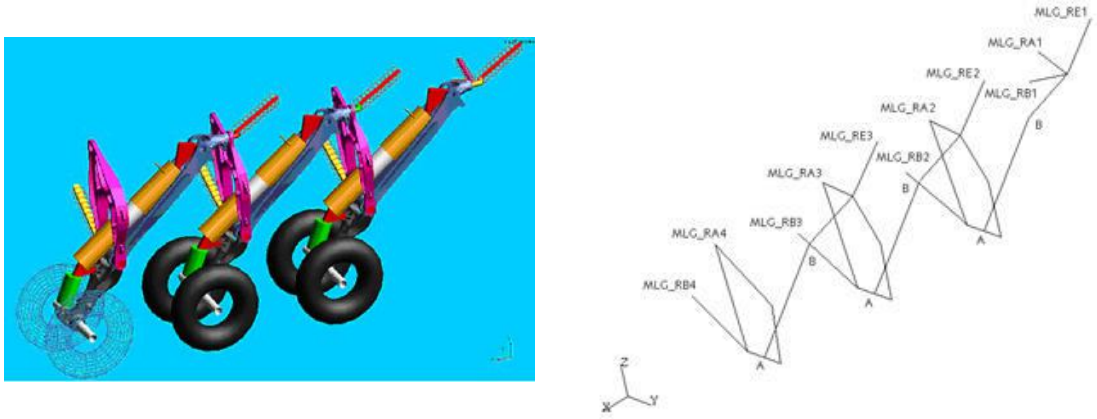

Figure 2.5 MSC.ADAMS MLG model and rigid MLG model, right part

Indeed, notice that the points where the loads are required to be determined are the pintle points. Once there is information about the forces acting on the landing gear movable to non-movable parts interface, those can be transferred to the pintle points by means of a transformation matrix.

In Figure 2.5 the schematic of the main landing gear MSC.ADAMS and rigid model can be appreciated. A1 is the nomenclature followed to name the upper link; B1 to designate the lower link; A2, A3, A4 are the identification names for the panel attachments, B2, B3 and B4 represent the lateral links and the longitudinal links are assigned by letter E.

2.3 Description of the taxi tests

Three different taxi test campaigns have been carried out. The airfields in consideration were Francazal, Ablitas and Écury sur Coole. Bear in mind that the test trials which have been performed in Francazal were used to validate the taxi model. Recall that simple obstacles were placed in said paved runway to analyse the aircraft response.

Particularly, the focus is set on the tests which took place in Écury sur Coole and Ablitas. The aircraft taxi capability was assessed in the latter unpaved runways. Furthermore, it

should be noted that these campaigns were not launched with the unique purpose of studying the aircraft response when taxiing over unpaved surfaces. The aircraft handling qualities and performance were evaluated as well. Besides, analyses on soil particles impacting the aircraft structure were performed. The detrimental problem of engine dust ingestion was also surveyed.

Écury sur Coole is an airfield located in the vicinity of Reims, France. This grass runway is 1500m long and 150m wide, its elevation is around 321 metres above mean sea level. The runway denominator is 04/22.

Figure 2.6 Écury sur Coole airfield

Ablitas aerodrome is located in Navarra, Spain. The runway is made of gravel and is 1800m long. The runway elevation is 324 metres above mean sea level and the denominator is 13/31.

Figure 2.7 Ablitas aerodrome runway

A set of taxi runs were performed with different configurations. The aircraft payload, fuel quantity, aerodynamic and propulsive settings as well as brake application and centre of gravity arrangement were varied along the test campaigns.

The taxi runs were performed after landing or prior to takeoff. When considering the first case exposed (landing), the effect of spoilers out, flaps in landing configuration, reverse thrust or thrust idle, autobraking or maximum brake application is scrutinised. On the other hand, when studying a taxi case performed before takeoff, maximum thrust condition as well as flaps in takeoff configuration can be representative settings to vary, which will be influential during taxi operation.

Several takeoffs and landings were executed at Ablitas runway in August 2013, and at Écury sur Coole airfield from September 7th to October 2nd 2015, in which the intermediate taxi

phase was being analysed. In total, ten flights have been accomplished in Écury sur Coole taxi campaign, each one composed of more than one takeoff and landing, and ten flights as well in Ablitas campaign, plus the addition of three rejected takeoffs.

In the preliminary stage of the campaigns, the runway itself was evaluated. The roughness profile along with the runway lateral inclination was measured. In order to facilitate the operation during the test campaign, specifically, Écury sur Coole runway was divided into three sectors (without physical separation), namely 04R, 04C and 04L. Furthermore, a total of twenty four parallel lines were measured along the runway length; these will come in handy to establish the position of each leg at a given instant of time. Besides, the CBR was measured throughout the whole runway extension, every sixty centimetres approximately. The local hardness was found to change along the runway surface. Thus, the CBR varied accordingly.

After clearances were duly given, the aircraft was able to begin its operations. The specimen followed trajectography at each instant of time was recorded by means of a GPS system.

Regarding the operations performed in Écury sur Coole runway, given that the aircraft had been operating in a soft runway almost day-to-day and taken into consideration external factors, it is remarkable to point out that many taxi runs were performed partially or totally on previous ruts. The reader should appreciate that these ruts were not included in the original runway topographical study, used to give clearance, since these were formed as a consequence of aircraft operation. This new feature introduces certain level of uncertainty in the aircraft response.

Besides, several repair works were done at the time the tests were performed. That information is also relevant when analysing the aircraft response after the taxi runs, since the roughness profile is not exactly the same as the one which was originally determined. These variations are required to be accounted for when comparing the tests with the numerical simulations.

The tested configurations for taxi after landing operation usually comprised reverse thrust or idle thrust settings; brakes off, autobraking (where not every brake system of each leg may be activated) or full pedal braking, flaps at 47º and spoilers on. The tested landing speeds ranged from 100 to 130 knots.

On the other hand, the taxi run that was followed by a subsequent takeoff was performed at a sequence of velocities 91/102/114 knots corresponding to V1/VR/V2 respectively in the best part of the cases. In addition, flaps were set at 30º and spoilers off.

Several mass configurations were tested. The aircraft weight ranged from 90T to 115T throughout the test campaigns. Variations of fuel weight and payload were crucial to assess the performance at different centre of gravity settings (forward, mid or rearward). To do that, the addition of water ballasts or dead loads was included in several runs.

To record the aircraft overall response and to have a comprehensive view of the output induced by the taxi runs, a series of aircraft components were monitored, as well as representative aircraft characteristics.

The aircraft weight, centre of gravity percentage, centre of gravity Y and Z position, moments and products of inertia (Ix, Iy, Iz and Ixz), water ballasts weight, fuel quantity in different tanks (feed, transfer and centre tanks), cargo hold tank capacity were recorded during the different runs. Moreover, measurements of ground speed, true airspeed, equivalent airspeed, indicated airspeed, static and total temperature and delta-ISA were registered. The aircraft position was recorded by means of a GPS system. The aircraft velocity was also monitored during the different runs.

Pitch and roll attitudes, engine thrust and RPM were also documented. Regarding the aerodynamic surfaces, spoiler, flap, elevator, rudder and aileron deflections were monitored. The shear force, bending and torsion moment variation during the runs were retrieved from several wing and HTP rib sections. The wing-fuselage attachments, three fuselage sections, landing gear links, shock absorber strokes and shock absorber gas pressure were monitored. The acceleration at the wing tips and HTP tips was also recorded.

The monitoring stations are described in further detail in Subsection 2.3.1 *Flight Test Instrumentation used*.

2.3.1 Flight Test Instrumentation used

In order to have a comprehensive view of the aircraft response during the taxi phase, a set of flight test instrumentation is installed in certain aircraft components to record the individual output of each sector to a given excitation.

The flight test instrumentation utilised in Écury sur Coole and Ablitas taxi campaigns is the same as the one provided in Francazal. Bear in mind that the batch of instrumentation

adopted to record the response of the aircraft during the aforementioned taxi campaigns is extensive. The instrumented sections and magnitudes which are listed in the following lines represent a reduced percentage of the total amount of instrumentation which was used during the tests. It should be highlighted that the listed one provides the pertinent information required to analyse taxi cases. The remaining instrumentation, which is not enclosed in this section, was utilised to study further dynamic phenomena.

Recall that the specimens tested during the unpaved runways taxi campaigns were A400M MSN2, prototype, and MSN6, series aircraft. Although the main difference between said specimens lies in the aircraft structure, it should be remarked that the instrumentation used also differed from one aircraft to another. The MSN2 operating empty weight plus flight test instrumentation weight was around 100T, whilst the MSN6 fluctuated around 80T. The 20T flight test instrumentation difference came from the fact that the MSN6 did not have the landing gear instrumented. As a consequence, the MSN6 was utilised to study aircraft actuation at low gross weights (five landings performed at Écury sur Coole campaign out of thirty-two), whereas the MSN2 was tested for larger aircraft gross weight configurations. It should be pointed out that some taxi operation sizing cases are expected to be found at the landing gear, thus, the MSN2 was used for the purpose of analysing the landing gear behaviour during taxi tests, among other activities, since the landing gear was instrumented.

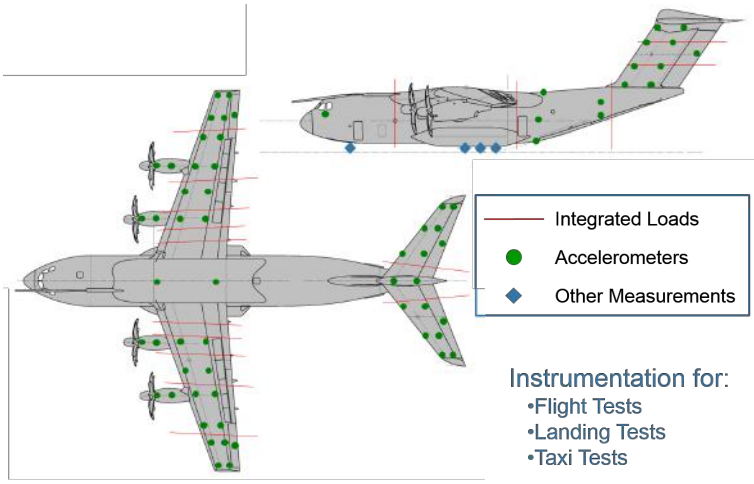

Figure 2.8 Flight Test Instrumentation

The instrumentation set can be split into three main categories: accelerometers, integrated loads and other type of measuring devices. Accelerometers are placed in the aircraft structure itself: wings, fuselage, engines, HTP, VTP and different attachments. Furthermore, integrated loads are located at specific fuselage, wing, HTP and VTP sections. These are also known as monitoring stations.

A monitoring station is a determined aircraft location where the aerodynamic, inertial, ground, engine loads and accelerations are integrated. It is also defined as a point where the resultant load is assessed in terms of forces and moments and a reference system where the integrated loads are referred to. In short, a monitoring station is composed of a grid point, a coordinate system and an area of integration. The reduced set of monitoring stations the taxi campaigns are focused on is listed in Tables 2.5, 2.6, 2.7 and 2.8.

Lastly, other measurements are taken in the landing gear. Table 2.9, 2.10 and 2.11 collect all the information regarding this flight test instrumentation type.

The ensuing table (Table 2.5) collects all the information regarding the condensed set of flight test instrumentation used in the wings. In addition, the wing attachments (right and left) to the fuselage are also instrumented. The magnitude to record is the vertical (shear) force Fz. Table 2.6. provides the collection of rear wing to fuselage attachments which are utilised to analyse the aircraft response. The remaining set of instrumented attachments are not enclosed within this text.

Section	Magnitude
Rib 2/3 L	Fz, Mx, My
Rib 2/3 R	
Rib 5/6 L	Fz, Mx, My
Rib 5/6 R	
Rib 7/8 L	Fz, Mx, My
Rib 7/8 R	
Rib 12/13 L	Fz, Mx, My
Rib 12/13 R	
Rib 19/20 L	Fz, Mx, My
Rib 19/20 R	
Wing tip L	Nz
Wing tip R	Nz

Table 2.5 Instrumented wing sections

Section	Magnitude
WFI_R06	Fz
WFI_L06	Fz

Table 2.6 Wing to fuselage attachments

The instrumented fuselage sections are presented in Table 2.7. Besides, Table 2.8 provides the sections of the HTP which are monitored (and utilised throughout the campaigns) as well as the magnitudes to record.

Section	Magnitude
FUS C30/31	Fz, Mx
FUS C51/52	Fz, Mx
FUS C67/68	Fz, Mx

Table 2.7 Fuselage instrumented sections

Section	Magnitude
Rib 2/3 L	Fz, Mx, My
Rib 2/3 R	Fz, Mx, My
HTP tip L	Nz
HTP tip R	Nz
HTP M00	Mx

Table 2.8 HTP instrumented sections

Following the nomenclature which is used to designate each landing gear component, the ensuing table (Table 2.9) collects the batch of stations and magnitudes that were monitored during the taxi campaigns. Lateral or vertical forces are requested depending on the geometry of the instrumented section. Moreover, the force modulus is demanded in the case of the longitudinal links, upper link, lower link and lateral links. Specifically, when dealing with the response of the longitudinal links (E), the resulting force modulus does not differ much from the horizontal force (Fx, longitudinally directed) due to the geometry of said part.

Consecutively, once the Fx and Fz are obtained in the main landing gear legs wheel axle, the braking coefficient can be directly computed by stating that $\mu = Fx/Fz$.

The landing gear shock absorber strokes and gas pressure are also monitored. The subsequent table (Table 2.11) lists the magnitudes and components to instrument. Note that the nose

Section	Magnitude	Section	Magnitude
NLG_LPA	Fz	MLG_LE3	Fs Mag
NLG_RPA	Fz	MLG_RE3	Fs Mag
MLG_LA2	Fy, Fz	MLG_LA1	Fs Mag
MLG_LA3	Fy, Fz	MLG_RA1	Fs Mag
MLG_LA4	Fy, Fz	MLG_LB1	Fs Mag
MLG_RA2	Fy, Fz	MLG_RB1	Fs Mag
MLG_RA3	Fy, Fz	MLG_LB2	Fs Mag
MLG_RA4	Fy, Fz	MLG_RB2	Fs Mag
MLG_LE1	Fs Mag	MLG_LB3	Fs Mag
MLG_RE1	Fs Mag	MLG_RB3	Fs Mag
MLG_LE2	Fs Mag	MLG_LB4	Fs Mag
MLG_RE2	Fs Mag	MLG_RB4	Fs Mag

Table 2.9 Landing gear overall instrumentation

Section	Magnitude	Section	Magnitude
NLG Wheel axle	Fx, Fz	MLG RFWD Wheel axle	Fx, Fz
MLG LFWD Wheel axle	Fx, Fz	MLG RMID Wheel axle	Fx, Fz
MLG LMID Wheel axle	Fx, Fz	MLG RAFT Wheel axle	Fx, Fz
MLG LAFT Wheel axle	Fx, Fz		

Table 2.10 Wheel axle instrumented sections

landing gear presents two chambers of distinct gas pressure level. For sake of simplicity,*Pg* stands for Gas Pressure. The main landing gear is divided into Right (R) and Left (L) part and subdivided into Forward (FWD), Mid (MID) and Aft (AFT) sections.

Section	Magnitude	Section	Magnitude	Section	Magnitude
MLG RFWD	Stroke, Pg	MLG LFWD	Stroke, Pg	NLG	Stroke, HP Pg, LP Pg
MLG RMID	Stroke, Pg	MLG LMID	Stroke, Pg		
MLG RAFT	Stroke, Pg	MLG LAFT	Stroke, Pg		

Table 2.11 Landing gear instrumentation

Further monitored magnitudes are displayed in the following table (Table 2.12). Recall that the collection provided represents a fraction of the total instrumented and documented magnitudes and sections. These come in handy to analyse and understand the aircraft overall response in taxi.

Magnitude	Details	Magnitude	Details
Weight	Aircraft Water Ballasts L/R Inboard Fuel Tanks L/R Outboard Fuel Tanks L/R Transfer Fuel Tanks L/R Centre Fuel Tank Cargo Hold FWD/AFT	Deflections	Spoilers L/R Flaps Elevator L/R Tail Plane Elevator Trim Rudder L/R Ailerons L/R
CG position	X %CG Y Z	Velocity	GS TAS EAS IAS
CG position through GPS	X Y Z	CG velocity through GPS	Vx Vy
Moments of inertia	Ix Iy Iz Ixz	Aircraft Angles	Pitch Roll Magnetic Heading
CG Accelerations	Nx Nz	Ambient air magnitudes	Total Temperature Static Temperature Delta ISA Air density
Thrust Forces	Inboard Engines L/R Outboard Engines L/R	Engines RPM	Inboard Engines L/R Outboard Engines L/R

Table 2.12 Further recorded data

2.3.2 Flight Test Data Postprocessing

The measurements retrieved from the taxi tests may not be useful as they originally are. In order to convert said readings into meaningful information, an intermediate step must be considered. That is when post-processing tools come in handy. This procedure is divided into two categories: the data conversion made by the Flight Test Department which yields already usable data and the process followed by the engineer to translate certain parameters that are considered to be significant, and needed in the numerical simulation, into relevant information. First, the post-processing followed by the Flight Test Department is described. Subsequently, the procedure pursued by the engineer to convert required data is detailed.

Since plain extensometers do not measure shear forces, bending or torsion moments directly but the structure deflection, an intermediate step takes place to transform the measured

deflections into readable force and moment time histories. The procedure which is utilised for this purpose is the so-called Skopinski method, developed by NACA (National Advisory Committee for Aeronautics, current NASA) in 1954 [19].

The Skopinski method comprises a set of guidelines to measure the shear, bending moment and torque in a given structure. It is based upon the fact that the stress in structural members might not be exactly a simple function of the shear force, bending and torque moment. Calibration procedures [19] are designed to reach the objective of obtaining accurate loads measurements. Those are yielded by combining the output of several bridges numerically.

This method [19] is composed of several calibration stages. In the preliminary one, it is stated that the bridges used to measure the deflections should be oriented as to capture pure shear loads, bending moment or torque, as far as possible. The second stage is concerned with the adequate selection of the points where the calibrated (reference) loads are applied. The third step involves the application of said loads in the previous points, in an incremental manner. Complementary checks are performed during the fourth stage.

On the other hand, further post-processing tools are described in the following lines. In order to obtain the corresponding braking coefficient to each leg, the horizontal (Fx) and vertical (Fz) ground loads acting on the wheels are required. These are the direct measurement gathered after using strain gauges. Said devices are required to be calibrated beforehand, as well. The braking coefficient is specified as $\mu = Fx/Fz$.

Specifically, the vertical and horizontal ground loads acting on the wheels are obtained by means of converting the signals that a set of strain gauges provides. These strain gauges include torsion, bending and tension/compression bridges. Because of that, a calibration procedure is also required by applying ground loads on a calibration rig to the landing gear and getting the calibration matrices. These matrices will link the strain gauges measurements to the ground loads that are being applied to the structure during the flight test campaigns. Note that a wheel reference axis is considered to measure the magnitudes in an orderly and structured manner. Because of that, a set of strain gauges are installed as to measure the response within the established reference axis. The relation between the combined set of strain gauges is also obtained as part of the calibration procedure. Moreover, it is remarkable to point out that different types of strain gauges were used. For instance, to measure the braking effect, a distinct kind of instrumentation was utilised compared to the one proposed to determine the resulting loads in non-braking conditions.

In these particular taxi campaigns, the vast majority of the retrieved data is coherent. Therefore, there was no need to apply low-pass filters to eliminate any incongruity. On the other hand, the unique parameters which present untrustworthy results after post-processing are the shear force and bending moment in the fuselage stations for Écury sur Coole taxi campaign. The given data stabilises into a plateau of considerable magnitude. Said magnitude is established to be as a out of range and unrealistic. Hence, the fuselage shear force and bending moment readings at those sections are discarded out of the analysis.

When it comes to tuning the numerical simulation to the taxi tests, the engineer may be required to perform a post-processing of relevant parameters to achieve the aim. This is the part where spurious signals are removed by applying DSP methods. In the case presented before, to eliminate spurious signals, sampling is employed. Note that it was not required to apply any sampling method to the given data as there was not the case of having spurious signals.

The aircraft trajectography serves as another example in which post-processing is required to be performed by the engineer on duty. The raw data which is firstly given consists of the runway origin GPS coordinates, the runway sub-divisory lines expressed in WGS84 and RGF93-CC49 reference systems and the location of the aircraft centre of gravity, at each instant of time, with respect to the runway origin, expressed in metres. As it may be appreciated, it is required to express all this information with respect to a common reference frame. Particularly, the selected working reference frame is placed at the runway origin. The runway axis is oriented such that the X axis is parallel to the runway length, the Y axis points to section 04L (in the case of Écury tests) and the Z-axis is just orthogonal to the X and Y axes and right-handed.

First, the runway origin GPS coordinates are translated into RGF93-CC49. Afterwards, a transformation of said measurements is needed so that they are expressed in terms of runway coordinates. Once every relevant magnitude to the problem is written with respect to a common reference frame (runway axis), the next step consists in obtaining the corresponding runway roughness profile to each leg.

Due to the geometry the landing gear presents, the runway roughness profile the nose landing gear sees is different to the one used for the right or left main landing gear legs to pass. Because of that, it is significant to determine the exact location of each landing gear section to obtain the appropriate roughness profile for each leg.

On the other hand, data interpolation is required. The original data is retrieved at a sampling rate which particularly does not meet certain accuracy requirements. When it comes to determining the different runway roughness profiles for each leg, it is necessary to get points each half metre in the X axis. Conversely, the sampling rate used to retrieve raw data might provide a point each seven metres in the X axis. In order to achieve a meticulous roughness profile with the aforementioned requirements met, interpolation comes in handy.

In addition, a second interpolation is performed to get an appropriate value of runway height for each leg, in case said leg does not lay on a runway subdivision line.

Further pre-numerical simulation procedures include the selection of a relevant time-window to analyse the aircraft response to taxi operation. Because of that, the runway profiles which are used have to be those corresponding to the instants of time the time-window adopts. In order to properly control the commencement of the aircraft response to any excitation, fifty metres of nil runway height variation are considered at the beginning and end of said runway roughness profile section. For sake of accuracy, the union between the zeros and runway profile itself is smoothed by means of applying a 1-cosine mask.

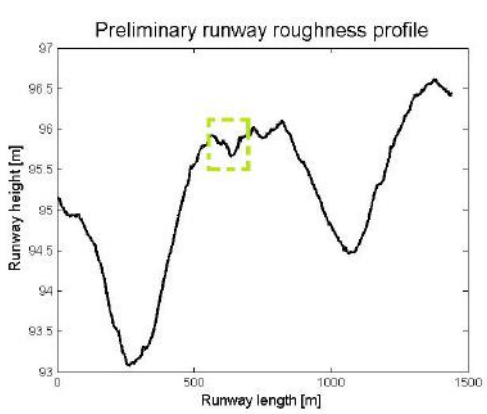

(a)

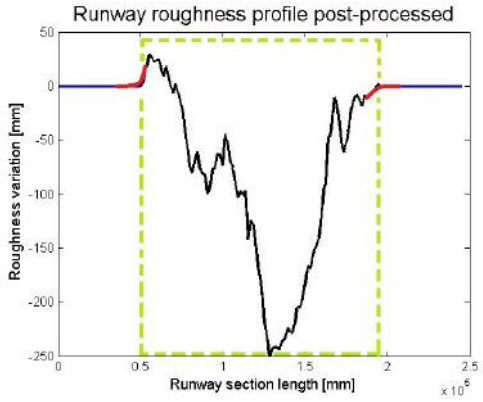

(b) 50m of null roughness profile at beginning and end (blue), 1-cosine mask (red)

Figure 2.9 Runway roughness profile post-processing

The last tool which is covered in this section is the static balance. Said process is aimed to get an overall value of vertical force (Fz_{CG}), roll moment (Mx_{CG}) and pitch moment (My_{CG}) applied at the centre of gravity prior to the computation of taxi loads in the numerical simulation. Indeed, said magnitudes are requested as an input (constant value or time history) in DYNTAXI (please, refer to Chapter 3 for further details).

The solicited force and moments over the centre of gravity result after computing relevant aerodynamic forces and moments, as well as gathering appropriate values for the propulsive and normal forces. In order to do that, the linear aerodynamic model is applicable once the pertinent aerodynamic coefficients are known. Moreover, lateral stability changes may infer in the longitudinal aircraft stability and, hence, in the longitudinal forces and moments.

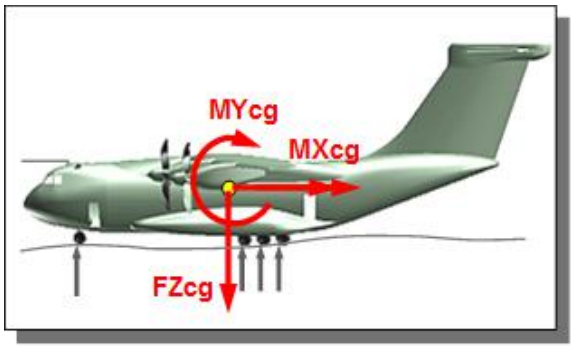

Figure 2.10 Static balance over the aircraft centre of gravity

The aerodynamic coefficients are assumed to be constant as unsteady aerodynamics effects are neglected. As an added perk, the problem is even simplified when analyzing landings in which reverse thrust (or ground idle regime) is included. Note that the aerodynamic coefficients and 1P loads are interrelated: the aerodynamic coefficients vary depending on the value 1P loads reach. When reverse thrust regime is applied, 1P loads value is zero, thus, the duly aerodynamic coefficients correction is not needed to be brought into play.

The lift and pitching moment coefficient equations used, coming from linear aerodynamics, are included below.

$$C_L = C_{L_0} + C_{L\alpha}\alpha + C_{L\delta_e}\delta_e + C_{Lih}ih + \Delta C_L \tag{2.2}$$

$$C_M = C_{M_0} + C_{M\alpha}\alpha + C_{M\delta_e}\delta_e + C_{Mih}ih + \Delta C_M \tag{2.3}$$

δ_e denotes the elevator deflection angle and ih corresponds to the elevator trim angle. ΔC_L and ΔC_M are the coefficients which add the effect of lateral stability in these longitudinal variables. In the case wings were not at level, one of the wings will be influenced by ground effect. This asymmetry based on the existence of a bank angle influences the lift and pitching moment coefficient. Antisymmetric aileron deflection also makes the lift and pitching moment coefficient vary. The latter ΔC_L and ΔC_M coefficients include the aforementioned effects.

Chapter 3

Dynamic taxi loads numerical simulation

3.1 Introduction to taxi loads numerical simulation

Experimental data is gathered by means of performing a series of tests where distinct configurations and operations are assessed. The aircraft response yielded during said tests is attempted to be reproduced by performing numerical simulations.

Throughout this Chapter, the description of the numerical simulation process and underlying assumptions is provided. A brief summary of the process is illustrated in the following lines to get the reader familiar with the software tools employed at introductory level.

At initial stages of the simulation, commercial software utilities such as MSC.NASTRAN are required to obtain the aircraft normal modes. In-house software developed by Airbus Defence and Space subdivision (former Airbus Military, EADS-CASA) such as DYNTAXI, DATLOAD, DYNRESP and DYNLOAD are essential to compute the acting loads on the landing gear movable to non-movable parts interfaces, to translate said loads to the landing gear to fuselage attachments (pintle points), to compute the transient response expressed in modal coordinates and to transform the previous transient response so that it is formulated with respect to the aircraft monitoring stations defined, respectively.

The collection of input parameters which is demanded by each program is extensive and diverse. Each software utility requires the input variables to be implemented in a particular manner. In Section 3.3 *Taxi loads numerical simulation procedure*, a comprehensive description of the tasks which are performed through each software utility is given, along with the list of input and output parameters which each procedural step is comprised of.

3.2 Description of the dynamic taxi loads model

The continuation of Section 2.2: *Introduction to the dynamic taxi loads model* is presented in the current Section by describing the main characteristics and assumptions made which are applicable to the dynamic taxi loads model. The definition of the structural aircraft model, landing gear model and dynamic taxi loads model represents a preliminary step towards the initialization of the numerical simulation.

Before entering into details, it is important to remark that the loads computed through the simulation process can be incremental loads, 1G loads or total loads. Indeed, each software utility outputs the resulting loads either as incremental loads or total loads. Note that total loads result after the addition of 1G loads plus incremental loads. The first group is also known as static loads. In taxi, these are computed by stating an initial condition in which the aircraft runs over an ideally flat runway profile. 1G loads include gravity and steady aerodynamic effects along with 1P steady effects. The second group is associated with the dynamic loads yielded after performing taxi runs over a real uneven runway.

The basic assumptions and methodology followed to get a compelling dynamic taxi loads model are enumerated below.

Along with the aircraft structural model and landing gear model characteristics depicted in Section 2.2 *Introduction to the dynamic taxi loads model*, a full-coupled solution of the linear and flexible aircraft model and nonlinear and rigid landing gear model is considered to get incremental dynamic loads. The coupling method makes use of the aircraft free-free modes to simulate real operating conditions.

To compute the incremental dynamic response with DYNTAXI, the aircraft is assumed to be taxiing at constant horizontal velocity. In taxi cases, the aircraft excitation is provided by the runway roughness profile itself. Moreover, sensitivity studies came to the conclusion that the cutoff frequency the taxi run should present is 40Hz.

Unsteady aerodynamics effects are not considered directly. The alleviation due to unsteady aerodynamics damping is introduced into the damping model. The unsteady aerodynamics damping is modeled as viscous damping. The damping force is given by the following equation:

$$\vec{F} = -c\vec{v} \tag{3.1}$$

c represents the viscous damping coefficient. As it can be appreciated, the velocity plays a fundamental role to size the magnitude the damping force reaches. Such force increases at the same rate velocity does. Extra damping is found at high velocities (V>100KEAS).

On the other hand, the damping model assumes the modal damping to be a function of frequency, and considers the fact that the wing to engine attachment elastomers induce additional damping by means of a loss factor. To do that, a NASTRAN CDAMP2 entry is introduced.

Furthermore, gyroscopic forces at not included in DYNTAXI calculations. They are indeed introduced in DYNRESP. These loads appear at the engines as a consequence of the propellers rotation. Besides, 1P loads[1] and Flight Control System (FCS) laws are neglected from the process.

The Data Recovery approach is based upon the Summation of Forces Method. Contrary to the assumptions the Displacement Method presents: the magnitudes in consideration are recovered as a linear combination of modal coordinates, the Data Recovery approach establishes that a reduced set of modes is just necessary to represent the dynamics of the system. Besides, the response of higher modes to low frequency excitation is found to be static. Thus, the contribution from higher modes to the resulting inertial and damping forces is considered to be negligible. The contribution from lower modes is taken into account, instead. This approach will come in handy in DYNLOAD.

3.3 Taxi loads numerical simulation procedure

Once all the assumptions behind the dynamic taxi loads model, applicable methodology, aircraft model, landing gear model and relevant experimental data are adequately defined, the taxi loads numerical simulation can be launched.

The process pursued is composed of several stages. Particularly, each stage demands a different combination of input variables depending on the job performed and methodology to follow.

The procedure itself is summarised in the following flowchart.

[1] **1P loads** are a result of having a propeller-equipped aircraft whose propeller angle of attack is different from zero. Therefore, a yaw moment is induced. The A400M presents counter-rotating propellers to avoid the yawing moment due to 1P-direct effects.

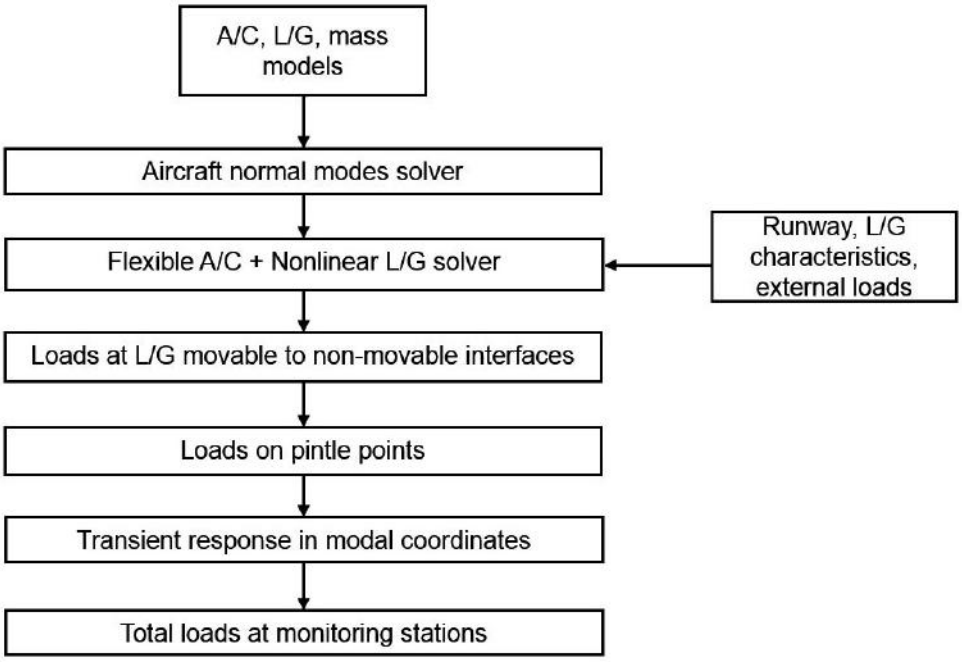

Figure 3.1 Taxi loads numerical simulation procedure

3.3.1 NASTRAN SOL103

The numerical simulation is initialised by computing the aircraft normal modes solution SOL103 with MSC.NASTRAN capabilities. The objective is to obtain the aircraft eigenvalues and eigenvectors together with the six aircraft rigid body modes and flexible modes.

A flexible aircraft FE model including the aircraft stiffness matrix along with a rigid FE model of the non-movable parts of the landing gear and the corresponding mass states are introduced as inputs. Note that the landing gear mass is included within the flexible aircraft model.

3.3.2 DYNTAXI

DYNTAXI routines are divided into two distinct activities: DYNTAXI static balance and DYNTAXI dynamic taxi simulation.

DYNTAXI static balance

The overall aircraft forces and moments applied at centre of gravity (Fz_{CG}, Mx_{CG}, My_{CG}) along with the 1G loads exerted on the landing gear to fuselage attachments (pintle points) and on the wheel axles are computed by DYNTAXI static balance module. This implies that the aircraft is balanced (summation of forces and moments is zero, at equilibrium) by considering a initial condition at $t = 0$ in which a taxi run over an ideal runway is performed.

The input parameters which are required for this purpose are the six complete aircraft rigid body modes yielded from NASTRAN SOL103 analysis, the landing gear properties coming from the characteristics the shock absorbers and tyres present and external forces including propulsive and aerodynamic effects.

The vertical force acting at the aircraft centre of gravity is given by the following expression:

$$Fz_{CG} = L - W - T\sin\varepsilon = \frac{1}{2}\rho V^2 S C_L - W - T\sin\varepsilon \tag{3.2}$$

L represents the lift force, W the aircraft weight, T the total engine thrust and ε the angle of thrust. C_L is given by equation (2.2).

The pitching moment over the aircraft centre of gravity is approximated by the formula below. Propulsive and aerodynamic effects are taken into account.

$$\begin{aligned} My_{CG} = {} & \frac{1}{2}\rho V^2 S C_M MAC + L(x_{CG} - x_{aero}) + D(z_{aero} - z_{CG}) + \\ & + T\cos\varepsilon(z_{CG} - z_{eng}) + T\sin\varepsilon(x_{CG} - x_{eng}) - \mu_{NLG} N_{NLG} z_{CG} - \mu_{MLG} N_{MLG} z_{CG} \end{aligned} \tag{3.3}$$

C_M is given by equation (2.3), the drag force is denoted by D, the total thrust is represented by T and the mean aerodynamic chord is expressed as MAC. μ_{NLG} and μ_{MLG} denote the applicable friction coefficient found in the nose landing gear and main landing gear, respectively. Likewise, N_{NLG} and N_{MLG} represent the normal force acting on the aforementioned landing gear components. The difference between the location where the lift, drag and thrust forces are applied and the aircraft centre of gravity is required to calculate the total pitching moment about said point.

The rolling moment about the aircraft centre of gravity is computed by including the asymmetric effects induced by the ailerons and the variation of the bank angle.

$$Mx_{CG} = \frac{1}{2}\rho V^2 S C_l MAC - L(y_{aero} - y_{CG}) + T\sin\varepsilon(y_{CG} - y_{eng}) = \\ = \frac{1}{2}\rho V^2 S(C_{l\delta_a} + C_{l\phi})MAC - L(y_{aero} - y_{CG}) + T\sin\varepsilon(y_{CG} - y_{eng}) \quad (3.4)$$

MAC represents the mean aerodynamic chord, C_l the rolling moment coefficient, $C_{l\delta_a}$ the aileron contribution to the rolling moment and$C_{l\phi}$ the bank angle contribution to the rolling moment. To compute asymmetric loads, a complete aircraft model is needed.

In short, the input data required by DYNTAXI static to calculate the loads acting at the aircraft centre of gravity include the aircraft mass, centre of gravity X, Y and Z positions, braking coefficients, total engine thrust and RPM, aircraft speed, pertinent aerodynamic coefficients to get C_L and C_M, aerodynamic surfaces deflections (flaps and spoilers) and ambient conditions.

Further loads computations include the calculation of 1G loads on pintle points and wheel axles. To do that, the landing gear characteristics such as leg type, location, shock absorber parameters (gas pressure, oil volume), tyre characteristics, wheel axles locations or movable to non-movable parts interface points are required as input parameters.

DYNTAXI dynamic module

The coupled system of equations given by the linear aircraft model and nonlinear landing gear model (equations (1.1) and (1.2)) is solved in the time domain. The landing gear characteristics along with the shock absorber and tyre features are demanded as input parameters. Moreover, the corresponding runway profile to each leg, the aircraft overall taxi speed (assumed to be constant during the run), Fz_{CG} and My_{CG} given as constant punctual values or time-histories, Mx_{CG} constant value, eigenvalues, modal matrix, generalised stiffness matrix and generalised mass matrix are also required as input parameters.

The resulting total loads are retrieved as time-histories of loads acting on tyres, shock absorbers or movable to non-movable parts interfaces.

In fact, the dynamic analysis can be defined as a static balance problem where inertial terms are included at each instant of time. The main difference between the static balance and the dynamic analysis lies in the fact that the initial geometric conditions are given by the

user in the first case, whilst the second case computes said initial conditions by taking into consideration the historical record of previous initial conditions in precedent instants of time. The dynamic process is iterative.

3.3.3 DATLOAD

The loads applied at the landing gear movable to non-movable parts interfaces are the output parameters coming from DYNTAXI. Said loads are required to be translated to the landing gear to fuselage attachments, instead. The reason behind this is related to the fact that the aircraft response is dependent upon the overall response the landing gear presents when taxiing. The only way to introduce the landing gear contribution to the aircraft structure is by applying said contribution to the points where the landing gear and aircraft structure are connected. These are the so-called pintle points.

The translation of said loads to the pintle points is performed by means of a conversion matrix. Note that the resulting loads are total loads (1G plus incremental loads). On the contrary, the next step in the simulation demands the loads acting on the pintle points to be expressed as incremental loads. Because of that, the current stage is also devoted to subtracting 1G loads to the total loads in order to prepare the next step required input in a suitable way for DYNRESP.

3.3.4 DYNRESP

The transient response to incremental loads acting on the pintle points is computed in the frequency domain with DYNRESP. The aircraft response is expressed in modal coordinates. The input parameters required by the solver consist of the solution to NASTRAN SOL103 stage, damping and gyroscopic effects.

3.3.5 DYNLOAD

Total loads at the aircraft monitoring stations and corresponding time histories are computed with DYNLOAD. The Summation of Forces Method is used, 1G loads are added to incremental loads to get total loads. The modal transient response obtained in the previous step is required in the present simulation stage to compute total loads at monitoring stations. A list of predefined monitoring stations is given as an input. Total loads at the aircraft monitoring stations cannot be computed with DYNTAXI directly, therefore, the process is split into two routines: DYNRESP and DYNLOAD.

In the following table, a summary of the processes involved in the simulation together with the respective inputs and outputs required by each step is illustrated.

Step	Inputs	Outputs
NASTRAN SOL103	A/C structural flexible FE model Stiffness matrix Rigid FE model non-movable part L/G Mass states	Eigenvalues Eigenvectors Rigid body modes Flexible modes
DYNTAXI (static)	A/C mass X_{CG} (%MAC), Y_{CG}, Z_{CG} μ_{brakes}[2], μ_{roll} Total thrust and RPM Speed (TAS, KTAS, KEAS) C_D, C_{L0}, $C_{L\alpha}$, C_{Lih}, $C_{L\delta_e}$ C_{M0}, $C_{M\alpha}$, C_{Mih}, $C_{M\delta_e}$ ih (º), flaps and spoilers deflection Altitude, air density, ISA offset Landing gear geometry and location Tyre properties and wheel axles location Movable to non-movable parts interface location Shock absorber parameters	Fz_{CG} Mx_{CG} My_{CG} 1G loads pintle points 1G loads wheel axles
DYNTAXI (dynamic)	A/C normal modes Fz_{CG}, Mx_{CG}, My_{CG} (external forces) Inertia A/C manoeuvre and configuration Runway profiles μ_{brakes}, μ_{roll} Landing gear geometry and location Tyre properties and wheel axles location Movable to non-movable parts interface location Shock absorber parameters	Total loads at movable to non-movable parts interfaces Total loads at shock absorbers and tyres
DATLOAD	Total loads at movable to non-movable parts interfaces	Incremental loads at pintle points
DYNRESP	A/C and L/G FE models Damping and gyroscopic models Incremental loads at pintle points	Incremental loads in modal coordinates
DYNLOAD	Monitoring stations 1G loads Incremental loads in modal coordinates	Total loads at monitoring stations given as time-histories

Table 3.1 Summary of the procedure followed by the taxi loads numerical simulation

[2]The braking coefficient can be either introduced as a single value for all main landing gear legs or as a list of six (different or not) braking coefficients, each referring to a particular main landing gear leg.

Chapter 4

Preliminary analysis of results

In this Chapter, the comparison between the experimental and numerical response of selected aircraft components is analysed. Specifically, the experimental data obtained through taxi tests is primarily selected from Écury sur Coole taxi campaign.

On the other hand, the numerical response is retrieved after performing a numerical simulation. The process of response (numerical to experimental) matching is laborious, since a collection of adjustments are required to be introduced at a time to improve the quality of the results.

The chronological development of tasks which are needed to tune the numerical response, with the purpose of reproducing with high fidelity the experimental response gathered through the campaign, is described herein.

Hard constraints such as time or computing resources are taken into consideration, as well. Because of that, the number of taxi cases and time-windows to analyse should be filtered so that remarkable cases and phenomena should be studied, solely. The criteria to select these noteworthy cases and time spans are presented in the following lines.

4.1 Selection of relevant taxi cases and time-windows

Écury sur Coole taxi campaign comprises thirty-two landings, out of which twenty-seven were performed by A400M MSN2 and the remaining five by A400M MSN6. The focus is set on the taxi runs in which the landing gear was instrumented. Therefore, the twenty-seven landing operations carried out by the A400M MSN2 are analysed at preliminary stages to shortlist a reduced number of them afterwards, based on established criteria, to simulate the aircraft response numerically.

The amount of data gathered during the tests performed by the A400M MSN2 is extensive. Because of this, a selection of noteworthy runs should be considered to be analysed solely. As a matter of fact, there are cases which do not provide any significant insight to the problem and they are, thus, discarded from the study. The preliminary steps (i.e. runway preparation) towards the initialization of the numerical simulation are time-consuming. Therefore, a simplification of the number of tasks required to perform prior to any simulation is considerably diminished by reducing the set of cases to analyse.

The activation of the nose landing gear shock absorber high pressure chamber, constant brakes application pattern, ground idle or reverse thrust regimes, constant and low values for roll and pitch angle and the avoidance of taxiing over previous ruts constitute the basic criteria followed to select the relevant taxi cases out of the total compendium of runs performed during the campaign. It should be noted that runs under reverse thrust regimes are found to be critical, since higher loads are found on the lading gear due to the aircraft apparent weight increment followed by wing lift suppression.

Furthermore, the numerical simulation is performed along a remarkable time-window. Said time span is predefined when analysing the already selected runs. The time-windows include relevant phenomena worth to reproduce in later simulations: the activation of the nose landing gear shock absorber high pressure chamber or the appearance of high loads on the landing gear, for instance.

Should the time-windows contain representative features encountered in taxi operations to enhance the understanding and analysis of the phenomena depicted. As an added perk, when evaluating the whole taxi run time span, it appears that the initial instants of time may not be relevant from the taxi point of view, since they usually represent the landing phase itself. Thus, said instants of time are discarded from the analysis as the aircraft is still aloft, the landing gear is not overcoming any load coming from taxi operation, and the brakes are not applied as well.

Oppositely, the last actions found during the taxi runs correspond to those where the aircraft comes to a halt. The braking system may not be active during these final recorded instants of time, and the loads encountered might not be critical.

Bearing the aforementioned criteria in mind, the number of cases which are selected to perform a numerical simulation afterwards, and to compare the experimental response with that retrieved numerically corresponds to three taxi runs pursued after landing.

In the table below, a summary of the shortlisted cases to simulate is enclosed, along with the main features the selected runs present.

Operation	Engine Regime	Brakes	Speed	Weight [T]	X_{CG}
Landing A	Ground Idle	Yes	Medium	105	Forward
Landing B	Reverse/ Ground Idle	Yes	Medium	106	Rearward
Landing C	Reverse/ Ground Idle	Yes	Medium	115	Forward

Table 4.1 Selected taxi runs to simulate

The taxi runs presented in Table 4.1 are originated from landings at Écury sur Coole airfield. These are performed at ground idle or reverse thrust regime, constant braking action in the vast majority, different mass states and centre of gravity configurations. It should be noted that a medium taxi speed is defined within a range around 50 to 75 knots.

The subsequent sections introduce the comparison between the experimental data gathered during these three taxi runs at a specific time-window with the results yielded after performing numerical simulations. A set of modifications is included throughout the numerical simulation process with the purpose of matching the experimental response with the numerical one. To do that, a combination of entering parameters is tuned to achieve said objective.

4.2 First simulation results

In this first set of attempts to match the simulated response to the experimental one, the taxi runs are simulated at constant velocity using the runway profile as it is. The shock absorber initial gas pressure P_0 to each leg is modified according to the experimental values the aircraft presented aloft, with the landing gear extended, prior to landing. The external forces at the aircraft centre of gravity Fy_{CG} and My_{CG} are introduced as constant values. Moreover, no rolling moment at the centre of gravity Mx_{CG} is accounted for and the same braking coefficient is considered to all main landing gear legs.

To facilitate the analysis, a reference time instant is defined at the maximum peak value the vertical force at the nose landing gear reaches during taxi operation. First stages include the matching of the experimental response with the numerical one at that precise reference time instant.

Many aircraft components' experimental response has been paired with the corresponding aircraft components' response yielded numerically. Nonetheless, the characteristic sizing cases found in taxi operations correspond to wing down bending moment, the vertical forces acting on the forward fuselage and the loads exerted on the landing gear. Through subsections 4.2.1 *Landing A*, 4.2.2 *Landing B* and 4.2.3 *Landing C*, the comparison between the responses obtained experimentally and numerically is presented for the aircraft wing root, HTP root and nose landing gear.

4.2.1 Landing A

The shear force (Fz) and bending moment (Mx) at the wing root, as well as the shear force and bending moment at the HTP root are depicted in the following figures[1].

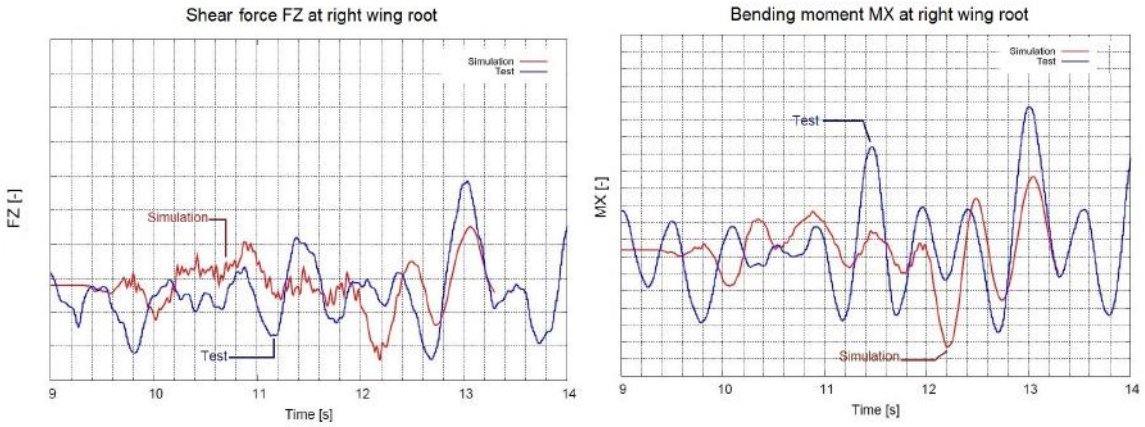

(a) Wing root shear force

(b) Wing root bending moment

Figure 4.1 Wing root magnitudes, Landing A

As it can be appreciated in Figure 4.1, the graphical comparison between the response yielded after performing a numerical simulation (red) and the experimental one (blue) is depicted for the shear force and bending moment acting at the wing root.

It is remarkable to say that the resulting loads retrieved from the numerical simulation, acting on the aircraft structure itself (including wings, HTP, VTP, fuselage), are incremental loads. Thus, should the respective 1G load be added to the latter with the purpose of comparing total loads.

[1] All values concerning forces, moments, pressure and stroke readings are given in non-dimensional form. A reference force, moment, pressure and stroke value is used respectively for this purpose.
The time scale is defined in a way it depicts the time passed after landing.

The magnitude the shear force and bending moment the numerical data present lies within the appropriate level if compared to the experimental values retrieved during the tests.

The ensuing step is related to the fact of matching the frequency and amplitude the experimental data presents. As it is perceived in Figure 4.1a, the computed response shows a match in frequency from 10.3 to 11.2 seconds and approximately matched from 12.5 to 13.2 seconds. The numerical response is either delayed or it does not display a representative pattern to enhance matching in the remaining time periods. Specifically, the zones which are coupled in terms of frequency do not present the amplitude enough to reach the peaks and valleys the experimental response shows.

Figure 4.1b exposes an approximate matching in frequency from 11.8 to 13.3 seconds. The remaining response appears to be out of phase. Experimental peaks and valleys are not accurately modelled since the numerical simulation data show a low amplitude response at certain characteristic peaks (11.5s and 13 seconds) and single valley (12.7s). On the other hand, the valley at 12.2 seconds and the peak at 12.4 seconds are outsized.

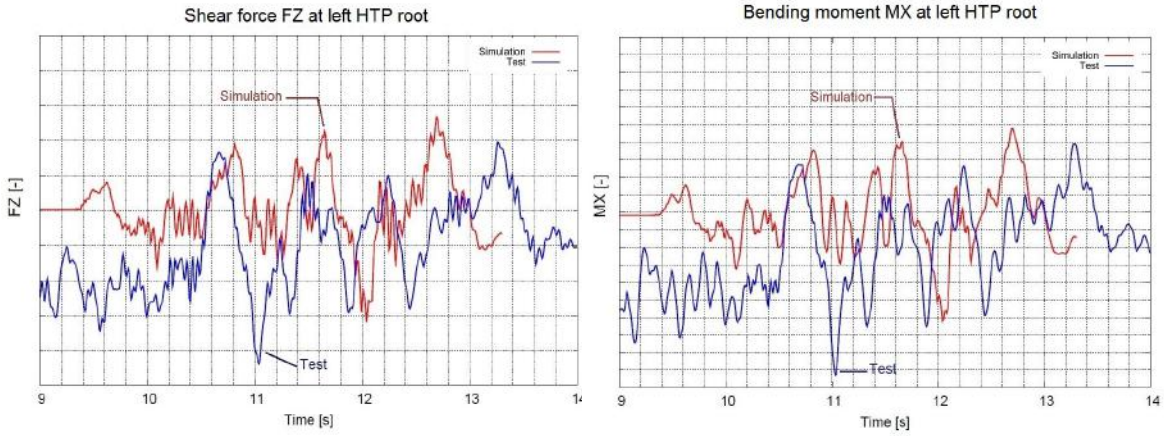

(a) HTP root shear force

(b) HTP root bending moment

Figure 4.2 HTP root magnitudes, Landing A

On the contrary, the loads resulting from the numerical simulation acting at the HTP root are unlevelled at initial instants of time. The numerical response given by the shear force and bending moment comes into view to be delayed. Moreover, the required amplitude to reach data extremes is insufficient, as well.

The variation of the vertical force acting on the nose landing gear is depicted in Figure 4.3. Note that loads acting on the landing gear do not require the addition of 1G loads. Both, numerical and experimental data, lie within a similar magnitude level. However, the

frequency and amplitude the numerical results exhibit differ from those obtained through the taxi runs. Notice that the shape of the response itself is dissimilar comparing both sources of data.

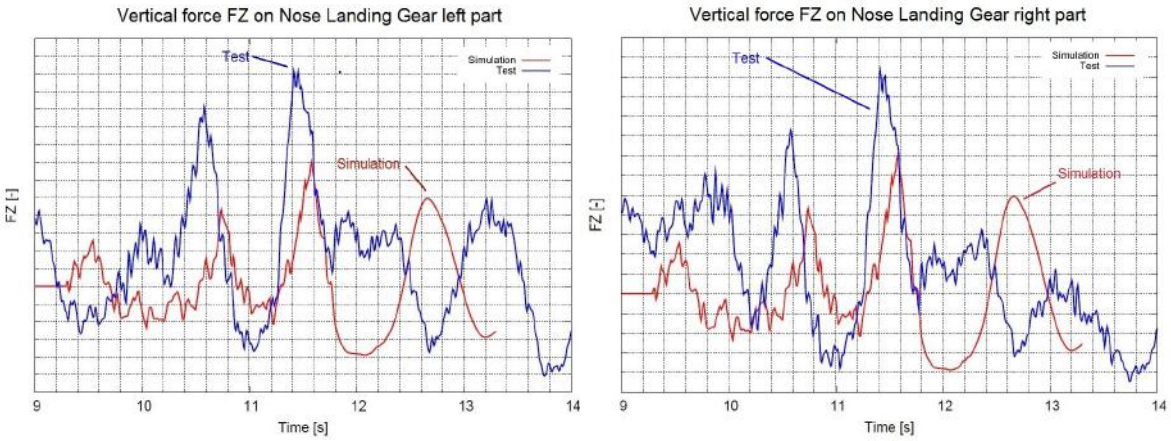

(a) Vertical force left part

(b) Vertical force right part

Figure 4.3 Vertical force on nose landing gear, Landing A

4.2.2 Landing B

The comparison between the experimental response and the numerical one for the second shortlisted taxi run is attached in the current subsection by providing the variation in time of a selected list of magnitudes.

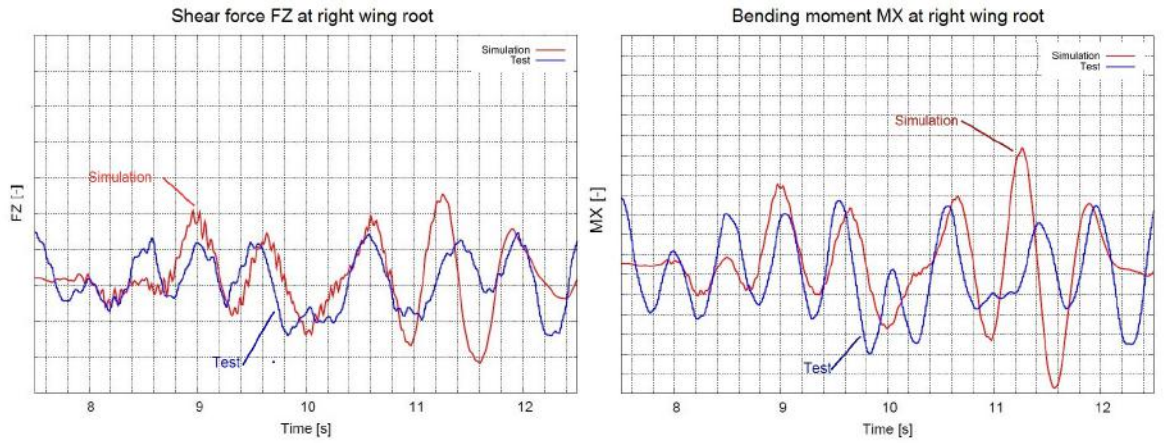

(a) Wing root shear force

(b) Wing root bending moment

Figure 4.4 Wing root magnitudes, Landing B

Figure 4.4 illustrates the graphical comparison between the shear force and bending moment acting at the wing root obtained numerically with the experimental response retrieved during the taxi tests. As it can be appreciated, both responses are levelled in terms of magnitude. The numerical response itself tends to be paired with the experimental one from 8.6 to 11 seconds in the case of shear force loads, whereas from 8.6 to 9.8 seconds in the wing root bending moment case. At those selected instants of time, the amplitude and frequency can be said to lie within established and appropriate limits, although some further tuning is needed to capture the valley values in a more accurate way (Figure 4.4b, specially).

On the contrary, the response the numerical simulation provides in the final section of the time span is utterly different from what the aircraft wing root did experiment during the tests.

Figure 4.5 portrays the evolution in time of the shear force and bending moment acting at the HTP root. Numerical and experimental responses are plotted altogether. Recurrently, the responses are levelled in terms of magnitude. Besides, the numerical response is considerably delayed from the experimental one. The responses are entirely unmatched.

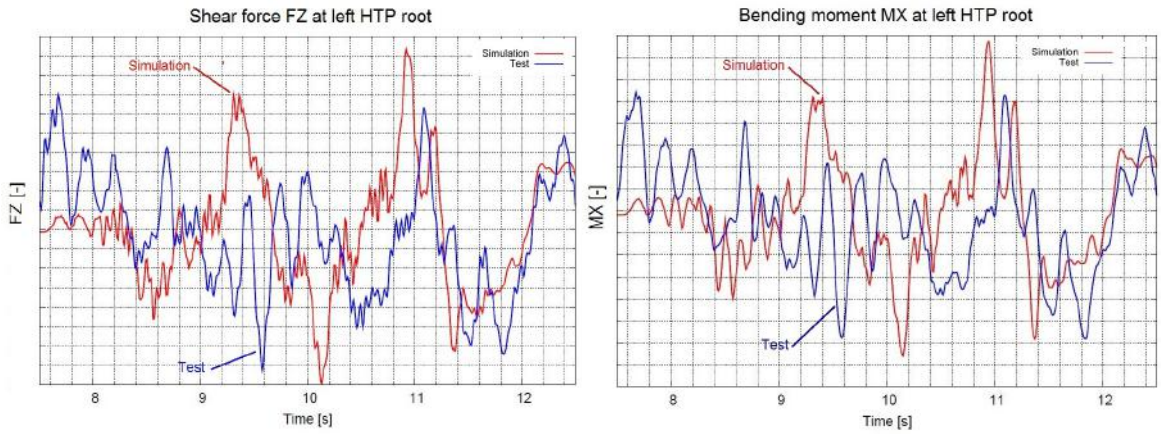

(a) HTP root shear force

(b) HTP root bending moment

Figure 4.5 HTP root magnitudes, Landing B

In Figure 4.6, the numerically computed vertical force exerted on the nose landing gear is depicted along the experimental response obtained at the taxi run followed by Landing B.

A good match between the numerical and experimental response is obtained from 10.3 to 11.4 seconds. Both frequency and amplitude requirements are fulfilled. Oppositely, the peak found from second 11.4 onwards is outsized: the value found at the valley is reproduced by the numerical simulation, whilst the numerically calculated peak value lies below the

experimental vertical force peak value the nose landing gear experienced at that precise instant of time.

Furthermore, the response gathered after performing a numerical simulation from 7.5 to 10.3 seconds depicts a completely distinct behaviour from what the nose landing gear is overcoming during the test.

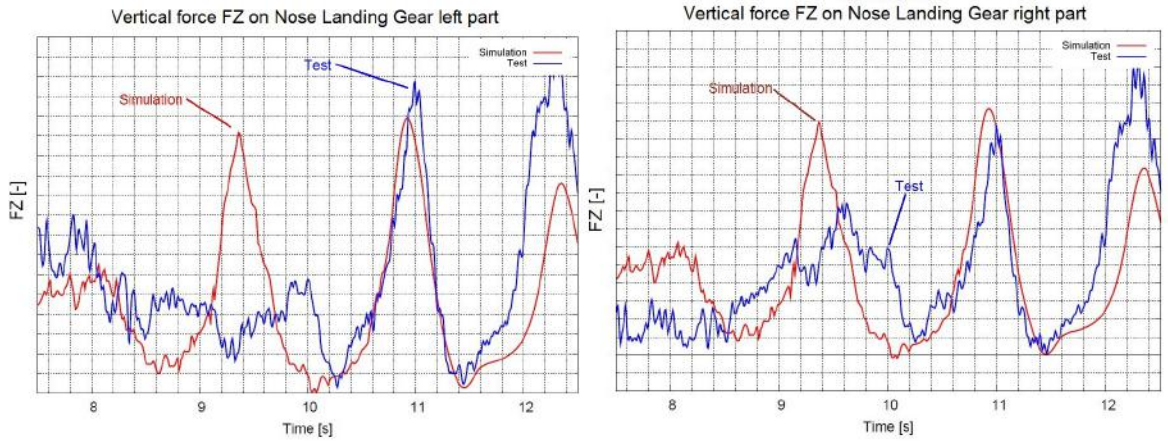

(a) Vertical force left part

(b) Vertical force right part

Figure 4.6 Vertical force on nose landing gear, Landing B

4.2.3 Landing C

The similarity between the numerical response and the experimental one yielded after Landing C is analysed through this subsection. The wing root and HTP root shear force and bending moment along with the vertical force acting on the nose landing gear are the parameters used for this purpose.

The numerically obtained shear force acting at the wing root attempts to reproduce the experimental pattern resulted from the taxi trials during a time period spanning from 11 to 11.7 seconds. The rest of the response lacks enough amplitude to be coupled with the experimental one. Moreover, the resulting numerical pattern does not emulate what is occurring at the aircraft wing root during taxi operation. The latter is graphically depicted in Figure 4.7.

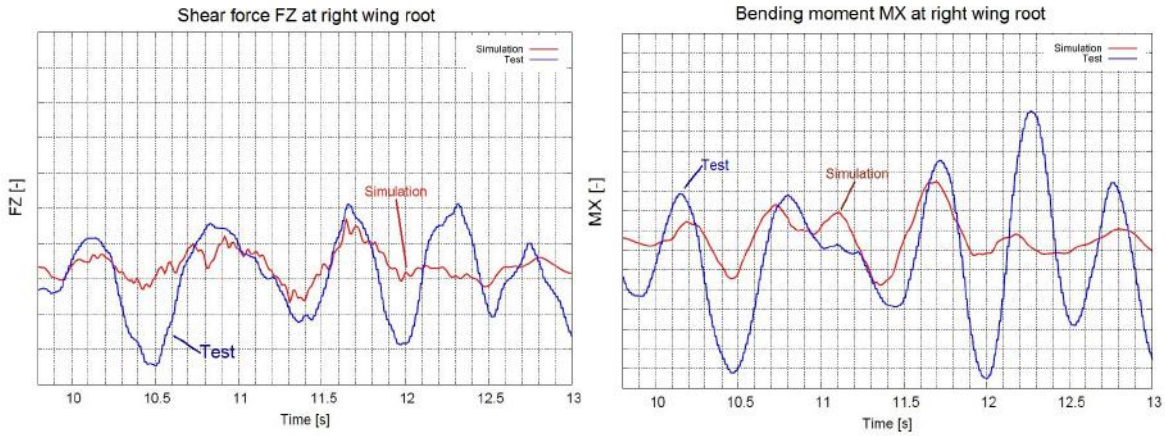

(a) Wing root shear force

(b) Wing root bending moment

Figure 4.7 Wing root magnitudes, Landing C

On the other hand, three conclusions can be drawn after analysing Figure 4.8:

- Numerical response presents distinct shape to experimental one
- Numerical response is delayed with respect to experimental one
- Numerical response presents low amplitude

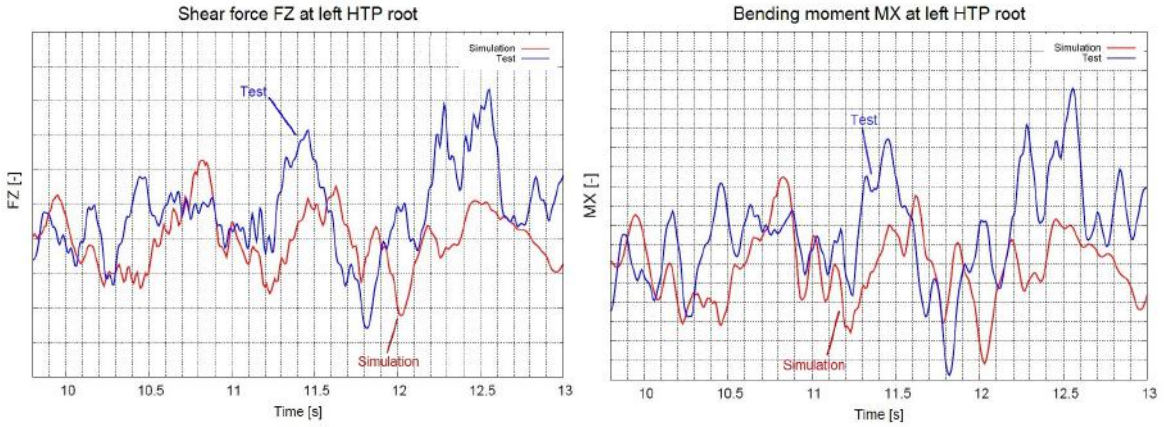

(a) HTP root shear force

(b) HTP root bending moment

Figure 4.8 HTP root magnitudes, Landing C

From 9.8 to 11.25 seconds, the numerically computed response is different from what the aircraft HTP root experiences during the taxi run. Furthermore, from 11.25 to 12.2 seconds the numerical response attempts to model the experimental response but it appears to be

either delayed or out of phase. From 12.2 seconds onwards, the numerical response is indeed similar in shape to the experimental one. Nevertheless, the resulting numerical response amplitude is lower than the required one to mimic the experimental response in an accurate manner.

It can be denoted by analysing Figure 4.9 that the peaks and valleys referred to the vertical loads acting on the nose landing gear are not precisely reproduced by the numerical simulation. The numerical response is delayed with respect to the experimental one and the amplitude is not the appropriate one to reach extreme values.

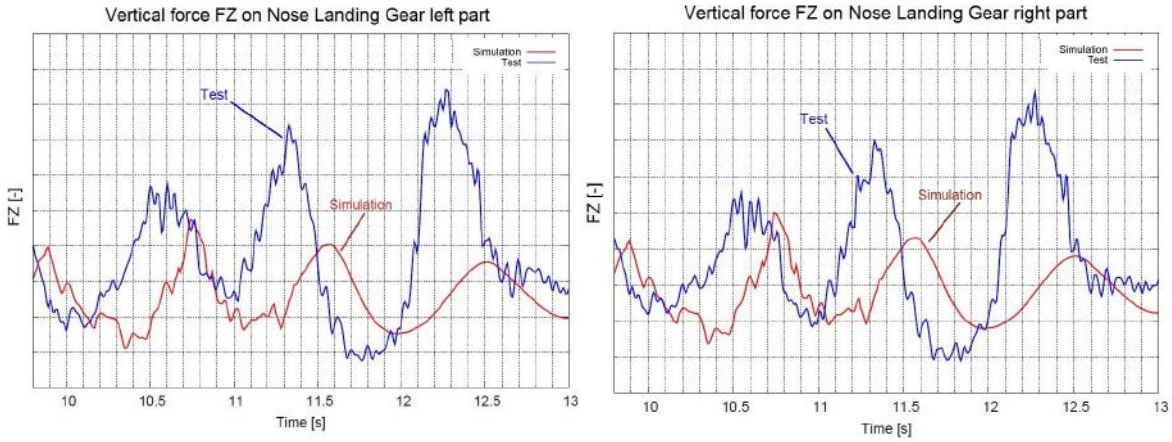

(a) Vertical force left part

(b) Vertical force right part

Figure 4.9 Vertical force on nose landing gear, Landing C

4.2.4 First stage concluding remarks

The features to tune in future numerical simulations are related to the delay both numerical and experimental responses display, the response amplitude to reach extreme values and the shape of the response itself (including frequency matching).

Further improvements can be done regarding the approach of adding experimental data as input parameters. Indeed, further modifications are praised to be introduced since the numerical and experimental response differ considerably. To do that, the addition of the total rolling moment at the aircraft centre of gravity is considered for future runs. The inclusion of said asymmetry may contribute to reshaping the numerical response. So far, the problem is analysed as if it were symmetric. Truth is that the taxi problem is not strictly symmetric since antisymmetric aileron deflections are deployed during test trials. It should be pointed out as well that the lateral runway inclination (lateral slope) plays a role in the level of asymmetry

found by inducing a determined bank angle. As a result, the addition of a mean constant rolling moment value into the simulation process will provide an extra degree of realism to the problem.

Far from that, the vertical force acting at the aircraft centre of gravity and pitching moment can be inputted as time histories. Since the aircraft angle of attack is not held in a fixed position during the entire run and the elevator deflection angle also changes, these variations may provoke the lift and pitching moment to vary as well. Said variations are accounted for in time histories.

This modification will make the shape of the response improve with respect to the shape gathered when considering constant values of forces and moments. Moreover, the amplitude of the response is expected to be widened since a pair of forces and moments are inputted into the numerical simulation every considered time step. On the other hand, by providing a single pair of force and moment values the real aircraft behaviour is not reproduced in detail, it is assumed that parameters such as the aircraft angle of attack or elevator deflection are kept fixed during the run.

Further improvements to introduce are related to the corresponding braking coefficient each main landing gear leg presents. Brakes are not uniformly applied. Besides, the autobraking system may not act on equal terms at each leg. Thus, different braking coefficients may be found at each main landing gear leg. It might be even possible to have non-braking legs along with braking legs at the same time. Braking appears to be a heterogeneous phenomenon to reproduce.

By introducing different braking coefficients to each leg, the response amplitude may change. As a consequence, not only the vertical force acting on the nose landing gear may be affected by this modification, interrelated magnitudes such as the shock absorber stroke or the loads acting on the main landing gear might also get influenced by this adjustment.

To adjust the response shape outside the time-window central section, the runway roughness profile can be further smoothed at the connections between the roughness profile itself and the 50m long flat profile. Note that these runway sections are modified with respect to the real runway profile with the purpose of enhancing the analysis. By placing a flat profile, the aircraft response to a given excitation is delimited by the profile itself in a way it is known where the response actually starts, since null response is obtained when taxiing over the initial flat profile.

Needless to say that this modification is indeed out of the original runway roughness profile the aircraft is experimentally taxiing on. It might be the case that the numerical response is not coupled with the experimental one because the time-window, and therefore, the runway profile, is not capturing the entire phenomena the original runway profile presents at those particular points. Hence, the aircraft response is different to the experimental one because the excitation is different too.

In order to palliate this discrepancy, the time-window should be enlarged to grasp the phenomena which were not taken into consideration in the previous time span. This readjustment will improve the numerical response outside the time-window central section.

4.3 Intermediate simulation results

Bearing in mind all the points concluded in the precedent batch of results, new modifications are introduced in the numerical simulation with the aim of upgrading the numerical response. Three major adjustments are incorporated in the present set of simulations:

- Mx_{CG} constant value
- Fz_{CG} and My_{CG} 0.5 second-accuracy time histories
- Different braking coefficient values to each leg

Since asymmetries are introduced in the problem by deploying the ailerons antisymmetrically, a rolling moment acting at the aircraft centre of gravity is therefore induced. The current DYNTAXI capabilities only allow the inclusion of a single rolling moment value. Said value corresponds to the mean rolling moment value found at the selected time window. The rolling moment is approximated by using the following equation:

$$Mx_{CG} = \frac{1}{2}\rho V^2 S(C_{l\delta_a} + C_{l\phi})b \tag{4.1}$$

The rolling moment evolution[2] in a specific time-window is depicted in Figure 4.10.

Apart from aileron deflections, the change in velocity during the selected window also influences the final values the rolling moment acquires. Note that the red point, rolling moment mean value, is solely introduced into the numerical simulation software.

[2]The following plots depicting time histories of forces and moments correspond to Landing A exclusively. These are used as guidance to follow the explanation. Landing B and Landing C present different time histories as the experimental data differs between runs.

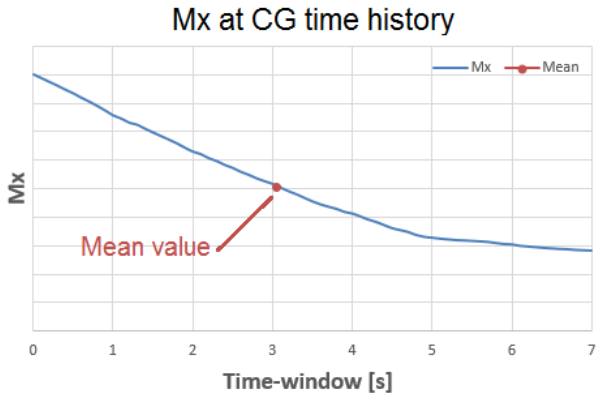

Figure 4.10 Rolling moment evolution

Oppositely, the vertical force and pitching moment acting at the aircraft centre of gravity can be introduced as time histories. To do that, the experimental aircraft angle of attack, elevator deflection, engine thrust and TAS velocity are required to be known at a certain time step. Since the experimental data was recorded at 128Hz, the information above can be extracted each 0.0078125 seconds. To start with, the initial time history of forces and moments is computed each 0.5 seconds along the time-window.

The difference between inputting a single value for Fz_{CG} and My_{CG} or a time history lies on the fact that in the first case the external loads acting on the aircraft are assumed to be constant during the entire run. In reality, the external loads vary since the velocity decreases as the aircraft brakes, as a first resort. Moreover, the angle of attack and elevator deflection angle also fluctuate during the run. The variation of the elevator deflection angle in time, for a given time-window is depicted in Figure 4.11.

The vertical force acting at the aircraft centre of gravity is computed as follows:

$$Fz_{CG} = L - W \tag{4.2}$$

The pitching moment at the centre of gravity is approximated by the following expression:

$$My_{CG} = \frac{1}{2}\rho V^2 S C_M MAC + L(x_{CG} - x_{aero}) + D(z_{aero} - z_{CG}) + T(z_{CG} - z_{aero}) \tag{4.3}$$

Note that C_M is given by equation (2.3).

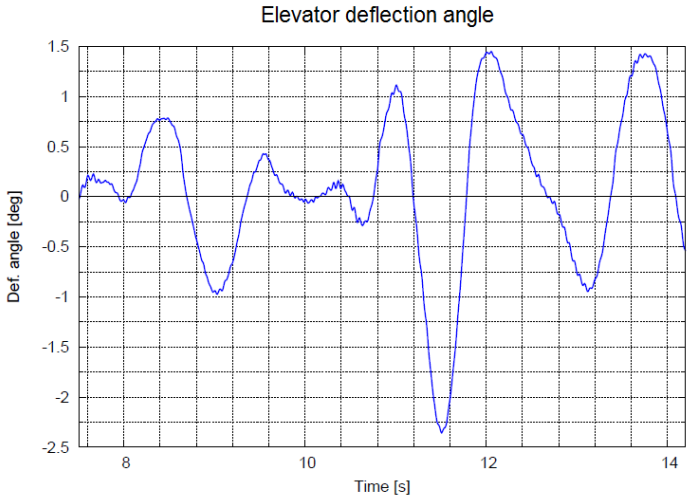

Figure 4.11 Elevator deflection angle evolution

In the enclosed figures, the time histories of vertical force and pitching moment acting at the aircraft centre of gravity are illustrated.

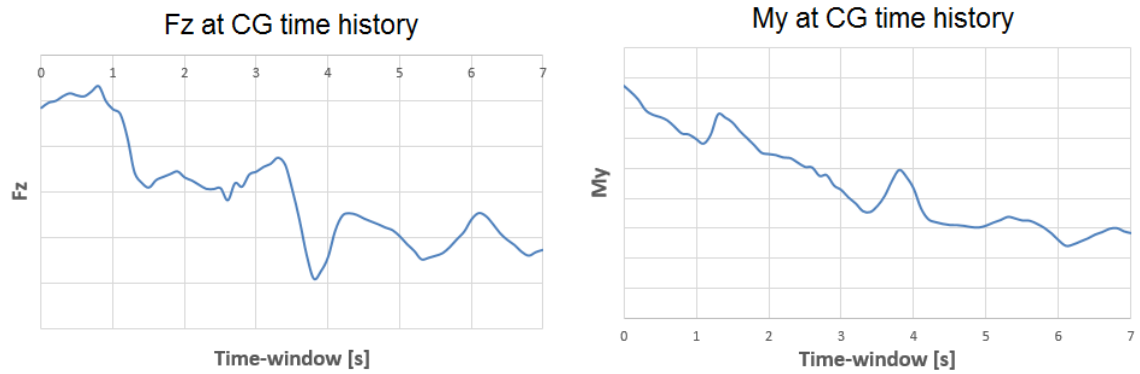

(a) Fz_{CG} time history

(b) My_{CG} time history

Figure 4.12 Fz_{CG} and My_{CG} time histories

The last adjustment is produced by introducing different braking coefficients to each main landing gear leg. The current software capabilities permit to input a single constant value to each leg. Time histories of braking coefficients are not admitted. Furthermore, the time-window was enlarged (to the left side) to capture the runway phenomena accurately, so that the numerical and experimental responses match.

In ensuing subsections, the effectiveness of the preceding ameliorations is checked. The shear force and bending moment at the wing and HTP root along with the nose landing

gear gas pressure are the magnitudes utilised to compare the numerical response with the experimental one. Note that the nose landing gear gas pressure response is similar to the vertical force acting on the nose landing gear itself. Therefore, both magnitudes can be interchangeably used to analyse the nose landing gear response.

In subsections 4.3.1 *Landing A*, 4.3.2 *Landing B* and 4.3.3 *Landing C*, the adjustments described through this section are taken into consideration. Likewise, the initial gas pressure P_0 each landing gear shock absorber presents is also modified with respect to a reference value. Again, the pressure reading each shock absorber displayed aloft, before landing, with the landing gear extended, was inputted into the numerical simulation process.

4.3.1 Landing A

In Figure 4.13, the comparison between the numerical and experimental response the shear force and bending moment at the wing root yield is illustrated.

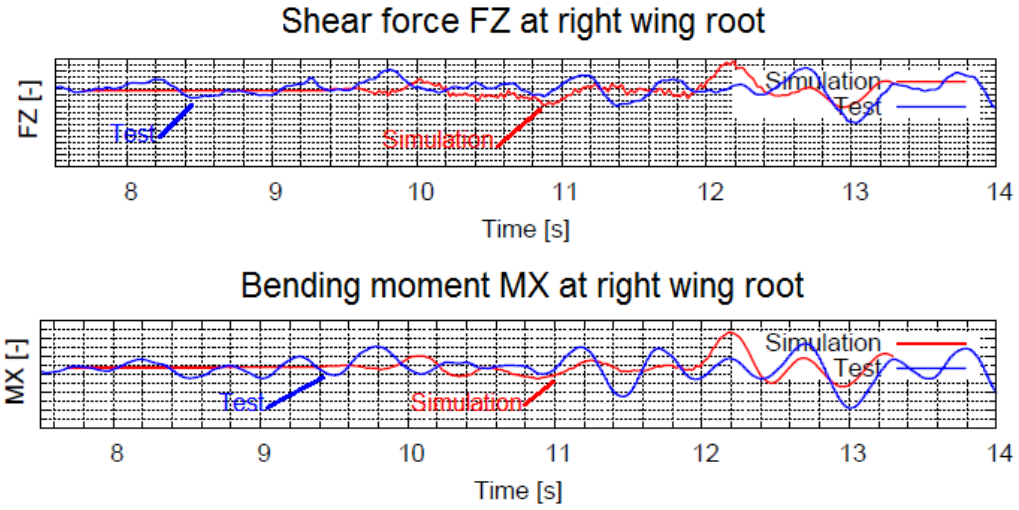

Figure 4.13 Wing root magnitudes, Landing A

It can be appreciated that both responses are levelled in terms of magnitude. On the other hand, the bending moment numerical response is out of phase with respect to the experimental one from 9.5 to 12 seconds. Particularly, the shear force numerical response seems to be damped at that particular time period, if likened to what the wing root is indeed experiencing. The shape and frequency of the numerical response attempt to match the experimental ones from second 12.5 onwards in both cases.

The major improvement gained from the first results gathered is related to the numerical response amplitude. Although these results need further tuning, it can be said that the peak and valley values the numerical response provides are closer to those the experimental response exhibits.

Figure 4.14 depicts the comparison between the numerical and experimental response retrieved at the HTP root.

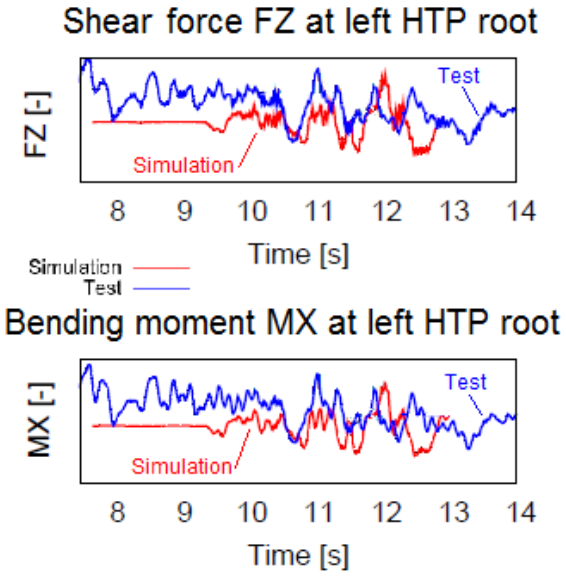

Figure 4.14 HTP root magnitudes, Landing A

The initial response up to second 10.5 looks to be unmatched since both responses are initialised at distinct magnitude level. Besides, both responses tend to be matched from 10.5 to 12 seconds. A major improvement is obtained with respect to the first results. The numerical signal amplitude is enhanced as well. Nonetheless, both responses differ at the final time section.

The numerical response of the nose landing gear low pressure chamber gas pressure differs from the experimental one up to second 10 and beyond second 12. The time delay between both responses is appreciated as well. The unique change comes from the ability to reach higher values. Thus, the response amplitude is increased in a way upper limit values are closer to be reached.

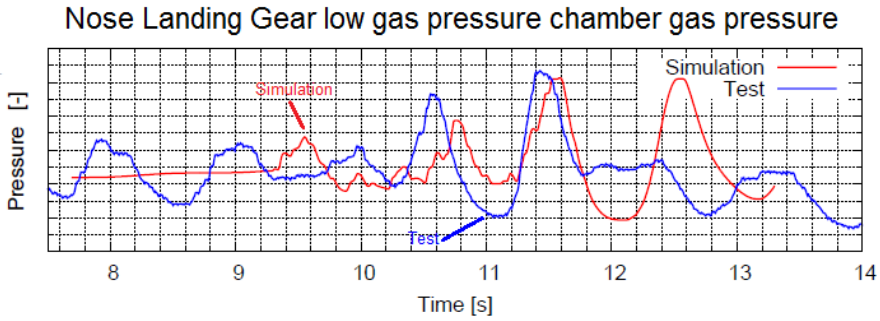

Figure 4.15 Nose landing gear gas pressure, Landing A

4.3.2 Landing B

Figure 4.16 depicts the graphical comparison between the numerical and experimental shear force and bending moment the second shortlisted case provides.

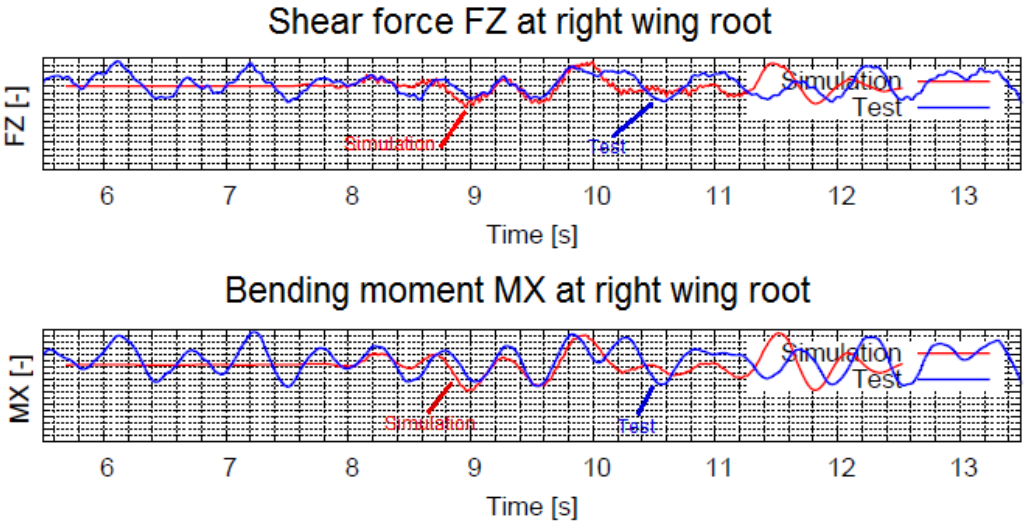

Figure 4.16 Wing root magnitudes, Landing B

A considerable improvement is found with respect to the initial results. The numerical response shape and frequency are extremely similar to those parameters characterising the experimental response in the time span comprising from 8.5 to 10.1 seconds. Indeed, not only the responses are levelled, there are peaks and valleys perfectly modelled (shear force). Hence, it can be stated that an increment in the numerical response amplitude is yielded.

On the other hand, further refinement is required from second 10.1 onwards since the response is found to be either delayed or it is different from what the wing root is experiencing.

Figure 4.17 displays the variation in time of the numerical and experimental responses the HTP root undertakes. In this case, the numerical response is not improved with respect to the initial one. The signal is still delayed from the experimental one. Further adjustments are required.

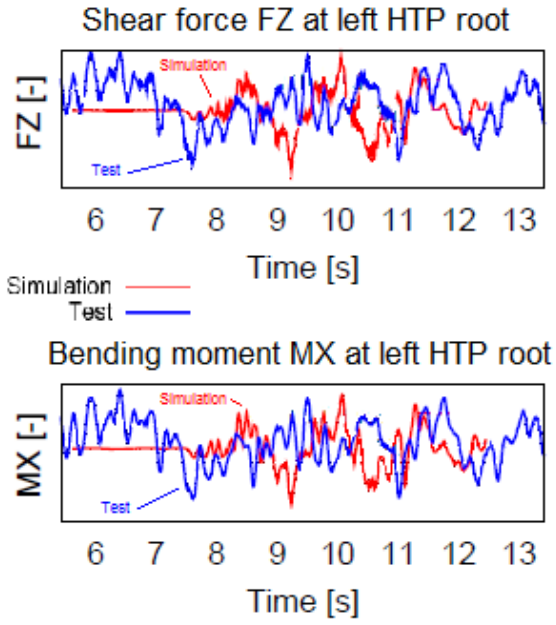

Figure 4.17 HTP root magnitudes, Landing B

The time history of the nose landing gear gas pressure is depicted in Figure 4.18. These numerical results constitute a worse version of the first ones presented (regrading the vertical force acting on the nose landing gear). The response is not only delayed towards the side the runway and time-window were extended, but a different and shrunk pattern was retrieved at the end of the time-window, as well. Both responses are not levelled.

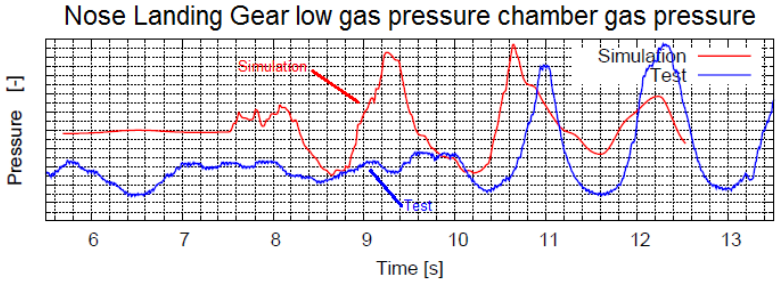

Figure 4.18 Nose landing gear gas pressure, Landing B

4.3.3 Landing C

The comparison between the numerical and experimental response of the magnitudes selected for Landing C is included in the present subsection.

The shear force and bending moment evolution in time is depicted in the following figure.

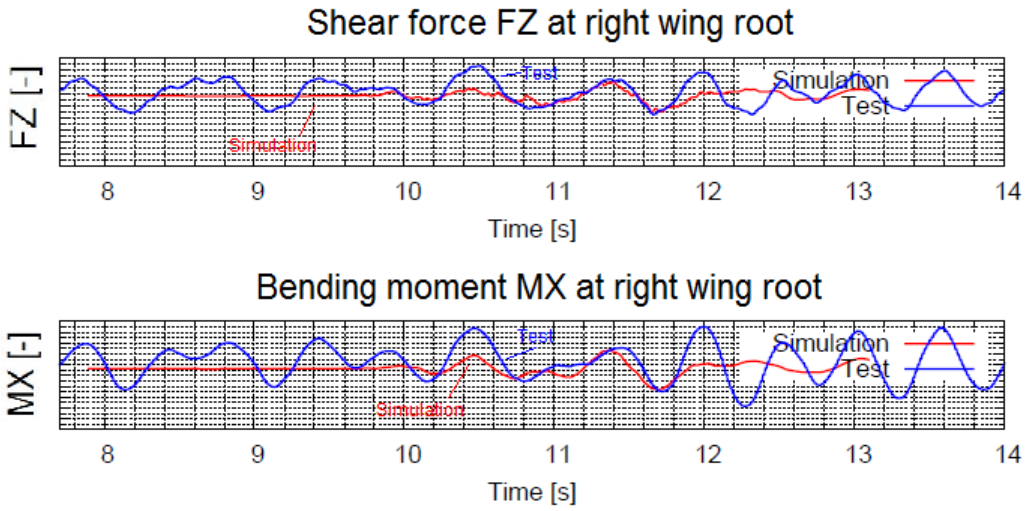

Figure 4.19 Wing root magnitudes, Landing C

A slight improvement is found with respect to the first batch of results obtained. An accurate match between responses results in the central section of the time-window. In other words, the experimental response is modelled by the numerical one in that precise section. However, it can be appreciated that the numerical response is damped during the instants of time different from those highlighted previously.

The responses retrieved at the HTP root are illustrated in Figure 4.20. A general amelioration is gathered since the numerical response is adjusted in shape and frequency to the experimental one. It is remarkable to point out that the precedent set of results for Landing C showed a discrepancy between the magnitude level the numerical response displayed compared to that associated with the experimental results. The numerical response lied below the experimental response.

Currently, the numerical response is indeed equally positioned or marginally above the experimental one. It can be concluded that the numerical response amplitude has grown with respect to precedent results.

Finally, the nose landing gear gas pressure is depicted in the time domain in Figure 4.21.

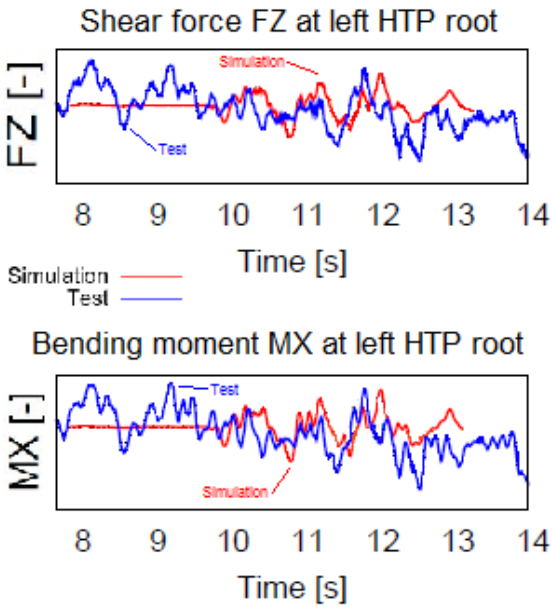

Figure 4.20 HTP root magnitudes, Landing C

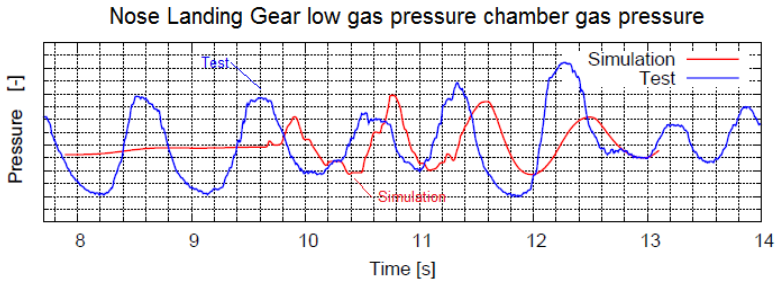

Figure 4.21 Nose landing gear gas pressure, Landing C

The unique distinction with respect to precedent Landing C results which is worth mentioning is related to the numerical response amplitude increment. Higher values are achieved, although peak and valley values are still unreachable. Contradictorily, the numerical response shape is maintained equally as well as the time delay depicted.

4.3.4 Intermediate stage concluding remarks

The addition of the preceding adjustments is not enough to match the numerical and experimental responses. As it was demonstrated in previous subsections, the overall numerical response amplitude was considerably improved. On the contrary, the response shape was still not perfectly fitted to the experimental one, and time delays were unfixed as well.

A notorious phenomenon yet found in the second batch of measurements is related to the time delay encountered in certain magnitudes described. It is distinguished that the time delay the nose landing gear magnitudes displayed is different to that found in other aircraft components (HTP, wings, for instance).

Landing B wing root magnitudes present coupled responses at a specific time portion. Nonetheless, the responses at the HTP root or nose landing gear are either out of phase or delayed at that precise time span.

In Landing A and C, the numerical response is slightly paired (for a given time period) with the experimental one in the wing root and HTP root magnitudes. Oppositely, at the specific time span where those aircraft magnitudes are coupled, the numerical response gathered at the nose landing gear is shifted so that a match is not possible to be found.

This incongruous time shift might not be fixed with the addition of a force and moment time history, a rolling moment, a modified P_0 or different braking coefficients to each leg, solely.

As a matter of fact, the addition of time histories for Fz_{CG} and My_{CG} only enhances the improvement of the response shape. The same applies for Mx_{CG}. Inputting different braking coefficients to each leg gives rise to an upgrade in the response amplitude. P_0 modifies the initial level the landing gear magnitudes present.

To cope with the time delay issue, further adjustments are required to be performed. To start with, the time-window and hence, runway profile, should be extended not only leftwards. It is found that, indeed, the numerical response does change since real phenomena are captured within the new enlarged time span. Nevertheless, the time-window should be widened towards both extremes to catch all the underlying occurrences left aside.

The second modification has to do with the runway adaptation so that the decrease in velocity induced by the braking action is included in the simulation somehow.

Although the taxi run is simulated at constant taxi speed, experimentally, the velocity diminishes at the same rate the brakes are applied. Therefore, the velocity reduction found within a specific time-window is noticeable and it cannot be neglected. In order to incorporate such variation without having to modify the numerical software (runs are still computed at constant taxi speed), the easiest manner is to integrate said variation within the runway roughness profile.

4.4 Final simulation results

Four major adjustments are introduced to reach final results:

- Runway profile adaptation
- Shock absorber curve fitting
- Further braking coefficient values re-adaptation to each leg
- Fz_{CG} and My_{CG} 0.1 second-accuracy time histories

The first adjustment which is taken into consideration through this new batch of simulations is the runway profile adaptation, so that the velocity variation along a specific time-window is included in the numerical solution. The objective of this arrangement is to get rid of the overall time delay presented between the numerical and experimental response.

The aircraft experienced a deceleration during taxi runs whenever brakes were applied. Thus, the aircraft underwent a decrease in velocity during the run contrary to what is indeed introduced in the numerical simulation process. Recall that taxi runs are simulated at constant speed during the whole time-window.

In order to compute a new runway profile suitable for this purpose, a reference instant of time is required. Recall that said reference instant of time corresponds to the time point within a determined time-window where the maximum force peak value was reached at the nose landing gear. Moreover, a reference velocity and reference runway position with respect to the runway origin are also defined at that precise time instant.

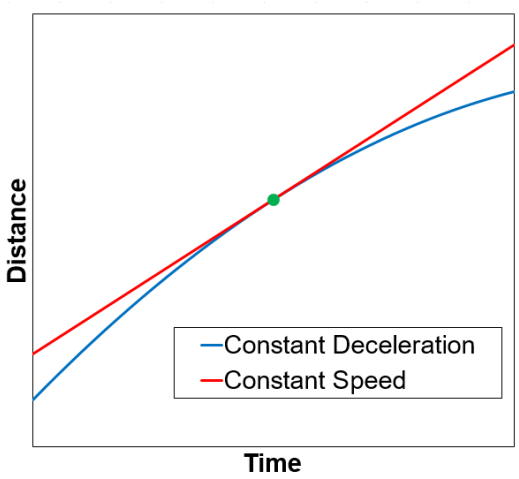

Figure 4.22 Runway roughness profile adaptation

Once the duly reference magnitudes are defined, the regenerated runway is computed mathematically as follows:

$$X_i' = X_R + V_R(t_i - t_R) \tag{4.4}$$

X_R denotes the reference runway position, V_R represents the reference velocity and t_R is the reference instant of time. Note that V_R is inputted into the numerical simulation as the constant velocity at which the aircraft runs during the test.

The formula above implies that for a given time instant t_i, the runway position with respect to the runway origin at that precise instant X_i' is equal to the runway position which would yield at the reference instant of time, plus the runway position offset which would be covered when introducing a change in velocity in a given time differential. For a given instant of time, each X_i' position has a corresponding Z runway coordinate, denoting the roughness profile itself (runway height variation). Note that this process should be repeated for each leg.

Additionally, the time-window is enlarged sideways to capture all the phenomena left behind with the purpose of getting realistic responses outside the window central section. To widen the time-window leftwards was not sufficient to improve the response shape outcome.

The second major modification which is required to be encompassed in the numerical simulation has to do with the magnitudes defining the shock absorber initial characteristics. So far, the single parameter which was adapted to match experimental results is P_0, the initial shock absorber gas pressure. However, when comparing the numerical and experimental responses the landing gear elements provide, it was detected that both responses were not only delayed but also unlevelled.

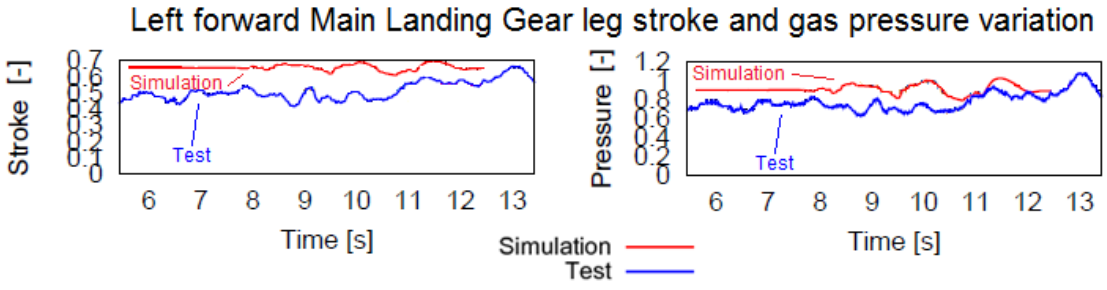

Figure 4.23 Shock absorber parameters

The variation in time of the experimental and numerical shock absorber stroke and gas pressure readings is presented in Figure 4.23. For sake of brevity, the magnitudes depicted

are referred to the left forward main landing gear leg. Similar behaviour is encountered in the remaining landing gear legs.

As it can be appreciated in the figure above, both, shock absorber stroke and gas pressure numerical and experimental responses are vertically separated (unlevelled) by a given offset. Besides, the responses seem to be unmatched as well. The challenge which is required to be overcome is related to getting rid of the offset which makes the responses be misaligned.

The previous magnitudes interrelation is depicted in the following figure. Note that it is again referred to the left forward main landing gear leg.

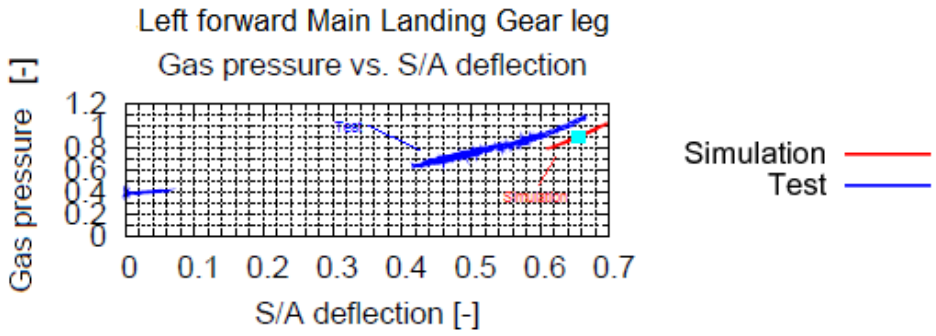

Figure 4.24 Shock absorber curve, single stage

The variation of the shock absorber gas pressure along with the shock absorber deflection (stroke) exemplifies the path followed by the shock absorber during operation. The light blue dot represents the 1G, static condition given by a pair of stroke and pressure readings.

Again, the numerical curve is shifted rightwards. New readjustments are required to be brought into action so that the separation between both curves (experimental and numerical) is minimum.

Note that the main landing gear shock absorbers are single-chambered. The phenomena illustrated above can also be found in double-chambered shock absorbers. Figure 4.25 depicts the nose landing gear shock absorber pressure to stroke variation. Two stages are represented. The second stage is encountered whenever the gas pressure exceeds a determined threshold (portrayed by the straight horizontal line in Figure 4.25).

In the same manner, it can be appreciated that the numerical curve is shifted with respect to the experimental one. By modifying a set of parameters which define the shock absorber curve, not only the experimental and numerical curves are likely to be matched, but also

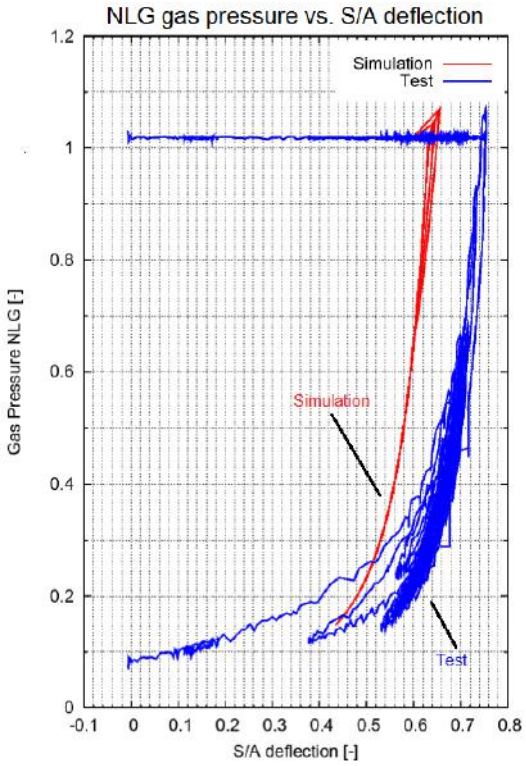

Figure 4.25 Shock absorber curve, double stage

the underlying numerical gas pressure and stroke responses in time could be paired with the respective experimental responses.

Recall that the shock absorber curve itself was mathematically modelled by equation (2.1). So far, the initial gas pressure P_0 is the only parameter which was modified to tune responses. Notice that this variable helps the shock absorber curve be positioned in a determined Y axis value, without altering the curve's shape.

The variables which come in handy to shift and reshape the numerical curve correspond to the initial shock absorber oil volume V_l and gas volume V_0.

The A400M shock absorber system is composed of a low pressure chamber (plus high pressure chamber, if any), oil chamber and piston assembly. The gas and oil volume can vary during operation as long as the total volume (V_0 plus V_l) is held constant (the shock absorber container has fixed and finite dimensions).

Particularly, throughout the campaign, the initial gas and oil volume readings were found to be different from the reference values established by the manufacturer. As a matter of fact, the initial gas volume value referred to the nose landing gear was higher than the reference

gas volume value itself. The opposite behaviour was identified in every main landing gear shock absorber. Moreover, it was discovered that the oil volume was decreasing along the campaign due to oil leakages. A gas volume increment by adding gas to the pertaining shock absorber chambers was an effective measure to counteract oil volume dropping.

In order to reproduce with higher accuracy what the shock absorber is undergoing during operation, the experimental values of V_0 and V_l encountered during runs, different from the reference values introduced in previous simulation batches, are required to be inputted into the numerical simulation.

Since one of the objectives is to match the numerical and experimental curves and the primarily related magnitudes, the required V_0 and V_l values to be introduced to the numerical simulation process are determined by tuning the numerical shock absorber curve -through equation (2.1)- beforehand, so that it is coupled with the experimental one.

It is important to highlight the fact that these magnitudes variation with respect to established reference values is performed in a controlled manner. The manufacturer did already determine that a deviation of $\pm 5\%$ can be expected regarding V_0 and V_l. Values beyond this limit are considered to be unrealistic from the landing gear model validity point of view.

The third major improvement can be achieved by re-adapting each main landing gear leg braking coefficient in a meticulous manner.

It was concluded that the inclusion of distinct and realistic braking coefficients to each leg was fundamental to widen the numerical response amplitude, so that peak and valley values are reached. Recall that the experimental braking coefficient time history is retrieved after dividing the wheel axle horizontal to vertical force time history for each leg.

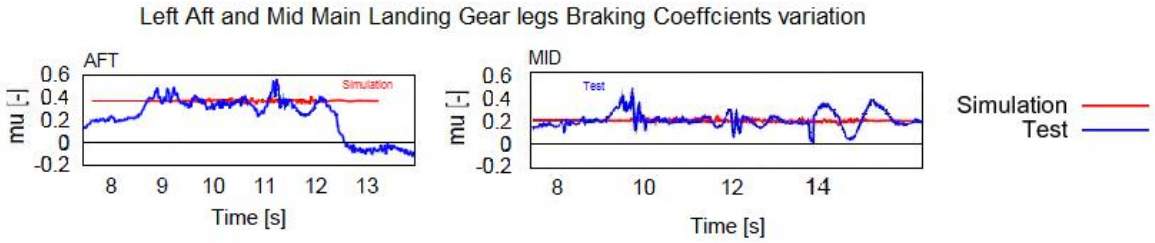

Figure 4.26 Braking coefficients: Landing A example (left), Landing C example (right)

As it can be appreciated in Figure 4.26, two distinct braking coefficient patterns can be found throughout the problem. The first one is found in Landing A left aft main landing gear leg where two braking conditions are represented: from 7.5 to 12.7 seconds the aircraft is braking,

whilst from 12.7 seconds onwards the aircraft is no longer braking as the braking coefficient is not positive-valued. On the other hand, a single braking condition is encountered in the example provided by Landing C left mid main landing gear leg.

So far, the braking coefficient introduced into the numerical simulation is the mean braking coefficient value found whenever brakes are applied along the selected time-window.

Nonetheless, it is perceived that the experimental braking coefficient values oscillate about a mean value. The maximum values are indeed a $\sim 50\%$ higher than the inputted mean braking coefficient values. This would impact significantly on the peak values the numerical responses reached, if said maximum values were introduced into the simulation.

Since there is a wide range of braking coefficient values to choose to be added into the numerical simulation, this new set of simulations uses mean braking coefficient values along with maximum values within a given time-window. A comparison is made between the results gathered through these two different approaches.

The last adjustment which can be encompassed in this new set of simulations is related to Fz_{CG} and My_{CG} time histories. The introduction of time histories of forces and moments instead of constant values is determinant when it comes to adding the transient aircraft behaviour (angle of attack and elevator deflection angle time variation) into the numerical simulation to reproduce the experimental aircraft response in a more accurate manner.

Precedent time histories were calculated with 0.5 second precision. Since transient phenomena exhibit drastic changes within a time span smaller than 0.5 seconds, new time histories are computed by using 0.1 second time step.

The comparison between numerical and experimental wing root and HTP root loads along with the loads acting on the nose landing gear is enclosed in succeeding sections, after including the aforementioned batch of measurements into the simulation process. Results are presented for two braking coefficient overall cases: mean value and maximum allowed value, in each case.

4.4.1 Landing A

The numerical simulation is performed twice so that responses are gathered for the two braking coefficient cases. The same runway roughness profile, Fz_{CG} and My_{CG} time histories and respective gas and liquid volumes to each landing gear leg are utilised for both cases. The unique variation arises from the braking coefficient criteria used: mean value or maximum allowed value.

μ	LFW	LMD	LAF	RFW	RMD	RAF
Low μ	0.29	0.24	0.46	0.39	0.34	0.3
High μ	0.29	0.37	0.55	0.39	0.34	0.45

Table 4.2 Landing A braking coefficients

The numerical and experimental shear force and bending moment at the wing root are depicted in the figure below for low (mean) and high (maximum) braking coefficients.

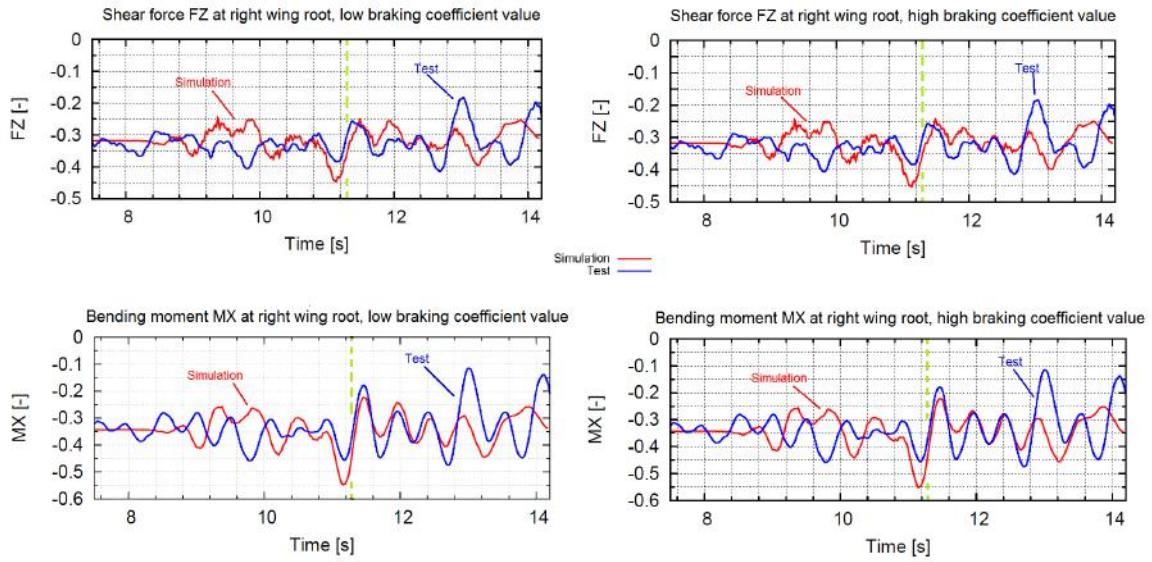

Figure 4.27 Loads at wing root: low μ (left), high μ (right). Landing A

The numerical and experimental responses are matched in terms of frequency and shape from 11 to 13.5 seconds. The responses at the reference time instant $t_R = 11.3s$ (green dashed line) are coupled. Moreover, the numerical response is conservative during said time span since maximum and minimum experimental values lie within the amplitude range registered by the numerical response. On the other hand, it should be noticed that during the initial and

final instants of time, the numerical response does not present the shape the experimental response portrays.

The numerical response shape is exacerbated, if compared to the response gathered in previous simulation batches. The signal amplitude has increased, as well. In the same manner, an amelioration in the responses matching is also achieved.

Lower limits are reached, since shear forces at the wing root are negative-valued, when introducing a higher overall braking coefficient. The numerical response located around t_R for high overall μ presents a slight variation with respect to the response found for lower overall μ: lower values are reached.

The numerical and experimental shear force and bending moment response at the HTP root is illustrated in Figure 4.28.

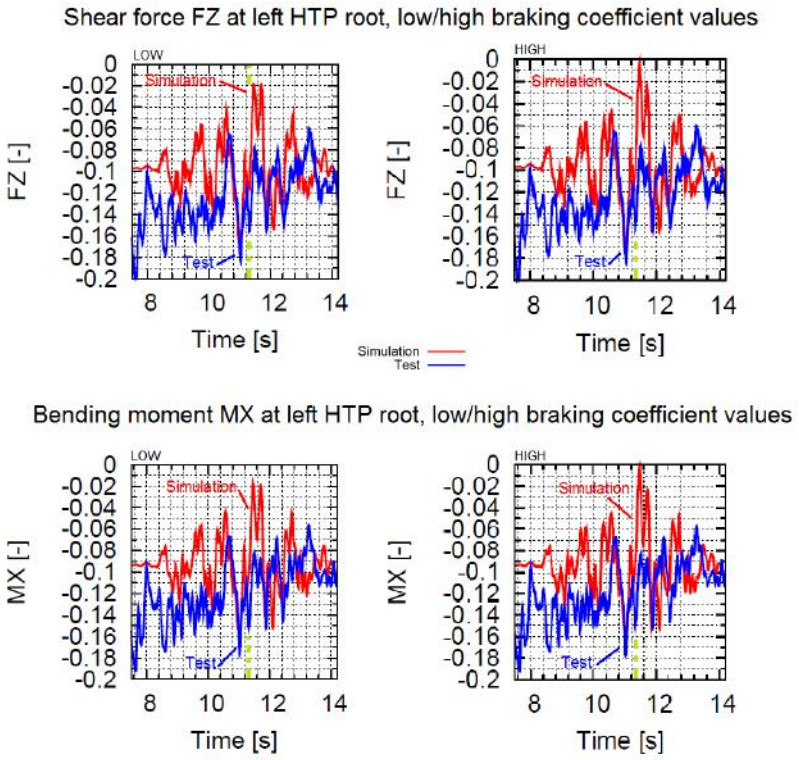

Figure 4.28 Loads at HTP root: low μ (left), high μ (right). Landing A

It can be appreciated that the numerical and experimental response is still unlevelled at initial instants of time. The reason behind this lies on the 1G load value. On the other hand, the numerical response is adequately matched in shape and frequency to the experimental one

around t_R. The numerical response amplitude has increased considerably with respect to initial and intermediate simulation results. Besides, the numerical response amplitude is slightly increased when considering higher overall braking coefficient values. Note that the time delay found between respective responses is no longer present.

The low pressure chamber gas pressure time variation is illustrated in order to directly assess the effect the braking coefficients, V_0 and V_l have on a specific landing gear component numerical response.

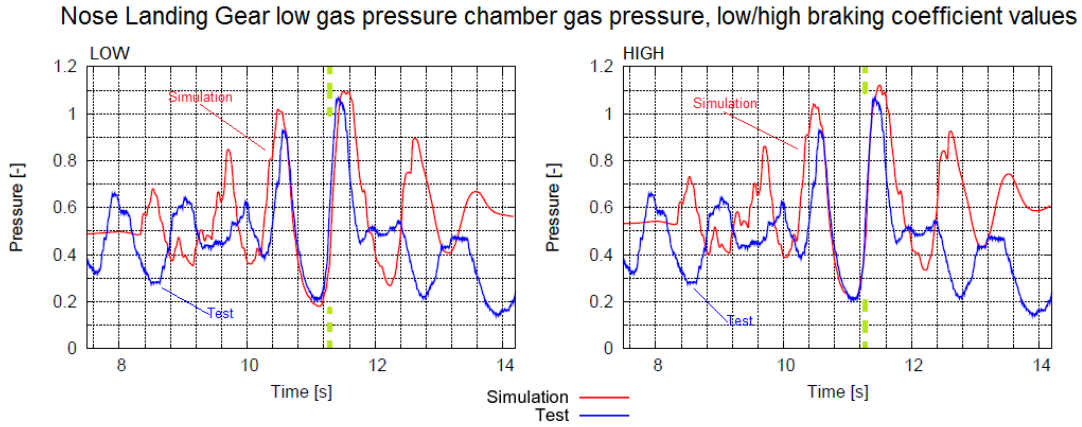

Figure 4.29 Nose landing gear gas pressure: low μ (left), high μ (right). Landing A

It is acknowledged that the numerical response is not matched outside the time-window central section. Nevertheless, the numerical response is coupled with the experimental one around t_R. The response shape and frequency are utterly reproduced. It should be denoted that the numerical response has increased in amplitude with respect to previous results, and it is concluded to be conservative since the experimental response lies within the amplitude range established by the numerical one. On the other hand, the delay encountered between respective responses is no longer present. Both responses are levelled.

Note that lower overall braking coefficients enhance the representation of valley values, whilst higher braking coefficient values are embraced to reach peak values. This phenomenon is illustrated at t_R, for instance.

Since the high pressure chamber is activated in Landing A during a time fraction, the underlying numerical phenomena is observed whenever different braking coefficient values are introduced: the high pressure chamber works once when low braking coefficient values are used, whereas it works twice by applying high braking coefficient values.

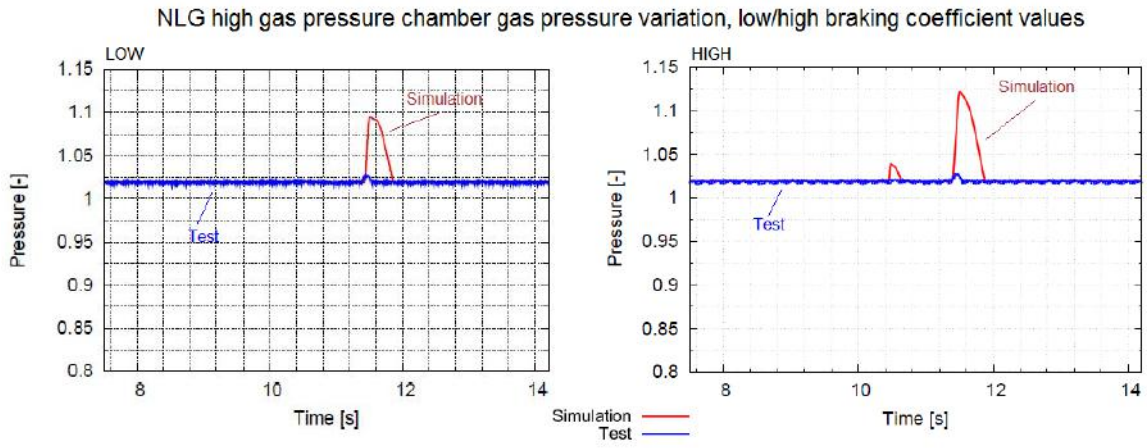

Figure 4.30 NLG high gas pressure chamber pressure variation: low μ (left), high μ (right)

4.4.2 Landing B

The comparison between the numerical and experimental response of Landing B wing root, HTP root and nose landing gear selected magnitudes is provided in the following lines. Again, low and high braking coefficient values are utilised to analyse the effect they caused on the response.

μ	LFW	LMD	LAF	RFW	RMD	RAF
Low μ	0.4	0.3	0.4	0.54	0.3	0.23
High μ	0.5	0.35	0.5	0.6	0.3	0.3

Table 4.3 Landing B braking coefficients

In Figure 4.31, the numerical and experimental responses regarding the loads acting at the wing root are depicted. A conservative numerical response is retrieved since the experimental response values stay within the range delimited by the numerical response amplitude. This phenomenon is illustrated around $t_R = 12.25s$.

Besides, the numerical and experimental response tend to be matched in frequency and shape at that particular instant of time, as well. The numerical response amplitude is enlarged with respect to previous results.

The governing shear force and bending moment time histories at the HTP root are illustrated in Figure 4.32.

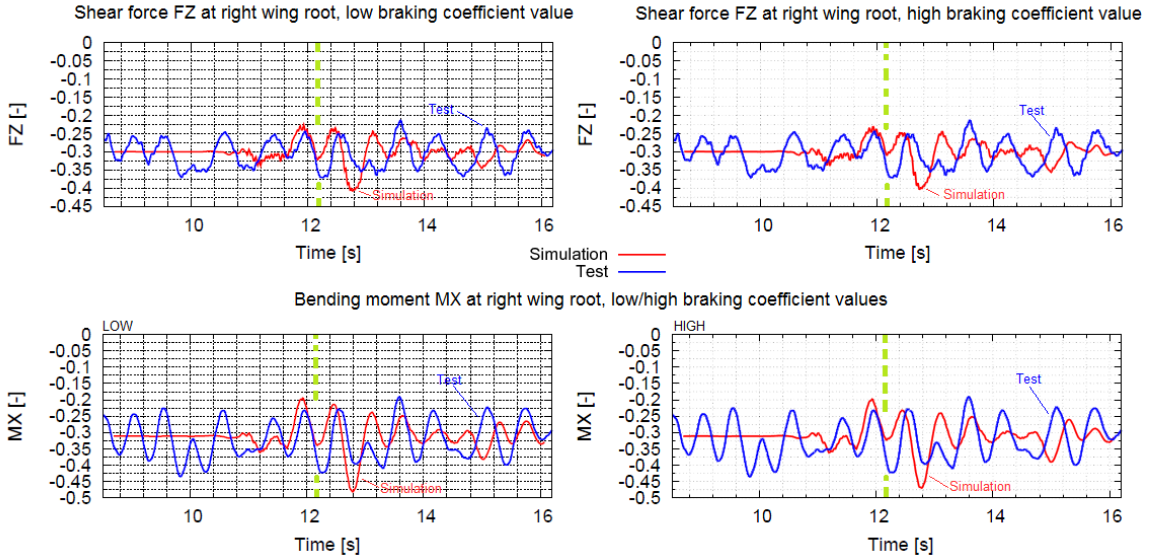

Figure 4.31 Loads at wing root: low μ (left), high μ (right). Landing B

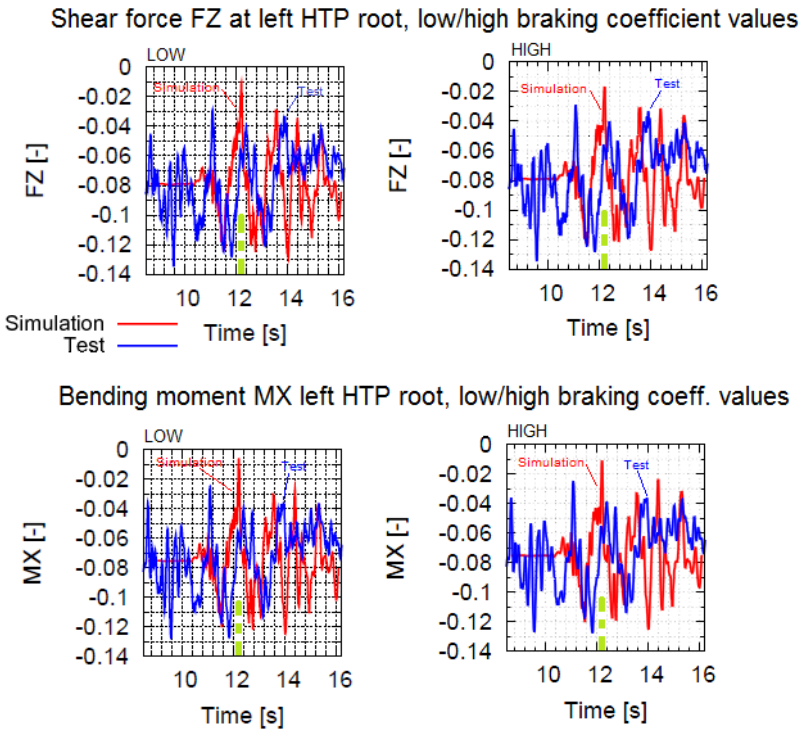

Figure 4.32 Loads at HTP root: low μ (left), high μ (right). Landing B

Again, a conservative numerical response is gathered. Thus, it can be concluded that the amplitude has grown if compared to precedent results. The main improvement which can

be highlighted is devoted to the correction of the time delay displayed in previous HTP root-related figures. Hence, the frequency, shape and position are thoroughly improved with respect to older trials.

The numerical nose landing gear shock absorber low gas pressure variation is compared to the respective experimental response in Figure 4.33.

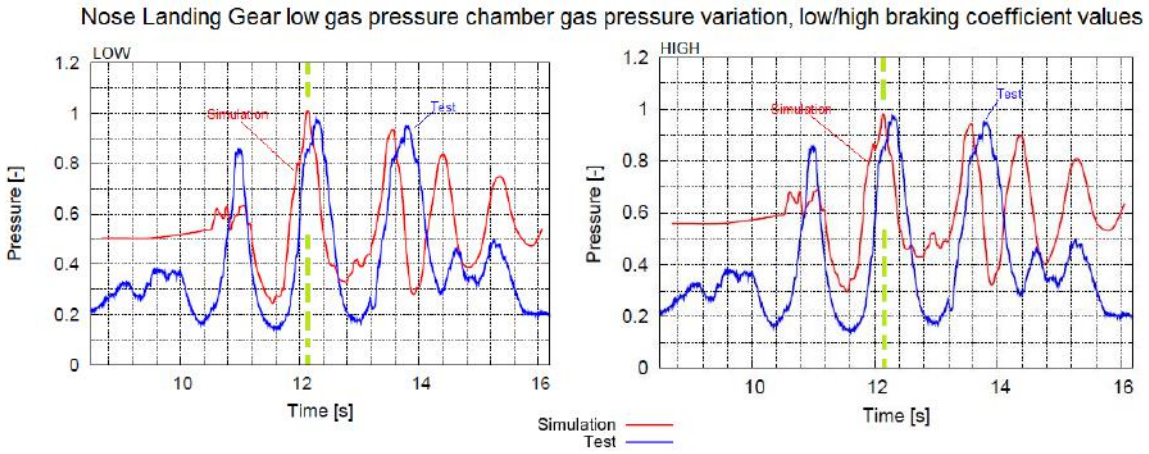

Figure 4.33 Nose landing gear gas pressure: low μ (left), high μ (right). Landing B

The numerical response has improved considerably when it comes to frequency and shape. It can be said to be partially matched with the experimental one at t_R. The time delay presented in intermediate results is no longer perceived, although a subtle delay is still required to be corrected.

It is remarked that higher braking coefficients allow the numerical response to reproduce peak values, whist low braking coefficients to reproduce valley values. However, the numerical response amplitude is still not wide enough to match valley and peak values at the same time. A noteworthy difference between respective responses is perceived at bottom values.

4.4.3 Landing C

The comparison between the experimental and numerical results gathered for Landing C are presented in the current subsection. The loads acting at the wing and HTP root, together with the nose landing gear gas pressure variation are computed using two approaches concerning the overall braking coefficient value.

μ	LFW	LMD	LAF	RFW	RMD	RAF
Low μ	0.17	0.2	0.3	0.35	0.26	0.3
High μ	0.29	0.3	0.5	0.46	0.45	0.3

Table 4.4 Landing C braking coefficients

In Figure 4.34, the shear force and bending moment acting at the wing root are depicted along a determined time span.

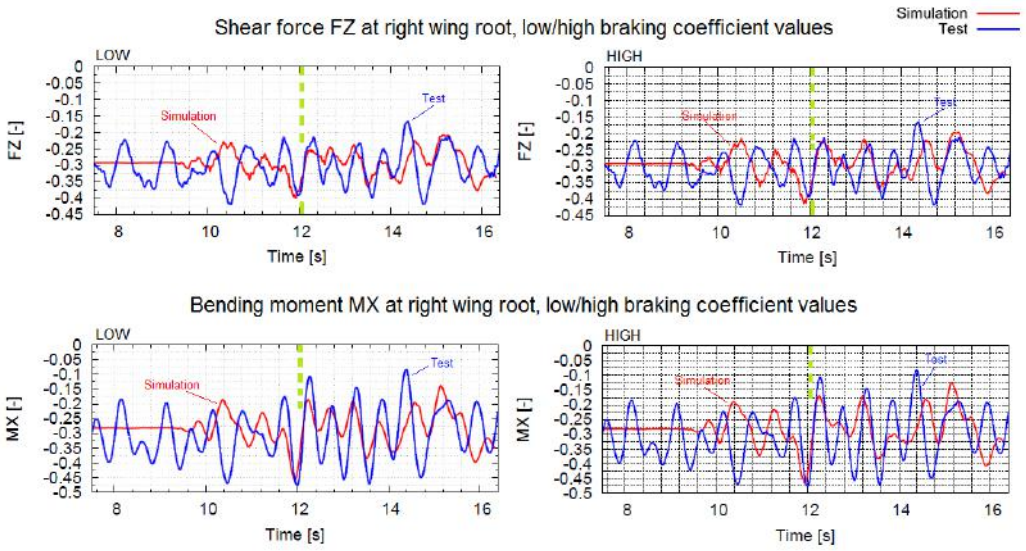

Figure 4.34 Loads at wing root: low μ (left), high μ (right). Landing C

The numerical response is matched in terms of frequency and shape around $t_R = 12.125s$ to the experimental one. Nonetheless, the numerical response is dissimilar to the experimental one outside the time-window central section. The numerical sampling amplitude has increased with respect to previous results, and the shape is intensified as well. In fact, a further amplitude enlargement is required to reproduce experimental extreme values or to retrieve a conservative numerical response.

The numerical HTP root magnitudes are coupled with the experimental ones at t_R in terms of shape, frequency and amplitude. Nevertheless, both responses tend to disassociate outside central time values. They are even unlevelled in terms of magnitude and seem to be out of phase from t_R onwards.

It is appreciated, though, that higher overall braking coefficient values make the numerical response reach bottom values easily (note that HTP root shear force and bending moment are negative-valued magnitudes).

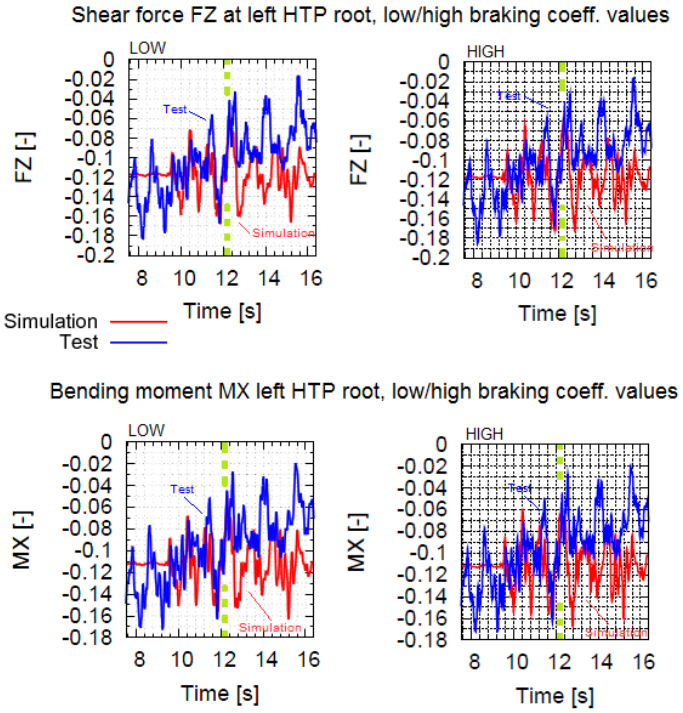

Figure 4.35 Loads at HTP root: low μ (left), high μ (right). Landing C

In Figure 4.36, the nose landing gear low gas pressure variation in time is shown. Again, the numerical response is matched in terms of frequency and shape around t_R.

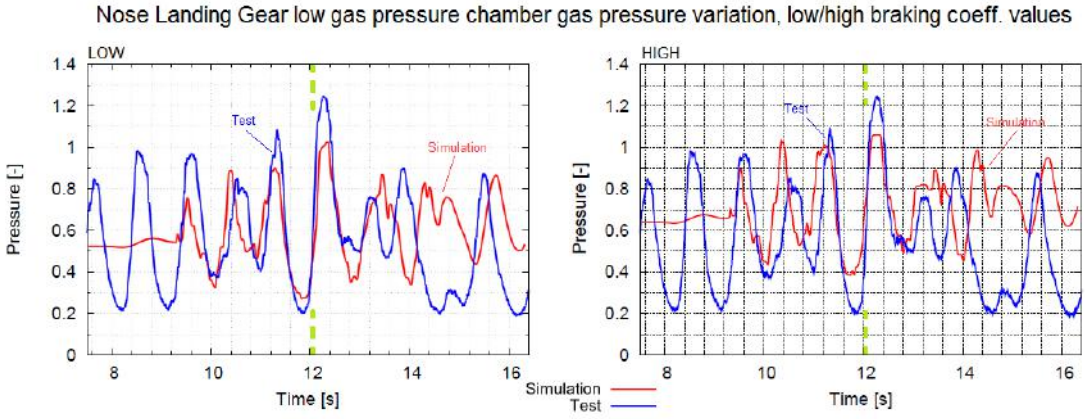

Figure 4.36 Nose landing gear gas pressure: low μ (left), high μ (right). Landing C

By comparing the current results with previous simulation batches, it is perceived that the numerical amplitude is widened, albeit not sufficiently to reach experimental extreme values, and the time delay issue is already fixed.

The effect the braking coefficient has on the numerical response is depicted in Figure 4.36, as well. Low overall braking coefficient values enhance the numerical response to reach valley values. Oppositely, a higher overall braking coefficient value makes the numerical response be positioned above the latter so that peak values are reproduced.

4.4.4 Final stage concluding remarks

The principal improvement achieved after performing the last set of numerical simulations is related to the disappearance of the time delay found between numerical and experimental responses. Therefore, it can be concluded that the runway roughness profile adaptation to include the speed variation, which indeed exists during operation, is key to fix this issue.

The dissimilar time shift found in landing gear and aircraft components, respectively, is mended by applying this new runway roughness profile tuning process. Although the simulation is still performed at constant taxi speed, the real speed variation phenomena occurring during the taxi tests is introduced into the simulation within the runway model.

Adversely, it is perceived that both responses tend to be matched around a given reference time instant, whist they are fairly coupled outside the time-window central section. This is explained by the fact of introducing a vaguely similar runway roughness profile to that found during tests.

When it comes to computing the specific runway profile applicable to each taxi case within a given time-window, the underlying phenomena outside the window central section may be found to be incomplete, since a given runway feature may be deep cut at a precise point defined by the time-window. Moreover, if the precedent aircraft historical trend, in terms of pitch angle for instance, were acknowledged, the numerical response would present realistic patterns at initial time instants, pairing both experimental and numerical responses in a more accurate manner.

Since the runway excitation is distinct from the real one, the responses are indeed different, as well.

The addition of finer time histories of external forces and moments along with more precise braking coefficients to each leg made the numerical response amplitude increase to reproduce the aircraft experimental results with higher fidelity.

Moreover, it is determined, in general terms, that the introduction of lower overall braking coefficient values enhances the reproduction of valley values, whilst peak values are

sharpened by using higher overall braking coefficient values. These phenomena can be easily appreciated in the responses given by landing gear components. A subtle perception of the description above is found in aircraft components response.

Finally, the last milestone worth mentioning is related to the tuning of V_0 and V_l initial values so that they match the ones found during operation. It is observed that this modification has also impact on the landing gear response amplitude. The idea behind this adjustment is to level the experimental and numerical responses given by single landing gear components, as well.

The nose landing gear low pressure chamber gas pressure variation in time for Landing A is a good example to prove that the numerical response amplitude is widened and levelled with respect to older results. Furthermore, the numerical shock absorber curve is matched to the experimental one (Figure 4.37).

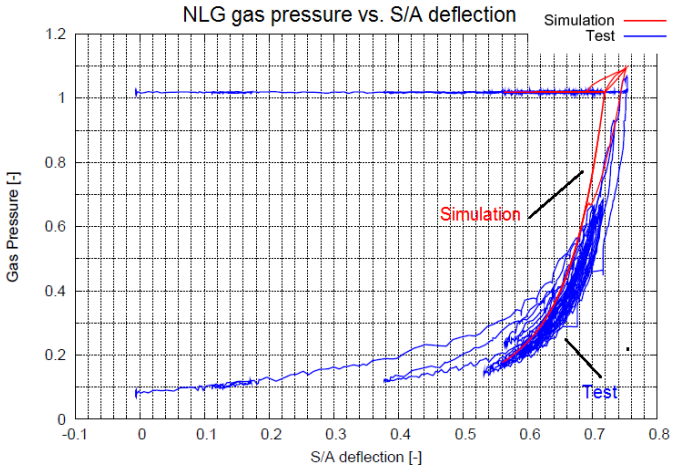

Figure 4.37 Nose landing gear shock absorber curve, Landing A

Landing B numerical gas pressure response is considered to be the worst response among these three landings, since the amplitude is not wide enough to cover the extent the experimental response amplitude demands. As a result, valley values are not reproduced in detail.

As it can be appreciated in Figure 4.38, the numerical nose landing gear stroke and hence, shock absorber curve, is completely unlevelled, unmatched and outsized with respect to the experimental response. The numerical shock absorber curve presents a different slope to that found in the experimental one. It is concluded that a poor matching between landing gear magnitudes will result in a cumulative inappropriate gas pressure pairing.

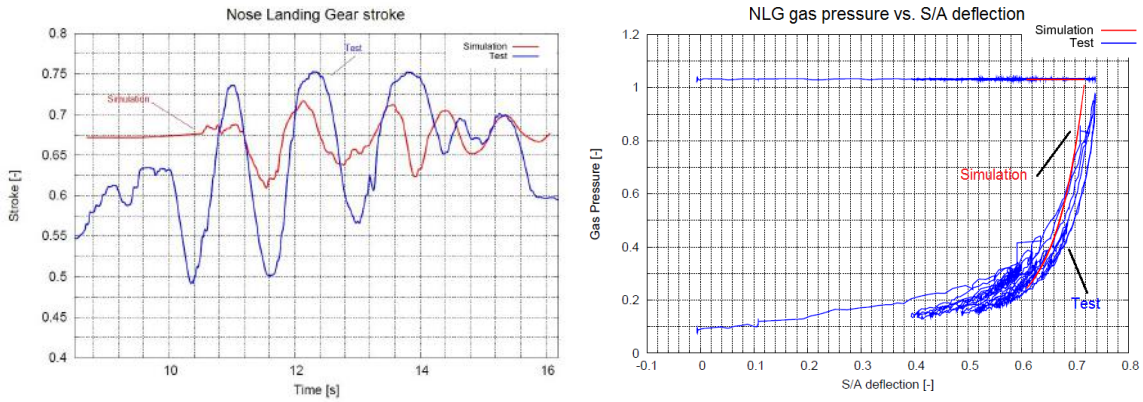

(a) NLG stroke

(b) NLG shock absorber curve

Figure 4.38 Further nose landing gear magnitudes, Landing B

Chapter 5

Results elaboration

A wrap-up of the work performed to reach the results gathered in precedent Chapters is presented herein. The major highlights towards the improvement of numerical results are enclosed, as well. Finally, the effect the braking coefficients present on the taxi problem is described in detail.

5.1 Digestion of results

The work performed to achieve major improvements is based upon four fundamental pillars:

- Introduction of external loads time histories
- Shock absorber curve fitting
- Runway adaptation
- Selection of adequate braking coefficients to each main landing gear leg

Among all concluding results gathered in Chapter 4, those referred to Landing A should be stressed since the initial predefined requirements aimed to the high quality attainment of numerical responses are met. These not only include the acquisition of an accurate numerical to experimental response matching but also the achievement of a conservative numerical model.

Consequentially, Landing A final results are utilised in the present Chapter to provide a concluding general picture of the problem tackled through this Final Thesis. Moreover, the detailed contribution of each of the four aforementioned points to the achievement of final results is also included.

External loads time histories

DYNTAXI module allows the incorporation of constant Fz_{CG}, Mx_{CG} and My_{CG} values or the introduction of Fz_{CG} and My_{CG} time histories. It was appreciated during the tests carried out along the taxi campaign that the external loads (Fz_{CG}, Mx_{CG} and My_{CG}) acting at the aircraft centre of gravity were far from constant. Thus, a realistic approach to numerically reproduce said variation includes the introduction of Fz_{CG} and My_{CG} as time histories.

Otherwise, the contribution of Fz_{CG} and My_{CG} to the final aircraft response is found to be more critical than the one provided by Mx_{CG}. Because of this, DYNTAXI upgrades were primarily focused on the integration of Fz_{CG} and My_{CG} as time histories, maintaining Mx_{CG} as a constant value input.

Said time histories are delivered as a text file where up to three columns can be filled. Each row comprises an instant of time (within a specific time-window) along with a precise Fz_{CG} and My_{CG} value applicable to the problem at that particular instant of time. Fz_{CG} and My_{CG} are the result of performing a static balance (computation of total vertical force and pitching moment at the aircraft centre of gravity so that the summation of forces and moments is zero). To do that, the elevator deflection angle, elevator trim angle, aircraft angle of attack, total thrust force and aircraft horizontal speed variation in time, along a predefined time-window, are taken into consideration. The number of rows the file contains is unlimited. In fact, it is related to the time step used to model the complete time history. The complete time history of external loads is computed by DYNTAXI. To do that, a linear interpolation method is applied to get force and moment values within the time interval defined by the user through the time step.

To choose an appropriate time step to obtain accurate Fz_{CG} and My_{CG} time histories, it should be noted the fact that relevant experimental data, such as the elevator deflection angle, suffer a rapid and abrupt change within a time span smaller than 0.5 seconds. Besides, the numerical aircraft response shape yielded after performing numerical simulations is found to be much more similar to the experimental one whenever the time step used to model external loads time histories is diminished. In other words, by using 0.1 second-accuracy time histories, the brisk variations of Fz_{CG} and My_{CG} related magnitudes are captured in a more accurate manner than if 0.5 second-time-step time histories were used, instead. Hence, the actual aircraft behaviour is represented in an meticulous manner whenever the time step is reduced.

The importance of parameters such as elevator deflection[1] angle or aircraft angle of attack to the time history computation, and hence, to shape the numerical response to that found experimentally is illustrated in the figure below.

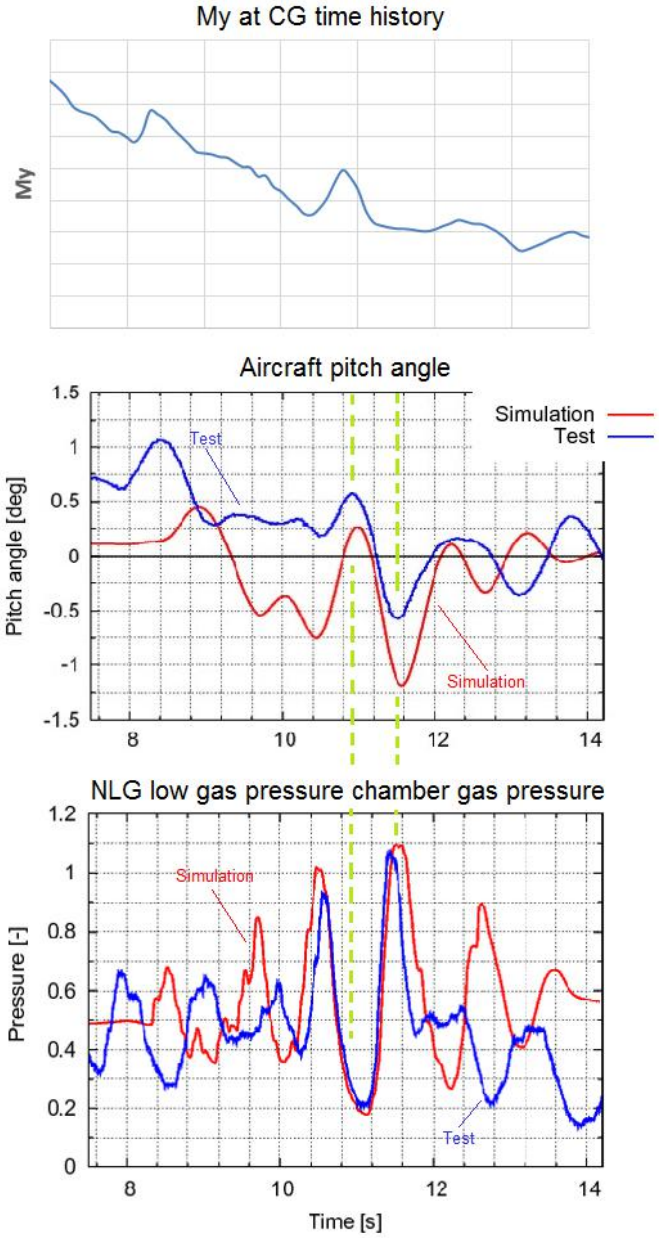

Figure 5.1 Time history effect on aircraft response

This figure includes the My_{CG} time history which was introduced to DYNTAXI, the experimental and numerical pitch angle (pitch angle and aircraft angle of attack are interchangeable

[1]Figure 4.11 acts as an example where the evolution of the elevator deflection angle in time along a given time-window is illustrated.

terms when the aircraft is operating on ground, i.e. taxi) and nose landing gear low gas pressure chamber gas pressure response.

At first glance, it is perceived that the introduced pitching moment time history is similar in shape, albeit less pronounced, to the experimental pitch angle (aircraft angle of attack) during the tests.

In addition, it is appreciated that the numerical pitch angle response gathered, after performing a numerical simulation, is analogous in shape to the experimental one. However, note that the experimental response lies above the numerical one. The historical pitch angle trend the aircraft presented prior to the time window should be included to level the numerical response to the experimental one. On the other hand, bear in mind that the existing difference between both responses is approximately 0.6 degrees.

The inclusion of external loads time histories to improve the resulting numerical response also permits to achieve a global picture of the aircraft behaviour during operation. In this manner, it is possible to relate the global pitch angle to the nose landing gear low pressure chamber gas pressure variation, for instance. It should be pointed out that other magnitudes such as nose landing gear shock absorber stroke present a logical and expected response which is coherent and related to the overall aircraft behaviour.

The green dashed lines point to two remarkable features: the valley and peak gas pressure values reached during operation. As a matter of fact, valley values represent those points in operation where the gas pressure is lowest. This implies that the shock absorber is extended and, thus, the aircraft nose landing gear might be aloft or with minimum ground contact. Likewise, this is translated into a positive nose up pitching angle. Said valley value denotes an increment in the pitch angle. A peak pitch angle value is reached.

On the other hand, the peak gas pressure value implies a shock absorber compression: loads are acting on the nose landing gear which are required to be overcome by activating the shock absorber. Moreover, this is translated into a negative nose down pitch angle. It is followed by a pitch angle decrease, a pitch angle valley value is reached.

It can be concluded that the addition of external loads time histories to the numerical simulation enhances the response shape of directly (pitch angle) and indirectly related (landing gear components response) magnitudes. The approach of introducing transient aircraft phenomena to the simulation, such as the elevator deflection angle variation, is a step forward towards the acquisition of realistic numerical responses.

Shock absorber curve fitting

The attainment of matched and levelled numerical and experimental responses is possible thanks to the shock absorber curve tuning. This modification primarily affects the responses gathered at the landing gear. Landing gear magnitudes such as gas pressure or shock absorber stroke are principally influenced by this adjustment.

The shock absorber curve is defined by the gas pressure variation with respect to the shock absorber stroke. Therefore, by adjusting the underlying parameters which define the shock absorber curve, a modification in individual gas pressure and shock absorber stroke responses is obtained.

This fitting is performed by introducing into the numerical simulation the initial gas pressure P_0 and initial gas V_0 and liquid volume V_l each shock absorber presented at rest (aloft, before landing, with the landing gear extended) during the experimental tests. These three parameters are relevant when it comes to defining the shock absorber curve.

In fact, the introduction of modified parameters to the numerical simulation adds a degree of realism to the results since these parameters varied from test to test. The drop of oil volume along the campaign was compensated by the addition of gas (gas volume increment). Oil leaks are needed to be accounted for. Their variation was found to be around $\pm 5\%$ reference values. This major constraint is adopted when introducing said changes into the numerical simulation process.

P_0, V_0 and V_l help the numerical shock absorber curves match the experimental ones in shape and position. Consequentially, the respective gas pressure and shock absorber stroke readings are matched. This transformation is shown in Figure 4.23, Figure 4.24 and Figure 4.25 (pre-fitting), and Figure 4.37 (post-fitting).

As it is appreciated in Figure 5.2, the numerical and experimental responses given by the gas pressure and shock absorber stroke are levelled once the parameters described above are adjusted. As a result, the numerical shock absorber curve is coupled with the experimental one. This fitting is performed in every landing gear leg to obtain an overall matched and levelled response.

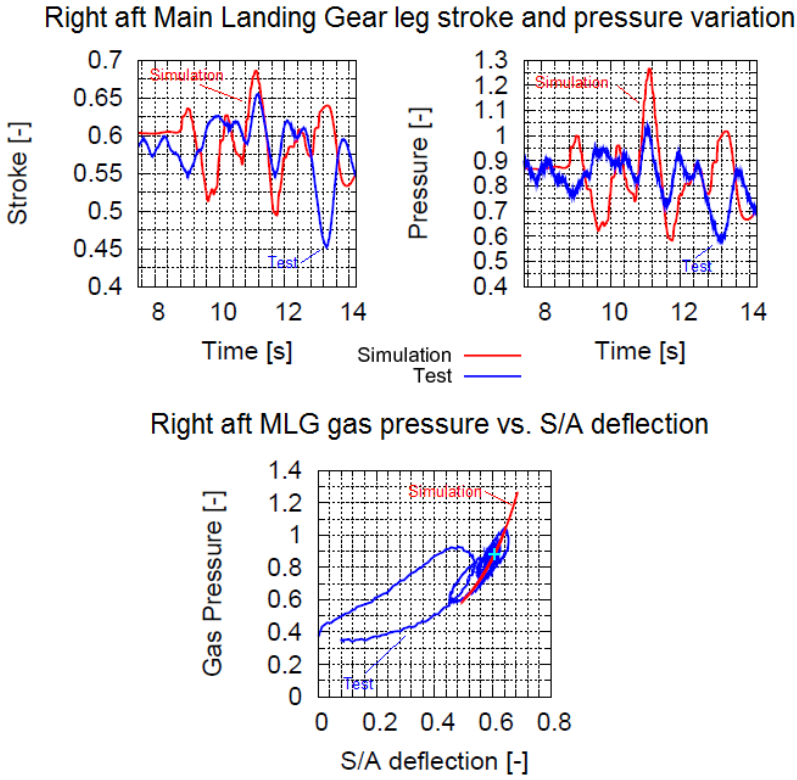

Figure 5.2 Shock absorber curve fitting effect on landing gear magnitudes (Right Aft leg)

Runway adaptation

The numerical aircraft response to runway excitation is computed at constant taxi speed. Actually, the taxi operations followed by a landing phase present a decrease in velocity as far as braking action takes place. As a result, the numerical aircraft and landing gear response was shifted in time (aircraft components time delay was different to the landing gear components time delay) with respect to the experimental response.

To fix this issue, the velocity variation the aircraft was subjected to is indirectly introduced within the corresponding runway roughness profile to each leg. Prior to this major adjustment, the runway roughness profile used by DYNTAXI was the one originally measured by telemetry which reflects the runway topographic features as they are. This modification provides a new runway roughness profile where the original runway profile features are presented in way they are run at non-constant velocity, whilst the taxi case is still simulated at constant taxi speed. As a result, the time delay presented between selected magnitudes is corrected as it is illustrated in Figure 4.15 (pre-adaptation) and Figure 4.29 (post-adaptation).

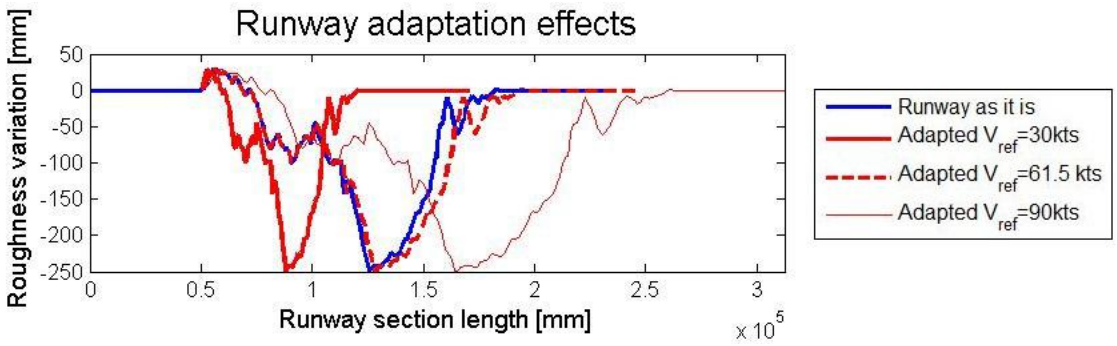

Figure 5.3 Runway adaptation effects

By correcting the time delay found between numerical and experimental responses, the numerical response sampling frequency is improved, thus, a matching between numerical and experimental responses is enhanced.

The numerical to experimental response match is intensified at the region defined by the reference time instant t_R, denoted as *Matching range* in Figure 5.4. Oppositely, it is detected that the numerical and experimental responses display a different shape and hence, they do not match, whenever such responses are located away from the matching range. The reasons behind these phenomena are twofold: different runway roughness profile to that experimentally found at that particular section, and the time-window is not wide enough to capture entire noteworthy profile features.

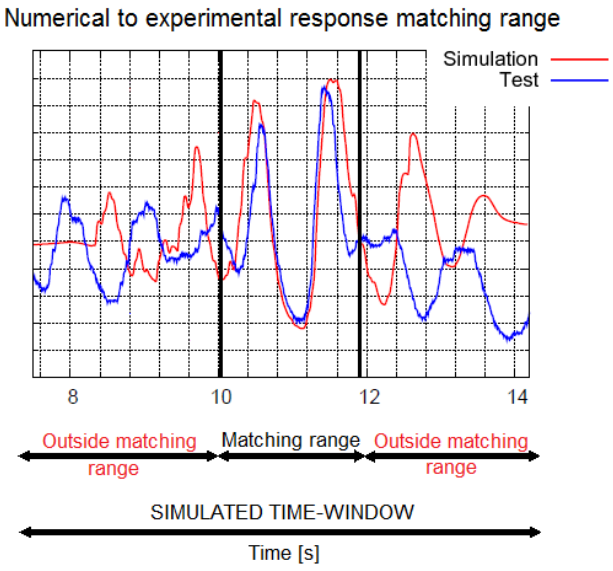

Figure 5.4 Matching range

The portion of runway roughness profile which corresponds to the selected time-window is smoothed by a 1-cosine mask at the adjacent points between the runway roughness profile and the flat pattern. The runway junction is nothing but an artificial element which is added to the profile to make the numerical simulation more robust. Besides, it does not correspond to the real runway profile the aircraft is operating on. Furthermore, the selected time-window may not include the whole runway bump which makes the aircraft behave in a determined manner. To overcome this problem, the time-window is extended so that the complete runway feature is covered.

Braking coefficients

The braking action is primarily analysed by delving into the braking loads exerted on the main landing gear longitudinal links. These provide a direct measurement of the braking pattern followed during operation. As it is perceived in Figure 5.5, the braking sequence pursued by the right mid main landing gear leg is nearly constant. Notice that when the signal drops to zero, braking action is no longer applied. On the contrary, two distinct braking patterns are distinguished in the right aft main landing gear longitudinal link: an almost constant pattern is observed from 10 to 12 seconds, and a linearly increasing sequence up to 10 seconds.

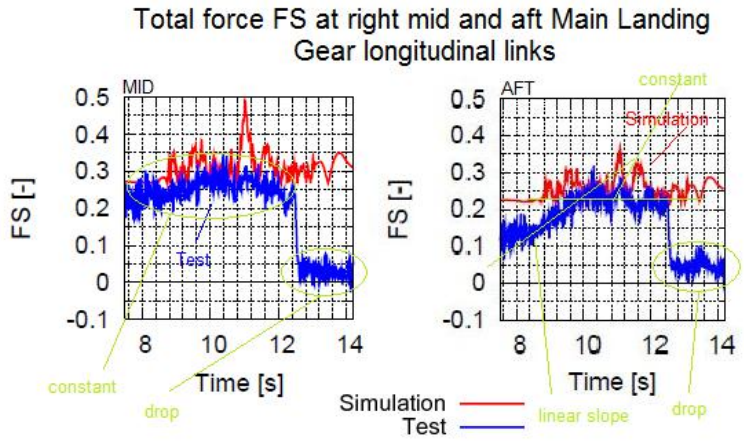

Figure 5.5 Braking loads on longitudinal links

The criteria followed to shortlist taxi cases praised the appearance of constant braking patterns. This is explained by having to introduce a constant braking coefficient value to each main landing gear leg through the numerical simulation tool. A constant braking coefficient value implies that the braking action pattern is constant, thus, the braking action response is successfully reproduced by the numerical simulation software. Since braking coefficients

time histories cannot be introduced due to the current capabilities the software presents, a non-constant braking pattern may not be likely to be emulated in detail.

The braking coefficient is defined as the ratio between the horizontal and vertical force acting on a particular landing gear leg wheel axle $\mu = Fx/Fz$. In non-constant braking sequences, said parameter may fluctuate around a given value. Continuing with the main landing gear legs kept as example, Figure 5.6 gives an insight on how the braking coefficient variation looks.

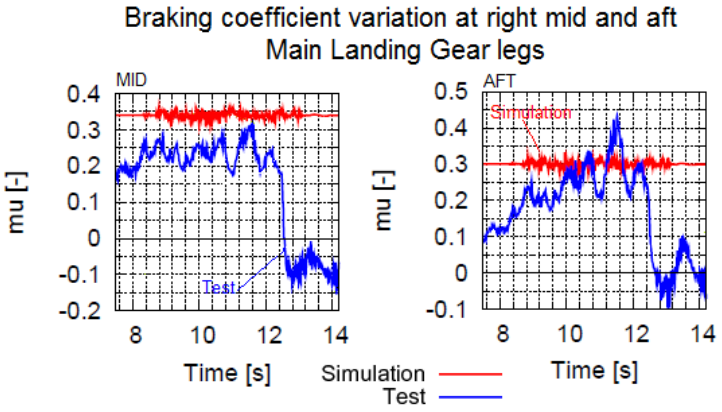

Figure 5.6 Braking coefficients

As expected, the first plot shows a fluctuation around a given mean value since the braking pattern was found to be nearly constant. On the other hand, the second plot illustrates a noteworthy variation up to 12 seconds as a non-constant braking sequence precedes.

Different braking coefficient constant values (one to each leg) can be introduced to DYNTAXI module. To reproduce the experimental response accurately, it is appreciated that the experimental braking coefficients oscillate around a given value. Therefore, two simulation batches are considered where different braking coefficients are applied. In fact, the braking coefficient values are either introduced as a mean experimental braking coefficient value or as the maximum value presented in each time-window. A remarkable difference is perceived whether maximum values or mean values are used: maximum values can even double mean braking coefficient values.

As a conclusion, it is determined that low braking coefficient values enhances the reproduction of valley values and high braking coefficient values, the emulation of peak values. Figure 5.7 presents in a clear way the aforementioned phenomena.

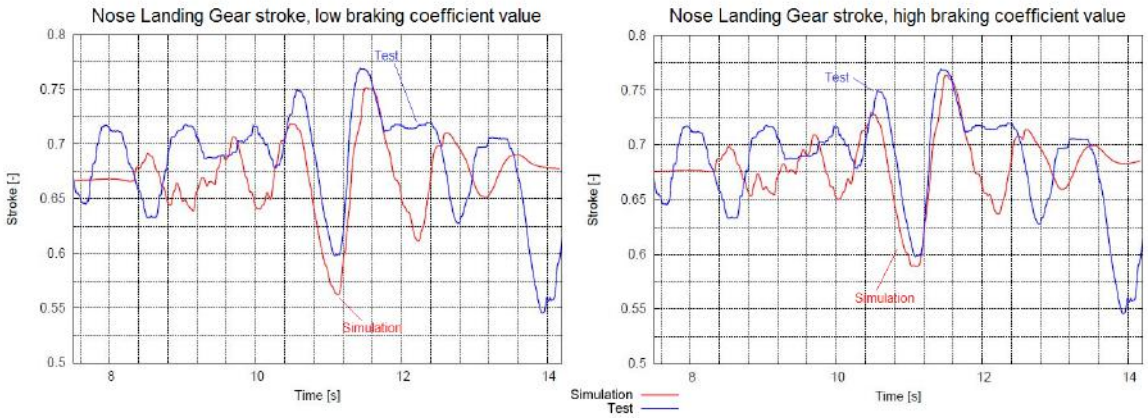

Figure 5.7 NLG stroke variation: low μ (left), high μ (right)

In this manner, the numerical response amplitude is not only changed in landing gear components, the overall aircraft response also presents a subtle variation when introducing different braking coefficient magnitudes. As a result, the numerical response amplitude is tuned by applying specific braking coefficient approaches.

The numerical response shape, frequency and level are modified by taking into consideration the three latter major points described: external loads time histories, shock absorber curve fitting and runway adaptation.

5.2 Impact of braking coefficients on taxi loads

In previous section, the effect that the braking coefficient values have on the numerical response is discussed. As the experimental braking coefficient values may fluctuate abruptly along a defined time-window, two methods can be followed to input braking coefficient values to the numerical simulation. It is concluded that high (maximum values) braking coefficient values help the numerical response reach peak values more easily, whilst low (mean values) values enhance the reproduction of valley values, instead.

As a matter of fact, given a specific vertical force acting on a particular main landing gear leg wheel axle, a higher braking coefficient value implies that the horizontal force acting on the wheel axle is also higher than if lower braking coefficient values were used.

In the following figure, the vertical and horizontal force acting on the left mid main landing gear leg wheel axle is depicted along with the braking coefficient variation corresponding to said leg.

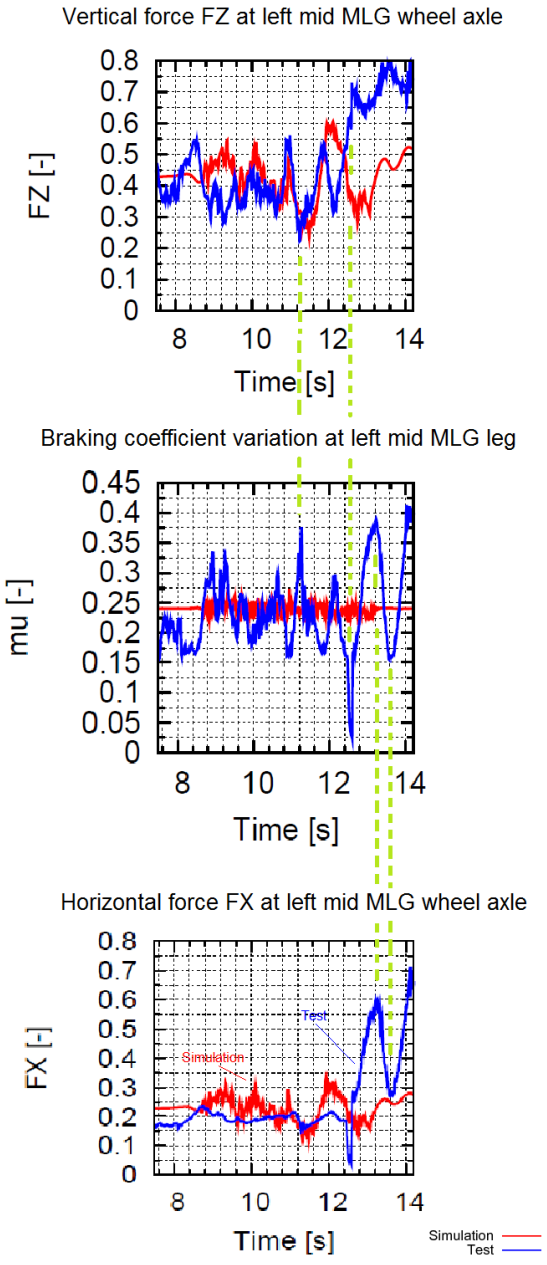

Figure 5.8 Fx and Fz on left mid wheel axle plus μ variation

As it is appreciated, the braking coefficient values introduced into the numerical simulation correspond to the mean braking coefficient value obtained within the time-window. On the

other hand, the relation between the variation the experimental braking coefficients and the vertical force on the wheel axle take is also illustrated. The green dashed lines act as an aid to point two braking coefficient extreme values to the respective vertical force values. It is perceived that whenever the braking coefficient magnitude reaches a peak, the corresponding vertical force value specified at the wheel axle is located at a valley, and vice-versa. Hence, the vertical force response at the wheel axle can be stated to behave oppositely to the braking coefficient variation.

Besides, the variation the horizontal force exerted on the wheel axle presents resembles to the braking coefficient variation pattern. Consequently, these magnitudes' responses are said to be in phase.

It is remarkable to compare the vertical forces acting on the nose landing gear and left mid main landing gear legs wheel axle altogether. This is depicted in Figure 5.9. Note that the pressure and vertical loads acting on the nose landing gear or wheel axle responses present a similar shape. They are interchangeable when it comes to studying the effects produced on the nose landing gear during operation.

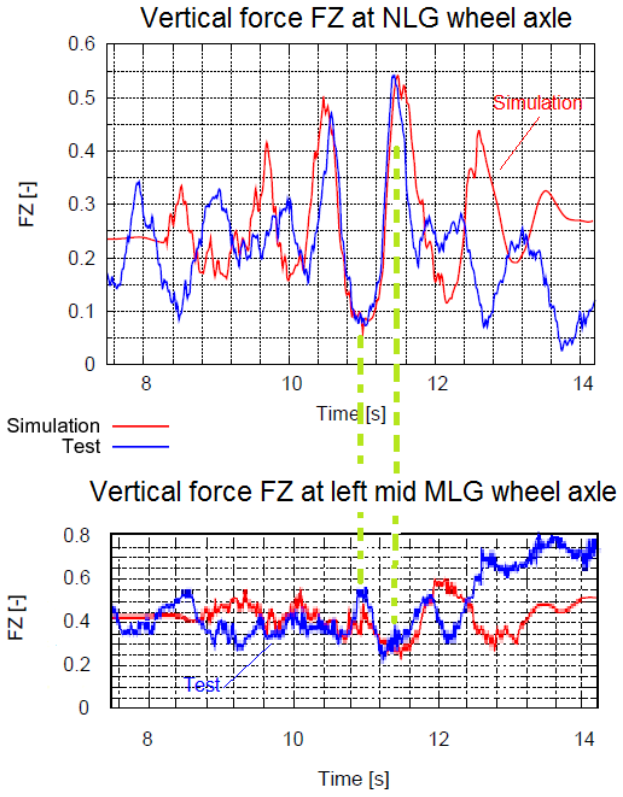

Figure 5.9 Fz on MLG left mid and NLG wheel axle

It is distinguished that when peak loads are reached in the left mid main landing gear leg wheel axle, thus, the braking coefficient value is found to be lowest, the vertical force acting on the nose landing gear wheel axle lies in a valley. In other words, whenever the braking coefficient is determined to be low, a relief in terms of vertical loads is gathered at the nose landing gear, since the force acting at the wheel axle is small (the shock absorber is extended, the nose landing gear leg may even be aloft).

Oppositely, if the braking coefficient is high and hence, the vertical loads acting on the main landing gear legs are low, it results that the vertical forces exerted on the nose landing gear are high.

The braking coefficient extreme cases are explained by means of 2D forces envelopes. In Figure 5.10, an example of typical envelopes is depicted. The forces acting on the right forward and mid wheel axles are illustrated in this particular manner.

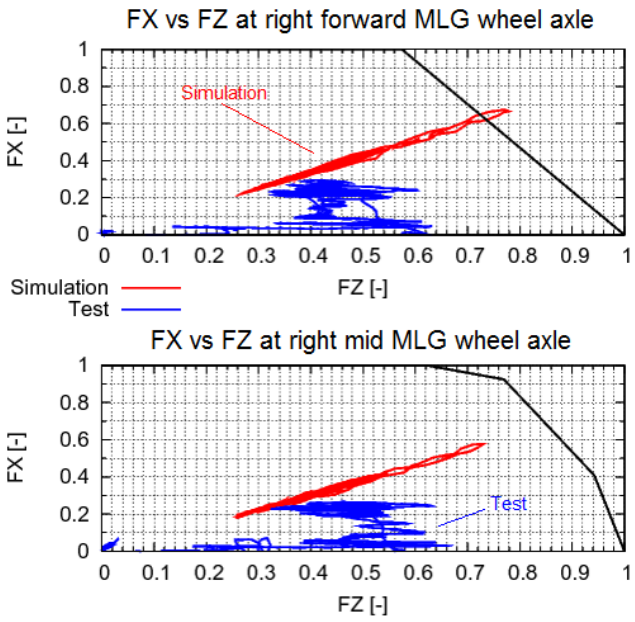

Figure 5.10 Forces at wheel axles 2D envelope

It is perceived, at first glance, that the numerical Fx to Fz variation gets out of the established boundary depicted by the continuous black line in the plot referred to the right forward main landing gear leg. Indeed, said boundary is not delimited by such straight line, it is flexible. What is remarkable to be highlighted is the fact that the numerical Fx to Fz variation presents a linear pattern. Since constant braking coefficient values are introduced to the numerical simulation, the numerical braking coefficient variation along the time-window

subtly oscillates around the inputted braking coefficient constant value. Therefore, the Fx to Fz variation slope is nothing but the constant braking coefficient value assigned to each leg.

Furthermore, note that for increasing Fz numerical values, the numerical Fx magnitude augments accordingly. However, it is experimentally demonstrated in this case that with growing Fz values, the horizontal force values the main landing gear wheel axles present only rise up to a fixed value, no matter how high Fz gets. For a given Fx value, an increasing Fz induces a decrease in the final braking coefficient value a main landing gear leg could reach.

Said experimental constraint is specific for the runs performed at Écury sur Coole runway. As a matter of fact, distinct behavioural patterns are expected to be found at runways of different nature.

Indeed, the fact of reaching a precise Fx value no matter how far Fz increases, inducing a drop in the braking coefficient value, is a direct measurement of soil decohesion. Note that Écury sur Coole runway is prone to present ruts after a specific number of aircraft passes. Écury sur Coole runway soil cohesion is defined to be poorer than Ablitas'. The later presents a much more compacted surface.

As a matter of fact, the Fx to Fz behaviour found at Ablitas runs can be studied by analysing the figure below (Figure 5.11). The time-window is selected so that the maximum nose landing gear shock absorber pressure reached during operation is included.

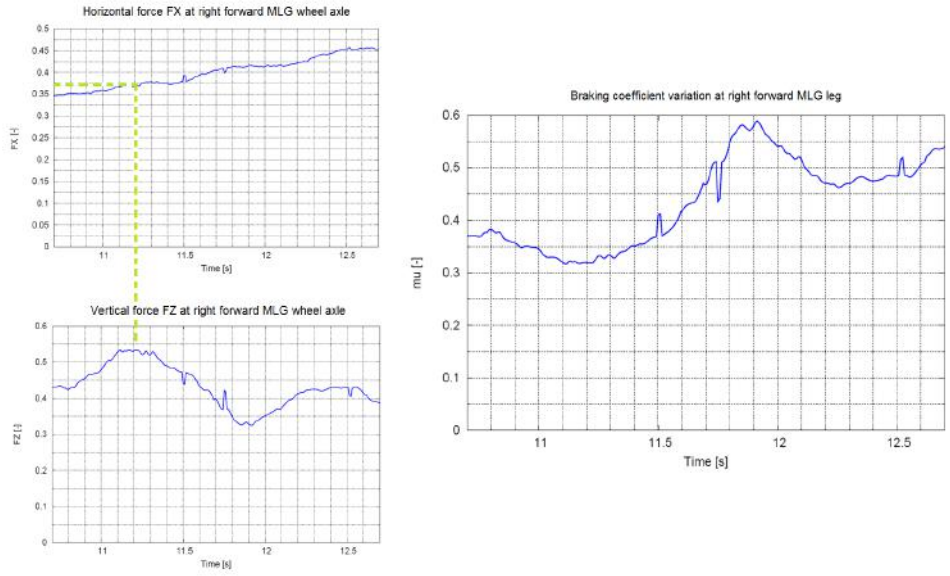

Figure 5.11 Fx, Fz and μ variation, Ablitas

Again, Fz and μ variation pattern is established to be out of phase respectively, whilst Fx and μ response is in phase. A slight Fx variation is perceived along the time-window, no brisk changes are observed. An almost constant Fx response is retrieved. Furthermore, the maximum Fz gathered at the specific time span, $Fz = 0.54$, yields a non-dimensional value of $Fx = 0.37$, which is equivalent to say $\mu = 0.33$. Fx does not drop dramatically with an Fz increment.

An equivalent figure is now provided for a specific Écury sur Coole taxi run.

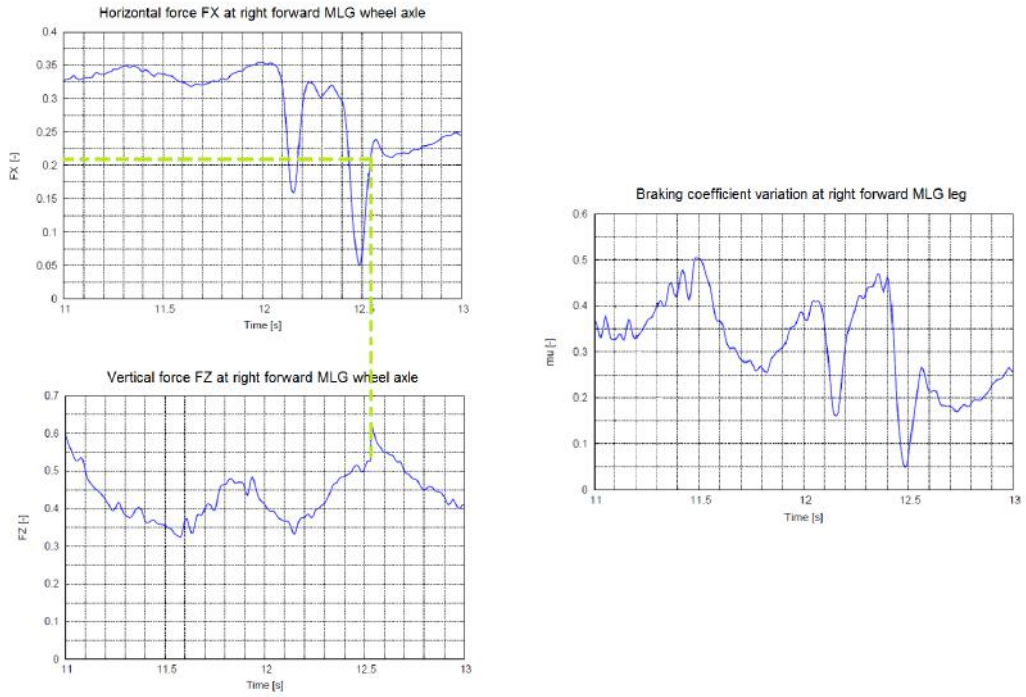

Figure 5.12 Fx, Fz and μ variation, Écury sur Coole

It should be noted that the Fx response presents abrupt precipitation changes whenever Fz increases. In this case, $Fz = 0.54$ induces a value of $Fx = 0.22$ or $\mu = 0.2$, approximately.

It can be concluded that the runway soil nature plays a fundamental role when it comes to establishing the braking capability the aircraft presents during taxi operations. As a result, compacted and cohesive runway surfaces enhance the braking capability since μ can reach higher values (consequentially, higher loads are gathered at the nose landing gear, as well). This reasoning is applied to Ablitas taxi operations.

Contrarily, runway surfaces which are prone to be eroded (cohesion lacking) present a reduced braking action since μ drops considerably. Thus, low braking coefficient values induce a load relief phenomenon at the nose landing gear.

Depending on the runway nature the aircraft operates in, the aircraft can be loaded in a different manner. It is perceived that whenever the aircraft weight is larger, the loads induced at the nose landing gear reach higher values than if the overall aircraft weight is reduced. Taking advantage of the load relief process found at the nose landing gear when operating in poor compacted soils (Écury sur Coole), there is a margin in the amount of weight the aircraft is allowed to carry to reach the loads which would be present if said aircraft were to operate in a compacted surface. The A400M missions weight capability would be improved around a 22% (approximately 23T) by this milestone.

It is evident at this point of the problem that those taxi runs which present braking action were shortlisted, instead of choosing those coming from takeoff runs. The importance of the braking action is embraced to optimise taxi operations.

Chapter 6

Conclusions and future activities

6.1 Conclusions

Design and Certification loops require taxi loads to be computed by following the requirements specified on Airworthiness Regulations relative to taxi. A wide range of velocities and mass states should be considered. The mass state spectrum is comprised of a variety of fuel and payload weight and extreme centre of gravity settings combinations. So far, taxi loads are computed by performing runs at constant taxi speed, symmetric cases are solely taken into account and the external loads acting on the aircraft were assumed to be constant during the run.

The contributions of this Bachelor Thesis to the taxi problem range from computing taxi loads in which the velocity variation found experimentally during tests is included, to the study of asymmetric cases or the variation of external loads in time for a specific mass state.

- The taxi velocity variation along the run is introduced by adapting the corresponding runway profile to each landing gear leg.
- To incorporate the variation of external loads along the run, time histories of forces and moments applied at the aircraft centre of gravity are used.
- Asymmetric cases are analysed with the help of utilising a complete aircraft structural model and the inclusion of a constant rolling moment value applied at the aircraft centre of gravity.

Computation of taxi loads to date	BSc. Thesis contributions to taxi loads computation
Constant taxi velocity	Variable taxi velocity
Constant external loads	Variable external loads
Symmetric cases	Asymmetric cases
Mass states variation	Single mass state

Table 6.1 Final Thesis contributions to taxi loads problem

6.2 Future activities

Further improvements are required to be performed to tune the numerical response beyond. The numerical to experimental response matching is found to be weak outside the Matching range, and imprecise whenever the braking action sequence is far from constant.

The first feature could be boosted by including previous aircraft inertial historical trends prior to entering into a specific time span. Although this is approximately introduced by Fz_{CG} and My_{CG} time histories, a software upgrade should be considered to enable the insertion of rolling moment Mx_{CG} time histories, as well. In fact, it should be recalled that the FCS model is not included within the dynamic model. A FCS model inclusion would permit the introduction of inertial historical trends in a much more accurate manner.

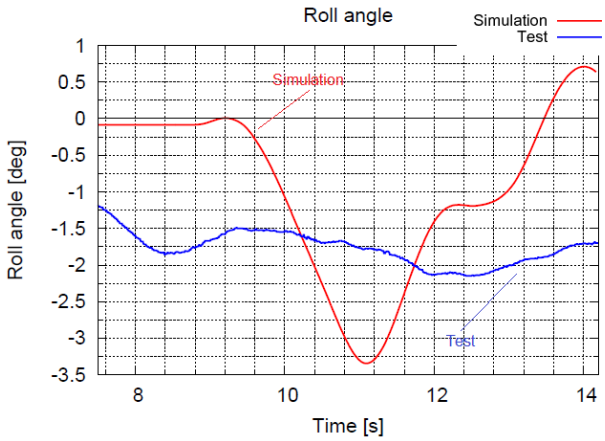

Figure 6.1 Roll angle response, Landing A

With this upgrade, the numerical and experimental response coupling would be intensified outside the Matching range. Not only that, the numerical simulation would gain realism since

the experimental aircraft behaviour (angle of attack or elevator deflection angle variation, to name a few) is incorporated through a FCS model. Moreover, the introduction of a constant mean Mx_{CG} value is not representative as the aircraft roll angle is not held constant during the run (Figure 6.1). The numerical and experimental responses could present a similar shape and magnitude level by approving these improvements.

Furthermore, the numerical aircraft response could be upgraded by modifying the corresponding runway roughness profile whenever taxi runs were performed over previous ruts. In that case, the runway roughness profile would be flattened at specific sections, provoking a smoother response.

Since non-constant braking patterns are hard to be reproduced, a numerical simulation software upgrade should be considered to introduce braking coefficient time histories to each leg, instead of incorporating unrepresentative constant values. Besides, the uncertainty of putting mean or maximum braking coefficient values would vanish.

Lastly, further taxi campaigns should be launched in different runway natures to obtain a global picture of the aircraft braking capability, and ensuing load relief process in unpaved runways. It is established that poor cohesive soils enhance loads reduction at the nose landing gear. It would be beneficial to determine the aircraft behaviour when operating in runways of intermediate cohesion and compactness features. Sand or clay runways would be determinant to fully comprehend the aircraft taxi operation in unpaved runways underlying phenomena.

Bibliography

[1] T.L. Lomax. *Structural Loads Analysis for Commercial Transport Aircraft: Theory and Practice*. AIAA Education Series. 1996.

[2] J.R. Wright and J.E. Cooper. *Introduction to Aircraft Aeroelasticity and Loads*. AIAA education series. John Wiley & Sons, 2007.

[3] J. L. Pérez-Galán, J. A. Portas, J. M. Chorro, J. L. López-Arévalo, and Héctor Climent. Aircraft taxi loads full scale tests and correlation with numerical simulations. *IFASD-2001-080*, 2001.

[4] A. G. Gerardi and A. K. Lohwasser. Computer program for the prediction of aircraft response to runway roughness. *AFWL-TR-73-109*, Volume I and II, 1973.

[5] C. Petiau and A. Celier. Méthode de simulation numérique du système avion atterrisseur. *AGARD-CP-326*, 1982.

[6] C. Maderuelo and H. Climent. Validación de un método analítico para el cálculo de cargas de rodadura. *CASA DT-89-3220*, 1990.

[7] D. Howe. *Aircraft Loading and Structural Layout*. John Wiley & Sons, Ltd, Chichester, 2004.

[8] J. L. Pérez-Galán, L. Benítez, M. Oliver, and H. Climent. Survey of aircraft structural dynamics non-linear problems and some recent solutions. *CEAS-2009-132 European Air & Space Conference*, 2009.

[9] C. Maderuelo, J. L. Pérez-Galán, S. Claverías, H. Climent, and B. Rendueles. Flight test validation of a fully coupled flexible landing gear and flexible aircraft models. *IFASD 2005*, Paper 21, 2005.

[10] B. B Purkayastha and K. K Sarma. *A Digital Phase Locked Loop based Signal and Symbol Recovery System for Wireless Channel*. Springer, 2015.

[11] NTSB. Aircraft accident report: Runway overrun during rejected takeoff global exec-aviation Bombardier Learjet 60, N999LJ. Technical report, NTSB/AAR-10/02, 2008.

[12] U. A .E. Aeronáutica-Civil. Informe técnico de accidentes de aviación con fines de prevención HK-3952. Technical report, Unidad Administrativa Especial de Aeronáutica Civil, 2008.

[13] D. Fédéral. Rapport final de la commission fédérale d'enquête sur les accidents d'aviation PH-KLC. Technical report, Département fédéral des transports, des communications et de l'énergie, 1989.

[14] BEA. Rapport d'enquête etabli suite a l'accident survenu a Bruxelles National le 29 Août 1998 a l'avion Airbus A340 immatriculé OO-SCW. Technical report, BEA, 1998.

[15] EASA. *Certification Specifications and Acceptable Means of Compliance for Large Aeroplanes CS-25*. European Aviation Safety Agency, 2015.

[16] J.L. Pérez Galán and H. Climent. C295m military operation. dynamic taxi loads analysis on unpaved runways. *CASA DT-5-ADD-99011*, 2000.

[17] G. Pastor, J. L. Pérez-Galán, Héctor Climent, A. J. Rodríguez-Jiménez, A. Pérez de la Serna, and S. Veguillas. A400M tests used for dynamic loads model validation. *IFASD-2011-166*, 2011.

[18] EASA. *EASA Type-Certificate Data Sheet No. EASA.A.169 for Airbus A400M.* TCDS No.: EASA.A.169. European Aviation Safety Agency, 2013.

[19] TH Skopinski, William S Aiken Jr, and Wilber B Huston. Calibration of strain-gage installations in aircraft structures for the measurement of flight loads. *NACA Technical Report 1178*, 1954.

Appendix A

List of symbols

α	Angle of attack
$\boldsymbol{B}$	Bulk modulus
$\boldsymbol{b}$	Wing span
C_L	Lift coefficient
C_{L_0}	Zero lift coefficient
$C_{L\alpha}$	Lift due to angle of attack variation coefficient
$C_{L\delta_e}$	Lift due to elevator deflection variation coefficient
C_{Lih}	Lift due to trim angle variation coefficient
C_l	Rolling moment coefficient
$C_{l\delta_a}$	Aileron contribution to rolling moment coefficient
$C_{l\phi}$	Bank angle contribution to rolling moment coefficient
C_M	Pitching moment coefficient
C_{M_0}	Zero pitching moment coefficient
$C_{M\alpha}$	Pitching moment due to angle of attack variation coefficient
$C_{M\delta_e}$	Pitching moment due to elevator deflection variation coefficient
C_{Mih}	Pitching moment due to trim angle variation coefficient
$\boldsymbol{c}$	Viscous damping coefficient
ΔC_L	Lift coefficient offset due to asymmetries
ΔC_M	Pitching moment coefficient offset due to asymmetries
δ_a	Shock absorber deflection, Eq. (2.1)

δ_e	Elevator deflection angle
δ_r	Tyre deflection
$\boldsymbol{D}$	Drag force
ε	Angle of thrust
$\vec{F}$	Damping force
F_0	External forces
F_a	Shock absorber forces
$F_{a/t}$	Aircraft to landing gear interaction forces
$[F_c\ ]$	Nonlinear terms
F_g	Gas force
F_r, F_R	Tyre forces
$F_{t/a}$	Landing gear to aircraft interaction forces
Fz_{CG}	Total vertical force at centre of gravity
γ	Polytropic gas constant
[GM]	Aircraft generalised mass matrix
[GS]	Aircraft generalised stiffness matrix
ih	Elevator trim angle
$\boldsymbol{K}$, K_{r1}	Tyre pressure dependent constant
K_{r2}	Rubber plasticity dependent constant
λ	Wavelength
$\boldsymbol{L}$	Lift force
μ	Braking coefficient
μ_{MLG}	Main landing gear friction coefficient
μ_{NLG}	Nose landing gear friction coefficient
MAC	Mean Aerodynamic Chord
Mx_{CG}	Total rolling moment at centre of gravity
My_{CG}	Total pitching moment at centre of gravity
$\boldsymbol{N}$	Tyre pressure dependent constant
N_{MLG}	Normal force at main landing gear

N_{NLG}	Normal force at nose landing gear
P_0	Initial gas pressure
$\boldsymbol{q}$	Landing gear geometric coordinates
ρ	(Air) Density
S	Wing surface
S	Piston area. Eq. (2.1)
$\boldsymbol{T}$	Total thrust force
$\boldsymbol{[TM]}$	Landing gear generalised mass matrix
t_R	Reference instant of time
V	Velocity TAS
V_0	Initial gas volume
$[V_a\ ]$	Shock absorber forces geometric transformation matrix
V_l	Initial oil (liquid) volume
V_R	Reference velocity
$[V_r\ ]$	Tyre forces geometric transformation matrix
$\boldsymbol{W}$	Aircraft weight
$\boldsymbol{x}$	Modal generalised coordinates
x_{aero}	Horizontal position to lift application point
x_{CG}	Horizontal position to centre of gravity
x_{eng}	Horizontal position to engine location
X_i'	X runway position after adaptation
X_R	Reference X runway position
y_{aero}	Lateral position to lift application point
y_{CG}	Lateral position to centre of gravity
y_{eng}	Lateral position to engine location
z_{CG}	Vertical position to centre of gravity
z_{eng}	Vertical position to engine location
$[\emptyset\ ]$	Modal matrix

Appendix B

List of abbreviations

A/C	Aircraft
AMC	Acceptable Means of Compliance
CBR	California Bearing Ratio
CRI	Certification Review Item
CS	Certification Specifications
DEF-STAN	Defence Standards
DSP	Digital Signal Processing
EASA	European Aviation Safety Agency
EBH	Equivalent Bump Height
FCS	Flight Control System
FEM	Finite Element Method
FTI	Flight Test Instrumentation
GVT	Ground Vibration Test
HTP	Horizontal Tail Plane
IM	Interpretative Material
ISA	International Standard Atmosphere
L/G	Landing Gear
MAC	Mean Aerodynamic Chord
MCRI	Military Certification Review Item
MFW	Maximum Fuel Weight

MLG	Main Landing Gear
MLW	Maximum Landing Weight
MPL	Maximum Payload
MTOW	Maximum Take-Off Weight
NLG	Nose Landing Gear
OCCAR	Organisation Conjointe de Coopération en matière d'Armement
PSD	Power Spectral Density
SC	Special Condition
VTP	Vertical Tail Plane

Appendix C

EASA CS 25.491/AMC 25.491

CS 25.491: Taxi, take-off and landing roll

Within the range of appropriate ground speeds and approved weights, the aeroplane structure and landing gear are assumed to be subjected to loads not less than those obtained when the aircraft is operating over the roughest ground that may reasonably be expected in normal operation. (See AMC 25.491.)

AMC 25.491: Taxi, take-off and landing roll

C.1 Purpose

This AMC sets forth acceptable methods of compliance with the provisions of CS-25 dealing with the certification requirements for taxi, take-off and landing roll design loads. Guidance information is provided for showing compliance with CS 25.491, relating to structural design for aeroplane operation on paved runways and taxi-ways normally used in commercial operations. Other methods of compliance with the requirements may be acceptable.

C.2 Related Certification Specifications

The contents of this AMC are considered by the Agency in determining compliance with CS 25.491. Related paragraphs are CS 25.305(c) and CS 25.235.

C.3 Background

a) All paved runways and taxi-ways have an inherent degree of surface unevenness, or roughness. This is the result of the normal tolerances of engineering standards required for construction, as well as the result of events such as uneven settlement and frost heave. In addition, repair of surfaces on an active runway or taxi-way can result in temporary ramped surfaces. Many countries have developed criteria for runway surface roughness. The International Civil Aviation Organization (ICAO) standards are published in ICAO Annex 14.

b) In the late 1940's, as aeroplanes became larger, more flexible, and operated at higher ground speeds, consideration of dynamic loads during taxi, landing rollout, and take-off became important in aeroplane design. CS 25.235, CS 25.491 and CS 25.305(c) apply.

c) Several approaches had been taken by different manufacturers in complying with the noted regulations. If dynamic effects due to rigid body modes or airframe flexibility during taxi were not considered critical, some manufacturers used a simplified static analysis where a static inertia force was applied to the aeroplane using a load factor of 2.0 for single axle gears or 1.7 for multiple axle gears. The lower 1.7 factor was justified based on an assumption that there was a load alleviating effect resulting from rotation of the beam, on which the forward and aft axles are attached, about the central pivot point on the strut. The static load factor approach was believed to encompass any dynamic effects and it had the benefit of a relatively simple analysis.

d) As computers became more powerful and dynamic analysis methods became more sophisticated, it was found that dynamic effects sometimes resulted in loads greater than those which were predicted by the static criterion. Some manufacturers performed calculations using a series of harmonic bumps to represent a runway surface, tuning the bumps to excite various portions of the structure at a given speed. U.S. Military Standard 8862 defines amplitude and wavelengths of 1-cosine bumps intended to excite low speed plunge, pitch and wing first bending modes.

e) Some manufacturers used actual runway profile data to calculate loads. The runway profiles of the San Francisco Runway 28R or Anchorage Runway 24, which were known to cause high loads on aeroplanes and were the subject of pilot complaints until resurfaced, have been used in a series of bi-directional constant speed analytical runs to determine loads. In some cases, accelerated runs have been used, starting from several points along the runway. The profiles of those runways are described in NASA Reports CR-119

and TN D-5703. Such deterministic dynamic analyses have in general proved to be satisfactory.

f) Some manufacturers have used a statistical power spectral density (PSD) approach, especially to calculate fatigue loads. Extensive PSD runway roughness data exist for numerous world runways. The PSD approach is not considered practical for calculation of limit loads.

g) Because the various methods described above produce different results, the guidance information given in paragraphs 4, 5, and 6 of this AMC should be used when demonstrating compliance with CS 25.491.

C.4 Runway Profile Condition

a) Consideration of airframe flexibility and landing gear dynamic characteristics is necessary in most cases. A deterministic dynamic analysis, based on the San Francisco Runway 28R (before it was resurfaced), described in Table 1 of this AMC, is an acceptable method for compliance. As an alternative means of compliance, the San Francisco Runway 28R (before it was resurfaced) may be used with the severe bump from 1530 to 1538 feet modified per Table 2. The modifications to the bump reflect the maximum slope change permitted in ICAO Annex 14 for temporary ramps used to transition asphalt overlays to existing pavement. The points affected by this modification are outlined in Table 1.

b) Aeroplane design loads should be developed for the most critical conditions arising from taxi, take-off, and landing run. The aeroplane analysis model should include significant aeroplane rigid body and flexible modes, and the appropriate landing gear and tyre characteristics. Unless the aeroplane has design features that would result in significant asymmetric loads, only the symmetric cases need be investigated.

c) Aeroplane steady aerodynamic effects should normally be included. However, they may be ignored if their deletion is shown to produce conservative loads. Unsteady aerodynamic effects on dynamic response may be neglected.

d) Conditions should be run at the maximum take-off weight and the maximum landing weight with critical combinations of wing fuel, payload, and extremes of centre of gravity (c.g.) range. For aeroplanes with trimable stabilisers, the stabiliser should be set at the appropriate setting for take-off cases and at the recommended final approach setting for landing cases. The elevator should be assumed faired relative to the stabiliser throughout

the take-off or landing run, unless other normal procedures are specified in the flight manual.

e) **A series of constant speed runs should be made in both directions from 37 km/h (20 knots) up to the maximum ground speeds expected in normal operation (V_R defined at maximum altitude and temperature for take-off conditions, 1.25 V_{L2} for landing conditions). Sufficiently small speed increments should be evaluated to assure that maximum loads are achieved. Constant speed runs should be made because using accelerated runs may not define the speed/roughness points which could produce peak dynamic loads. For maximum take-off weight cases, the analysis should account for normal take-off flap and control settings and consider both zero and maximum thrust. For maximum landing weight cases, the analysis should account for normal flap and spoiler positions following landing, and steady pitching moments equivalent to those produced by braking with a coefficient of friction of 0.3 with and without reverse thrust. The effects of automatic braking systems that reduce braking in the presence of reverse thrust may be taken into account.**

C.5 Discrete load condition

One of the following discrete limit load conditions should be evaluated:

a) With all landing gears in contact with the ground, the condition of a vertical load equal to 1.7 times the static ground reaction should be investigated under the most adverse aeroplane loading distribution at maximum take-off weight, with and without thrust from the engines.

b) As an alternative to paragraph 5.a. above, it would be acceptable to undertake dynamic analyses under the same conditions considered in paragraph 4 of this AMC considering the aircraft response to each of the following pairs of identical and contiguous 1-cosine upwards bumps on an otherwise smooth runway:

   i) Bump wavelengths equal to the mean longitudinal distance between nose and main landing gears, or between the main and tail landing gears, as appropriate; and separately:

   ii) Bump wavelengths equal to twice this distance.

   The bump height in each case should be defined as:

$$H = A + B\sqrt{L}$$

Where:

H = the bump height

L = the bump wavelength

A = 1.2, B = 0.023 if H and L are expressed in inches

A = 30.5, B = 0.116 if H and L are expressed in millimetres

C.6 Combined load condition

A condition of combined vertical, side and drag loads should be investigated for the main landing gear. In the absence of a more rational analysis a vertical load equal to 90% of the ground reaction from paragraph 5 above should be combined with a drag load of 20% of the vertical load and a side load of 20% of the vertical load. Side loads acting either direction should be considered.

C.7 Tyre conditions

The calculation of maximum gear loads in accordance with paragraphs 4, 5, and 6, may be performed using fully inflated tyres. For multiple wheel units, the maximum gear loads should be distributed between the wheels in accordance with the criteria of CS 25.511.

[Amdt No: 25/2]

[Amdt No: 25/8]

Appendix D

Socioeconomic background

The present Bachelor Thesis is focused on the analysis of the experimental data gathered at Ablitas and Écury sur Coole taxi campaigns, and the posterior performance of numerical simulations to match the respective aircraft numerical and experimental responses.

A detailed estimation of costs is solely presented for the analysis of experimental raw data and the subsequent performance of numerical simulations. The cost of the underlying trials at Ablitas and Écury sur Coole runways is not included since these took place in 2013 and 2015, respectively. Moreover, they were not exclusively aimed for studying the aircraft capability in taxi. Aircraft performance, actuation or fatigue are further analyses which were covered during both campaigns, as well.

The work developed to the completion of this project has been carried out from February to June 2016. The tasks which were required to be performed during this time period include:

1. Getting familiar with Airbus informatics and in-house software used to compute dynamic loads numerically.
2. Familiarisation with taxi loads problem: relevance in aircraft design, history of taxi loads trials, accidents, applicable airworthiness regulations, noteworthy parameters which enhance the analysis of taxi loads, description of the specimen.
3. Data gathering of Ablitas and Écury sur Coole test results: suitable time-windows, relevant magnitudes to compare, description of FTI instrumentation, post-processing tools.
4. Runway path and runway profile conception.

5. Performance of numerical simulations: comparison between test and numerical simulation results, calibration and tuning of numerical results to match experimental responses.

6. Wrap up of work performed, digestion of results: impact of braking coefficients on taxi loads, proposal of future activities, conclusions.

7. Project documentation.

The different duties above are executed within a specific time span. These are shown in Figure D.1.

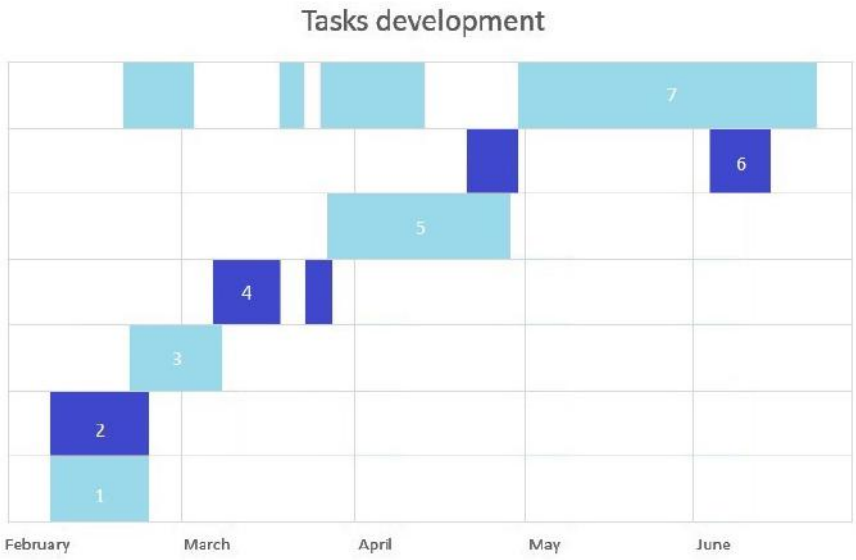

Figure D.1 Gantt chart

Furthermore, the total number of working days amounts to 120 days. An estimation of 8 working hours per day is established. The total amount of working hours is 960 hours. It should be pointed out that an average value of 300 working hours out of 960 are shared with the mentor.

The calculation of costs is divided into direct and indirect costs. The first one includes personnel wages, software licenses and equipment costs. Electricity and Internet connection fares are examples of indirect costs. Due to the difficulty to quantify electricity charges, indirect costs are established to be 5% of direct costs.

The salary a recent undergraduate Aerospace Engineer (Bachelor's Degree) gets hourly is estimated to be 13.16€/h hour[1]. A ten year-experience Aerospace Engineer earns 36.62€/h. The total personnel expenses amount to 22,425.48€.

Labour cost			
Engineer	**Working time** [h]	**Cost** [€/h]	**Total** [€]
Undergraduate	960	13.16	12,638.04
Experienced	300	36.62	9,787.44
			22,425.48

Table D.1 Labour costs

The equipment and software licenses costs are itemised in the following table. Amortization costs are included. For that, a straight linear depreciation model applies. The amortization coefficient percentages are gathered from 2015 amortization rates.

Equipment and software cost			
Item	**Price** [€]	**Amortization** [%]	**Total** [€]
PC/laptop	1,000	25	250
Office 2013	105.6	33	34.85
MATLAB Academic use	500	33	165
Fortran compiler for UNIX	1,300	33	429
MSC.NASTRAN	25,000	33	8,250
Taxi loads software	20,000	33	6,600
			15,728.85

Table D.2 Equipment and software costs

Indirect costs (5% direct costs) amount to 1,907.72 €. The total project cost is estimated to be 40,062.05€.

Total project cost	
Item	**Total** [€]
Direct costs	38,154.33
Indirect costs	1,907.72
	40,062.05

Table D.3 Total project cost

[1] `http://www.sipa.es/files/calendarios/SIPA_Cubo_2016_Getafe.pdf`